UNIVERSITY OF SOUTHAMPTON

FACULTY OF SOCIAL & HUMAN SCIENCES

School of Geography and Environment

The Application of Terrestrial Laser Scanning to Measure Small Scale Changes in Aeolian Bedforms

by

Robert Squirrell

Thesis for the degree of Master of Philosophy

March 2011

UNIVERSITY OF SOUTHAMPTON

ABSTRACT

FACULTY OF SOCIAL & HUMAN SCIENCES
SCHOOL OF GEOGRAPHY AND ENVIRONMENT

Master of Philosophy

THE APPLICATION OF TERRESTRIAL LASER SCANNING TO MEASURE SMALL SCALE CHANGES IN AEOLIAN BEDFORMS

by Robert Squirrell

Traditional methods used to measure aeolian sediment transport rely on point based sampling, such as sand traps or saltation impact sensors, which ignore the spatial heterogeneity displayed in the transport system. Obtaining an accurate transport rate is important to parameterise predictive models, which currently show large deviations between measured and predicted rates.

Terrestrial laser scanning (TLS) is a tool that is rapidly emerging in the field of geomorphology. It provides the ability to capture surface elevation data of in-situ bedforms at the spatial and temporal scale necessary to link change, such as ripple migration, to the processes that drive them. Repeat scans provide digital elevation models which can be differenced to provide volumetric rates of change, in a process known as the morphologic method. However, utilising data at such high resolutions requires an accurate estimation of error in order to provide meaningful results.

Typically the morphologic method documents surface change between geomorphic events. However, due to the high temporal variability displayed by the aeolian transport system, measuring topographic change during a transport event would be beneficial. Using TLS during active transport removes the ability to take multiple convergent scans. Therefore current methods of approximating error in TLS derived surfaces by using convergent scans from multiple scan locations cannot be applied.

The influence of scanning geometry and survey set up is explored in order to quantify and reduce errors when scanning small scale bedforms from a single location. This is then applied to an active transport event to measure wind ripple migration, and derive a sediment transport rate using the morphologic method. The results suggest TLS is a viable tool for capturing in-situ aeolian ripples. Scan incidence angle is shown to significantly affect point density and therefore point cloud accuracy. The influence of incidence angle is different depending on the extent of the bedform studied. Ripples were measured during an active transport event in the Great Sand Dunes National Park, Colorado. Ripple morphologies and migration rates were within previously observed ranges. Applying the morphologic method highlighted ripple migration patterns, surface change and enabled an overall sediment budget to be calculated.

Contents

List of Figures

List of Tables

List of Symbols

ϕ	Transport intensity function
κ	Von Karman constant
σ	Standard deviation of DEM error
ρ_a	Air density
ρ_s	Sediment density
A	Shields function
b	Bedform growth
d	Mean grain diameter
D	Aerodynamic drag
e	Saltation feedback through grain ejection
g	Gravity
I_p	Interparticle force
L	Lift
M	Moment
$_{min}LoD$	Threshold level of detection
r	Reptation
s	Saltation
t	Time
τ	Shear stress
u	Wind speed
u_*	Shear velocity
u_{*t}	Threshold shear velocity
W	Weight
z	Elevation
z_o	Aerodynamic roughness length
z_{of}	Bed morphology effecting shear stress through drag,
z_{os}	Saltating grains extracting momentum from the wind

DECLARATION OF AUTHORSHIP

I, Robert Squirrell declare that the thesis entitled *The Application of Terrestrial Laser Scanning to Measure Small Scale Changes in Aeolian Bedforms* and the work presented in the thesis are both my own, and have been generated by me as the result of my own original research. I confirm that:

- this work was done wholly or mainly while in candidature for a research degree at this University;
- where any part of this thesis has previously been submitted for a degree or any other qualification at this University or any other institution, this has been clearly stated;
- where I have consulted the published work of others, this is always clearly attributed;
- where I have quoted from the work of others, the source is always given. With the exception of such quotations, this thesis is entirely my own work;
- I have acknowledged all main sources of help;
- where the thesis is based on work done by myself jointly with others, I have made clear exactly what was done by others and what I have contributed myself;
- none of this work has been published before submission, **or** [delete as appropriate] parts of this work have been published as: [please list references]

Signed:

Date:

Acknowledgements

I would like to thank my supervisors, Joanna Nield, Jadu Dash and Stephen Darby for their invaluable assistance, feedback, ideas and support. I am grateful to Jo in particular for providing data and showing great patience while this thesis was completed. Many thanks to Julian Leyland, who was a sounding board for ideas, and provided great help with the laser scanner. I am grateful to the support staff at Southampton, especially Julie Drewitt, for their help.

I would like to thank Andrew Lawrence at the National Trust for the use of the East Head beach for data collection.

Andrew Valdez provided assistance at the Great Sand Dunes National Park before and during the visit. Nick Lancaster, Charlie Bristow and Jo Nield also assisted in the data collection in the Great Sand Dunes Park.

Chris Hackney, Trevor Bond, Gary Watmough, Simon Dixon and Simon Hunter were great company in the office, and offered assistance whenever it was needed.

Chapter 1: Introduction

The spatial variability of aeolian sand transport is important to understand in order to provide more accurate sediment transport equations (Jackson *et al*., 2006). Predictive equations are important in order to relate in situ wind characteristics to sediment transport rates in environments affected by aeolian transport such as dune fields and sand beaches (Nickling and McKenna, Neuman, 1997). Predictive models attempt to relate wind shear velocity, to sediment transport rate, however when compared to empirical field observations, their performance is poor (Haff, 1996; Arens, 1996; Sherman *et al*., 1998; Liu *et al*., 2006). These equations assume ideal transport conditions which are rarely met in natural environments (Shao and Lu, 2000), due to a number of spatial and temporal factors. Spatial factors include wind speed fluctuations, turbulence, topography, streamers, moisture and roughness elements.

The above factors are compounded by difficulties in measuring sediment transport (Jones and Willets, 1979; Nickling and McKenna Neuman, 1997; Ellis *et al.*, 2009a). Methods used to quantify transport generally fall into two categories: sediment traps, that seek to capture moving sediment, and at-a-point devices which detect saltation impacts and relate impact frequency to sediment transport (Barchyn and Hugenholtz, 2010). The ability of point based methods to accurately quantify sediment flux are limited by the spatial variability displayed during aeolian transport. Typically, few samplers are deployed in the field, and are assumed to be representative of the study area, however sand transport is not a uniform blanket of saltating grains but displays large spatial heterogeneity (Baas and Sherman, 2006; Baas, 2008). Jackson *et al*., (2006) deployed five sand traps in an array and recorded disparities between flux measurements of 150%. Similarly, Baas and Sherman, (2006) document differences of 266% in an array of 35 saltation impact sensors.

Given the limitations of traditional techniques, it is worth considering the merits of an alternative approach to estimating total mass flux, namely the morphologic method. In this technique, mass flux is estimated using the principle of conservation of mass (Brasington *et al*., 2000). In this approach, repeat topographic surveys are undertaken, which can be used to produce digital elevation models (DEMs). Provided the spatial extents match, the later DEM can be subtracted from the former to provide a total volumetric change (Brasington and Smart, 2003). This approach has typically been employed in fluvial geomorphological studies, over large spatial and temporal scales (Fuller *et al*., 2003; Martin, 2003) as a result of survey equipment which limited the spatial and temporal resolution that was achievable (Wheaton *et al*., 2010). However advances in surveying techniques have cut acquisition times by an order of magnitude (Marcus and Fonstad, 2008) and improvements in surveying equipment have improved the spatial resolution achievable in the field.

Terrestrial laser scanning (TLS) has recently emerged as a feasible monitoring tool (Brasington *et al.*, 2007; Heritage and Hetherington, 2007; Milan *et al.*, 2007; Heritage and Large, 2009; Hodge *et al.*, 2009a, 2009b), able to capture topographic data at spatial and temporal resolutions small enough to link process and form in aeolian environments (Baas, 2008). TLS (or ground based LiDAR) utilises electro-optical distance measurement to obtain a point cloud of a required surface at resolutions in the order of 10^3 points m^{-3} and rates of up to 50,000 points/second. The distance of each point from the scanning position is calculated using either phase difference or a time-of-flight laser pulse (Hodge, 2010).

TLS offers the opportunity to capture small scale aeolian bedforms such as ripples and proto dunes, at temporal resolutions low enough to link wind speed with surface change. However, TLS data is subject to numerous sources of error, and point cloud precision can be affected by scanning geometry and object properties. TLS has been applied to relatively few aeolian studies (Nagihara, *et al*., 2004; Ochoa, 2005; Nield *et al*., 2011; Nield and Wiggs, 2011) and this gives the opportunity to develop standardised protocols and error assessments when using TLS in aeolian environments. Therefore, the aims of this thesis are to develop a set of protocols in order to reduce erroneous results when applying TLS to aeolian environments. The effect of scanning geometry specific to scanning small scale aeolian bedforms will be explored. The dynamic and intermittent conditions experienced in aeolian environments require novel use of the TLS and these will be developed. The TLS will then be applied to capture migrating ripples and develop a sediment budget for an aeolian transport event.

Chapter 2: Literature Review

Aeolian deposits constitute a significant proportion of the Earth’s surface. The United Nations Environment Programme (UNEP) estimate that just less than 50% of the Earth’s total land cover can be classified as dryland, and of this 20% are sand seas directly influenced by aeolian transport (UNEP, 1997, Figure 2.1). Dune encroachment onto agricultural land in arid and semi-arid areas poses a threat to local food security (Geist and Lambin, 2004). Dune migration onto transport structures and other infrastructure forms is a wide spread problem that requires significant economic costs to mitigate (Khalaf and Al-Ajmi, 1993; Liu *et al*., 2006; Yao *et al.,* 2007).

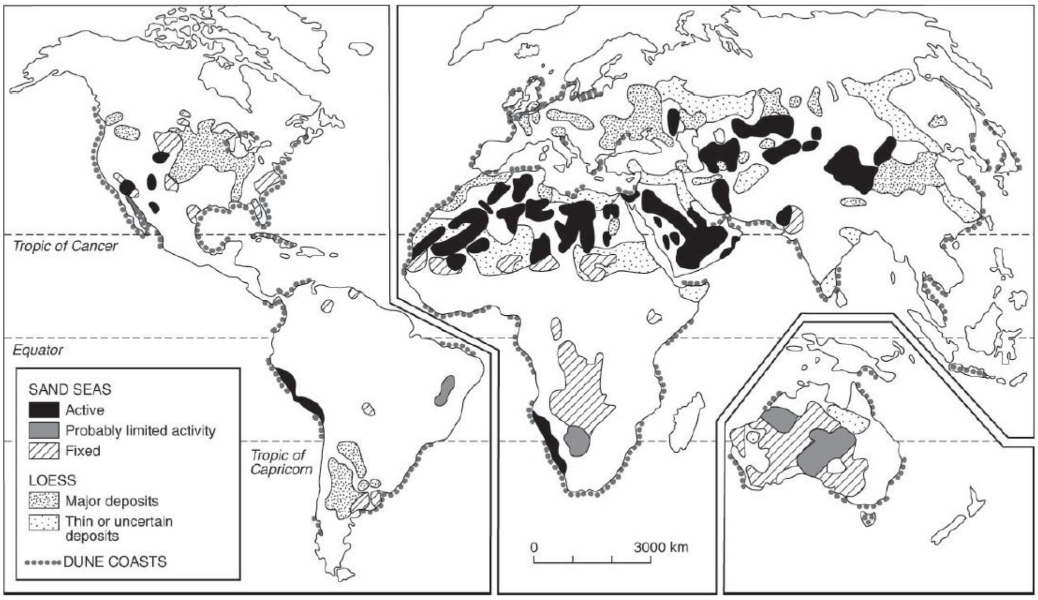

Figure 2.1: Map showing areas of Sand seas, Loess deposits and Coastal dunes. Reproduced from Thomas and Wiggs (2008).

Coastal regions can also be influenced by aeolian transport processes. Coastal dunes act as a sand reservoir which can delay coastline retreat and protect low lying backshore areas (Ruz and Meur-Ferec, 2004). Dune systems on barrier islands provide an effective defence against hurricanes (Houser, 2009). This is particularly relevant as sea levels are widely predicted to increase over the next century, and predicting dune response to such rises will be crucial (Szkornik *et al., 2008)***.**

2.1 Sediment Entrainment

When a surface of sand grains is subjected to shear stress imparted from a moving body of air, there is potential for sand transport. An individual grain will be entrained in transport when the fluid forces of lift and drag overcome the inhibiting forces of gravity, granular friction and inter-particle cohesion (Figure 2.2) (Jackson, 1996a). Lift is created as a result of decreased fluid pressure at the top of a grain, whilst the inhibiting forces are related to the physical properties of the grain such as its weight, density, packing, size and mineralogy.

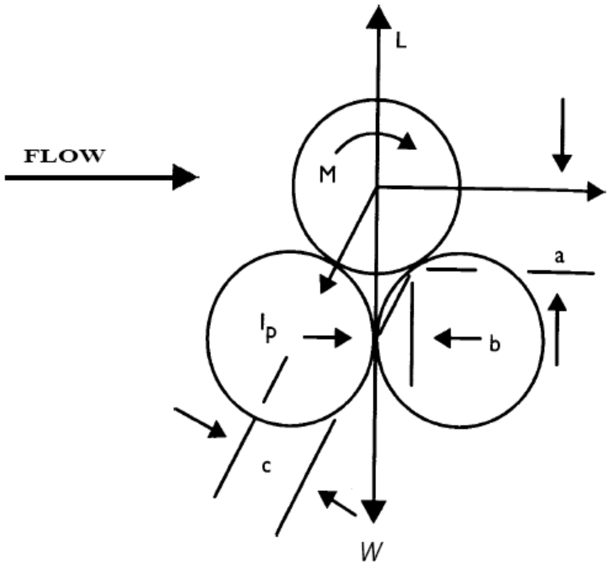

Figure 2.2 Schematic showing packed grains on a bed and the forces acting upon them: L = lift, M = moment, D = aerodynamic drag, I_p= interparticle force and W = weight. Moments about a point are given

As shear velocity increases, a point is reached where grain motion is initiated known as the threshold shear velocity, u_{*t} typically estimated using Bagnold (1941) equation:

$$u_{*_t} = A\sqrt{\frac{gd(\rho_s - \rho_a)}{\rho_a}} \qquad (2.3)$$

Where A is the square root of Shields function (a dimensionless variable encompassing the factors that interact to initiate sediment motion) = $(\theta)^{1/2}$ = 0.1; ρ_s is sediment density; ρ_a is the air density – 1.23kg m^{-3}; g is gravity = 9.8 m s^{-2} and d is mean grain diameter. Theoretically u_{*t} could be estimated using only particle diameter, however this is only under ideal conditions which are rarely met in a natural setting (Shao and Lu, 2000). Numerous other environmental variables will influence the entrainment process. Natural sediments consist of a range of grain sizes and shapes which vary in the density and way they are packed together which suggests a threshold range may be more appropriate than a single value (Lancaster, 1995). Local topography also has an influence, threshold shear velocity is significantly lower on downward sloping surfaces as Hardisty and Whitehouse (1988) demonstrate. Surface moisture also increases the shear velocity required for transport as capillary forces increase the apparent particle cohesion (McKenna-Neuman and Nickling, 1989). Increasing gravimetric moisture content from 0-8% requires increasingly strong winds to dislodge surface particles, and experiments have shown the transport system shuts down when the surface is around 10% saturated (Davidson-Arnott *et al.,* 2008). This process may not be prevalent in hyper-arid environments, defined as areas where the ratio of precipitation (p) to potential evapotranspiration (pet) is less than 0.05. However, surface moisture plays an increasingly important role in arid (p/pet 0.05-0.2) and semi-arid environments (p/pet 0.2-0.5) due to the increasing precipitation, (Thomas, 2005). There are also numerous sources of moisture in coastal environments such as wave uprush, presence of a water table and precipitation (Davidson-Arnott *et al.,* 2008). Surface sediments may also be bound together by soluble salts or organic matter to form surface crusts that are resistant to the influence of the wind. The presence of a surface crust will significantly reduce the amount of sediment eroded by the wind compared to unconsolidated surfaces (Goosens, 2004). The influence of non-erodible surface elements such as vegetation and debris can also influence entrainment rate as they provide a level of protection to the underlying sediment. Low density surface roughness elements generally lower threshold velocity due to eddie development, whilst larger roughness densities have the opposite effect (Lancaster, 1995).

Shermann and Hotta (1990) suggest that if all parameters influencing threshold velocity can be characterised, then accurate prediction would be possible. However, the idea that both thresholds can be treated as constant has been called into question. Nickling (1988) showed a gradual transition in motion from rolling to a sudden saltation cascade. The rate of mass transport has also been shown to respond irregularly to intermittent wind forcing events (Spies *et al.*, 2000). McMenamin (2002) produced similar results in a wind tunnel study where a single grain size and continuous wind velocity were maintained. In spite of the homogenous conditions, a chaotic transport response was still observed which led the authors to conclude that the surface bed displays self-organising behaviour whereby grain impacts rework the surface to the point where a single impact can trigger an entire transport event. Thus, without detailed knowledge of the structure of the sand bed it is difficult to predict the timing or magnitude of events. However, detailed representation of the bed is difficult to obtain in the field without causing disturbance to the wind flow and thus the transport system itself.

Once the threshold for motion is crossed, transport as a direct response to the wind, occurs in three forms, creep, saltation and suspension (Figure 2.3). Creep is the rolling or gliding of a grain in contact with the bed, saltation is the movement of grains by small hops and is the predominant form of aeolian transport (Bagnold, 1941). Suspension is where a grain is entrained and sustained in transport for large distances and contributes a relatively small proportion of mass flux due to the size of the particles susceptible to suspension (Wang *et al.*, 2009). Saltation is the predominant sediment transport process, and as such has received most attention within the literature (Namikas, 2003). A saltating particle, once entrained, follows a steep ascent of around 50° before descending and impacting the bed at angles of 9-15°. Saltation trajectories are governed by gravity, aerodynamic drag, the magnus effect (lift generated by rapid spinning) and aerodynamic lift (Manukyan and Prigozhin, 2009). Bagnold (1941) argued that initial take off speed was in the same order as the shear velocity. However, both Namikas (2003) and Rasmussen and Sorensen (2008) have undertaken numerical modelling which suggests this is not the case, and take off speed is largely independent of shear velocity. Bagnold (1941) used this assumption to produce his widely used sand transport equation (Section 2.7)

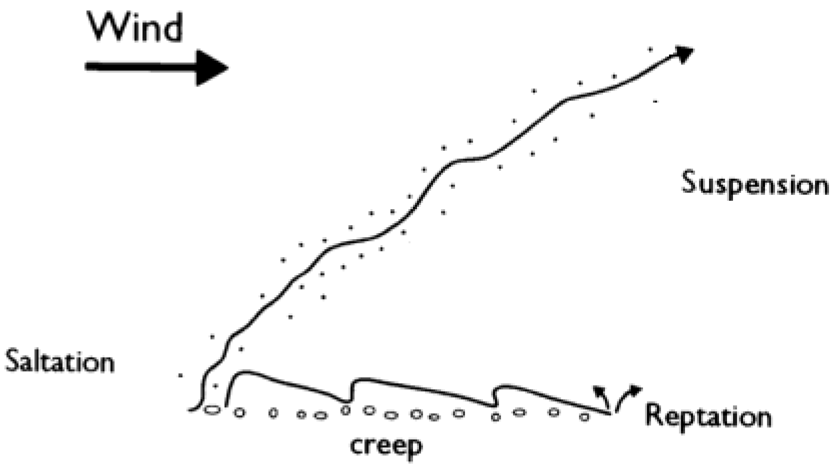

Figure 2.3. Schematic showing the main processes of aeolian mass transport (after Pye, 1987).

When a saltating grain impacts the bed, energy is either dissipated as heat, or transferred to other grains (Baas, 2007). The grain usually rebounds to a height where it can be entrained by the wind again and continues saltating. The energy imparted at the bed can cause low energy ejection of grains in a process known as reptation (Ungar and Haff, 1987) and is typically modelled as the splash function (Werner and Haff, 1988). Saltation impacts can also provide enough energy to other grains to be entrained in saltation at lower shear velocities than if that grain was influenced by fluid forces alone. This is known as the impact or dynamic threshold (Eq.2.3) but with the Sheilds function taking a value of 0.08 (McKenna-Neuman, 1993). The relative proportions of each mode of transport contributing to total mass flux have been the subject of some debate. Bagnold (1941) estimated the proportion of bedload transport (creep and reputation) to be around 25%, whilst Namikas (2003) reported values of 10% of total transport. However Namikas (2003) suggests that this value may be an underestimation due to systematic bias as a result of sand trapping, which can exclude the creep and reptation component due to scour (See Section 2.8).

A fully saturated saltating layer has a dynamic feedback effect on the near-surface wind velocity profile. Saltating grains extract momentum from the flow which in turn reduces the shear velocity (Baas, 2007). Owen (1964) argued the shear velocity influencing the bed is reduced to equal the impact threshold in a process typically termed the ‘Owen effect’ (Gillette, 1999). The alteration of the velocity profile by saltating grains therefore means the law-of-the-wall no longer applies to the saltating layer and wind profiles are non-logarithmic. It is thought however, that the thickness of the saltating layer is proportional to the aerodynamic roughness imparted by the saltating grains themselves and will therefore correlate to u_*^2. These processes have been supported through numerical modelling using self regulating cloud-models (McEwan and Willets, 1993). These models assume a uniform cloud of saltating grains across a surface, which is challenged by observations of quasi-linear saltation transport across natural surfaces (Baas, 2008). These features, known as streamers, snake in a streamwise direction merging and splitting as they travel downwind and highlight the spatial variability of sand transport (Baas and Sherman, 2005; Baas and Sherman, 2006). A number of hypotheses for streamer formation have been postulated (Baas, 2008), and results indicate that their formation is a result of near surface gusting, related to larger scale eddies descending through the boundary layer. Microtopography is also cited as a possible mechanism for streamer formation and may be especially important when shear velocity is approaching the fluid threshold (Baas 2008). Research undertaken by Baas (2003) using a coupled boundary layer air flow and aeolian transport model (SAFE, Van Dijk *et al.*, 1999) indicated that bed elevations of only 5cm experienced a 10-25% increase in sand transport rate over surrounding lower areas. This is somewhat unsurprising as flow velocity increases with distance above the bed (Stull, 1988) and airflow compression occurs over topographic obstacles resulting in an increase in wind speed on the windward slope of the obstacle (Walker *et al.*, 2006). Baas and Sherman's (2005) study indicated that streamers formed even when the surface was artificially flattened to the point where microtopographic variation was minimal. This suggested that such variation is not necessary for streamers to form, however, this was put forward tentatively as the experiment did not measure the effect of microtopography on saltation dynamics. Microtopography in the form of aeolian ripples are potentially an important factor in the sand transport system (McEwan and Willets, 1993), and ripple formation has been shown to cause a decrease in sand transport rate (Butterfield, 1991; Rasmussen and Mikkelsen, 1991). Streamer behaviour is likely to induce further variation in bed topography (Baas and Sherman, 2005) and therefore ripple development. Saltation impact intensity has been shown to drive ripple development (Sharp, 1963) therefore it is conceivable that variation in saltation intensity could drive defect creation from a rippled bed due to crestline breakup (Kocurek *et al.*, 2010). Due to high spatial and temporal variability in aeolian sediment transport, accurately measuring transport rates has proved difficult.

2.2 Aeolian Bedforms

Aeolian environments are dominated by hierarchical bedforms, ranging in size from ripples (wavelengths 0.1-1m), individual dunes (wavelengths 50-500m) and compound and complex dunes (wavelengths >500m) (Lancaster, 1995). Bedform formation is a positive feedback mechanism, a result of small scale perturbations in the sand surface which influence the airflow and modify patterns in erosion and deposition which encourage bedform growth (Pelletier, 2009). This feedback loop between bedforms and airflow, especially with respect to ripple formation, is not well understood (Baas, 2007). Wind ripples are present on over 80% of sand surfaces in all dune areas (Lancaster, 1995) and are important to consider when investigating small scale aeolian processes.

2.3 Wind Ripples

Wind ripples form as a result of bed deformation during sand transport and are found in all depositional aeolian environments. Ripples are regular undulations orientated perpendicular to the wind direction and are typically asymmetric in profile. The stoss slope is convex with a usual incline of around 8° - 10° whilst the lee slope consists of a short steep (30°) slope near the crest, followed by a shallower concave slope. The lee slope does not typically reach the angle of repose for sand of around 30-35° (Sharp, 1963). Characteristic wind ripples are 5-10mm in height, have a wavelength of 50-200mm and a median grain size of 0.3-0.35mm (Bagnold, 1941; Sharp, 1963). Much larger ripples have been observed in the field, with wavelengths ranging from 0.5-2m and an amplitude of 0.1m. These are often composed of much larger grains of around 1-4mm median grain size and have been variously termed granule ripples (Sharp, 1963; Fryberger *et al.,* 1992), or mega ripples (Greeley and Iverson, 1985). These features are treated as separate entities by Sharp (1963), however Ellwood *et al.,* (1975) argued they are not separate forms, but are rather two extremes of a continuum of ripple dimensions. The conditions required to produce mega ripples are rarely met, as there are usually smaller grains more susceptible to transport. This observation is extended by Lancaster (1995), (Figure 2.4), who suggests variation in ripple dimensions reflect differences in wind speed, particle sorting and sediment size. Due to their size, ripples respond to changes in wind direction and local sediment transport conditions in an order of minutes and therefore provide good in situ indicators of changes to the transport system (Lancaster, 1995).

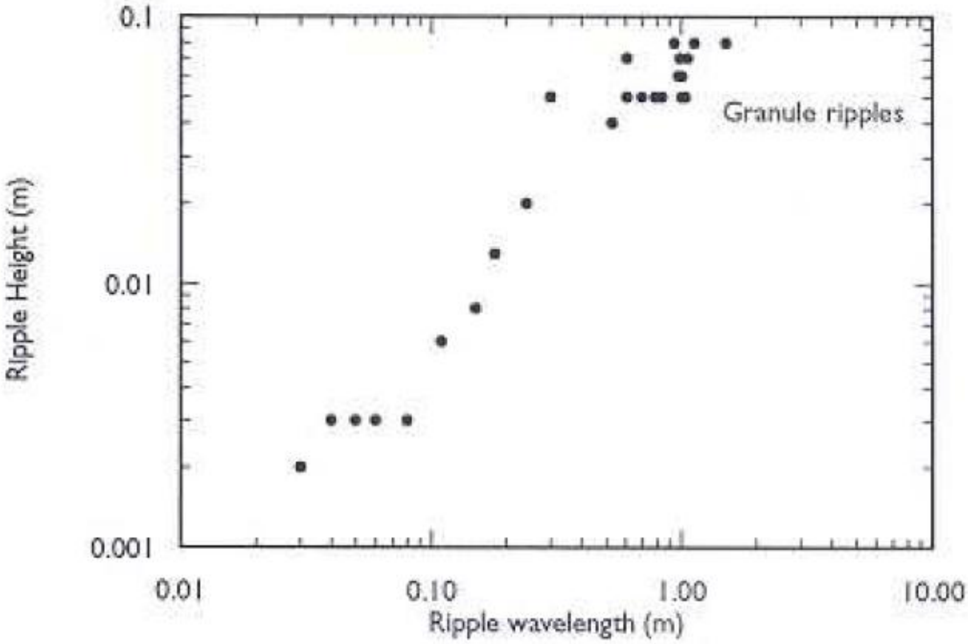

Figure 2.4. Ripple wavelength plotted against ripple height showing continuum between regular wind ripples to granule wind ripples. Source: Lancaster (1995).

A number of theories of ripple formation have been postulated, heavily influenced by the seminal work of Sharp (1963). Bagnold (1941) observed a correlation between ripple wavelength and calculated saltation lengths in wind tunnel experiments. He argued that a flat bed suffers irregularities caused by differing grain sizes and chance deformations which encourage areas of variable saltation impact intensities (Figure 2.5A). The areas of greater saltation impact intensities will cause grains to move up the stoss slope, causing hollows to enlarge. This in turn causes accumulation at the ripple crest, as grains are not moving down the lee slope as quickly as they are arriving. This then forms a second area of differing impact intensities and the pattern is repeated, thus areas of greater impact intensities propagate as ripples downwind. Bagnold (1941) suggests that the wavelength of the ripple field is determined by the ‘characteristic path’ or the average saltation hop length which reinforces the disparity experienced on a bed between impact intensities (figure 2.5B). However, Bagnold later questioned this ballistic hypothesis, which was disputed by Sharp (1963), who saw no evidence for a relationship between saltation path length and ripple wavelength during field experiments on the Kelso dunes in the Mojave Desert, California.

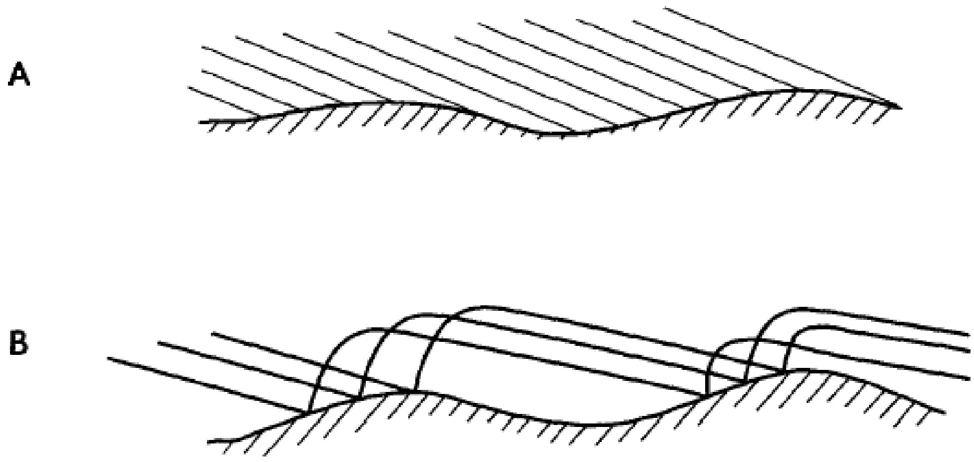

Figure 2.5. A showing areas of differing saltation impact intensities. Stoss slops receive a larger number of impacts compared to the less side of the ripple. B showing the relationship between saltation path length and ripple development suggested by Bagnold (1941)

Using these observations, Sharp (1963) proposed an alternative mechanism for ripple formation (Figure 2.6). Bed irregularities are formed and again create areas of differing saltation impact intensity. This heterogeneity in impact intensity deforms the bed, creating ‘proto-ripples’ (a). These proto-ripples create shadow zones in their lee (b) which are unaffected by saltation impacts. This encourages ripple growth, as the areas of high impact intensity are reinforced by reptating grains (c). Ripples then propagate downwind as grains are transported up the stoss slope of the ripple by reputation (the movement of surface grains due to impact from saltating grains) and are subsequently deposited on the lee side. The length of the shadow zone created in the lee of the ripple subsequently determines ripple wavelength and is a function of ripple height and wind velocity as this influences saltation impact angle (d).

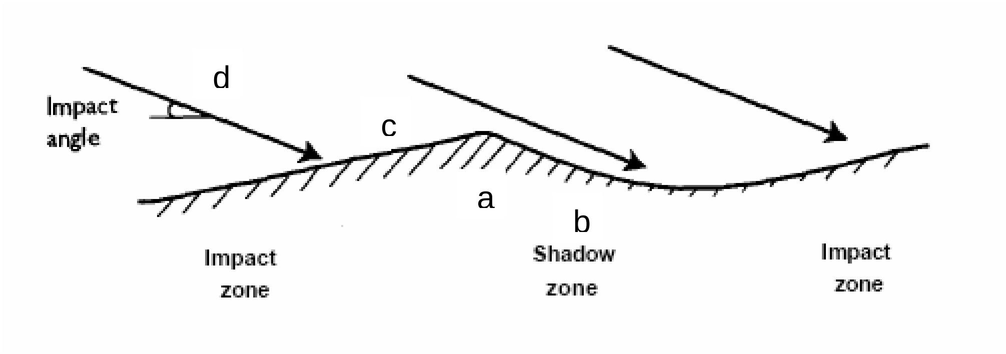

Figure 2.6. Schematic showing the alteration between impact and shadow zones suggested by Sharp (1963)

Larger grains make up the crest of the ripples moving by reptation, as smaller grains are entrained in saltation. Most ripples are homogenous, with little internal structure (Sharp, 1963). A small number of ripples display foreset bedding and typically consist of finer grains suggesting that these features are formed during periods of lower wind speeds. Earlier work (Bagnold, 1941; Norris and Norris, 1961) had suggested that ripple crests tended to consist of the coarsest grains. However Sharp (1963) observes that only a small increase in grain coarseness occurs towards the ripple crest, and the majority of the ripple is uniform in grain size. He argues that of more interest is the finer grains observed in the ripple trough, which is attributed to be the finer grained bed upon which the ripples are migrating.

Ripple migration occurs due to the angle of incoming saltating grains. Impacts from the windward direction cause grains to move downwind. Sharp (1963) observed individual grains moving up the stoss slope of a ripple by reptation. Once a grain has passed the crest, it is buried on the lee side and incorporated into the main ripple body by subsequent migration of other grains. Sharp envisaged that eventually the buried grain would remerge on the stoss slope, where the process is repeated again, and an individual grain could remain in one ripple cycle indefinitely (Sharp, 1963) (Figure 2.7).

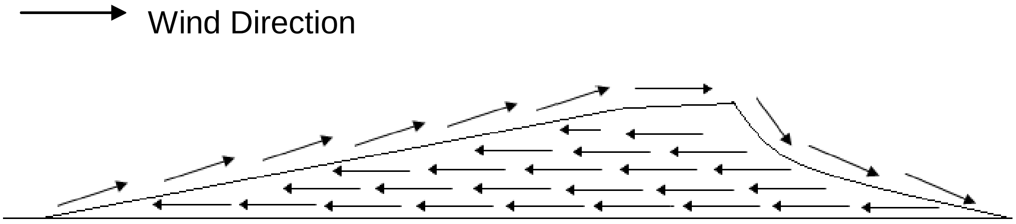

Figure 2.7: Schematic showing the idealised movement of sand grains (arrows) through a ripple. The grains moving through the ripple represent grain position relative to the movement of the ripple over them. They do not move backwards through the ripple, but re emerge on the stoss side after the ripple has migrated over them. After Sharp (1963)

In this way ripples migrate downwind. Smaller ripples travel at a faster rate than larger ones as it takes fewer reptation ‘hops’ for a grain to travel up and over a ripple (Hoyle and Woods, 1997). Hence smaller ripples are absorbed into larger ones until a quasi stable wavelength is reached for the grain size and shear stress. This is an example of bedform interaction which will be discussed in Section 2.4 (Page 24). Ripple migration rates have shown a good correlation with wind speed (r^2 0.86), and migration rates of 0.9-8.1cm per minute were reported by Sharp (1963). Ripple movement was initiated when the shear velocity reached around 0.38 ms^{-1} which is around the same velocity that the saltation system is initiated (Sharp, 1963) therefore the lowest migration speeds occur at the fluid threshold. These values are site specific and vary depending on sediment size. Ripple migration increases with wind speed until a maximum shear velocity of 1.30ms^{-1} is reached. At wind velocities this high, the surface flattens and ripples cease to exist. This process has been observed by both Bagnold (1941) and Sharp (1963). Sharp (1963) notes that at wind velocities this high, the creeping surface cannot be seen or defined.

Since the work of Sharp (1963) there have been very few field (Ellwood *et al.*, 1975; Lorenz and Valdez, 2011) or laboratory based (Anderson, 1990; Niedzielski *et al.*, 2006; Andreotti *et al.*, 2006) experiments concerning wind ripples. Anderson *et al.*, (1991) note that numerical modelling and theoretical based research on aeolian sand transport was on the verge of outstripping traditional field based approach. This trend has continued over the last 20 years, with research based around ripple simulation models becoming more widespread than field based publications (Werner and Gillespie, 1993; Hoyle and Mehta, 1999; Valance and Rioual, 1999; Csahók *et al.*, 2000; Miao *et al.*, 2001; Misbah and Valance, 2003; Zang and Miao, 2003; Yizhaq *et al.*, 2004; Andreotti, *et al.*, 2006; Manukyan and Prigozhin, 2009). Thus there is a developing need to collect field data in order to validate model output.

Anderson (1987) developed a model to study the generation of ripples from a flat bed. This was based on analytical work by a number of authors (e.g. Rumpel, 1985; Mitha *et al.*, 1986; Ungar and Haff, 1987; Willets and Rice, 1986) who looked at the interactions between particles and the bed at an individual grain scale. This reductionist model used the sediment continuity equation, calculating the spatial distribution in reptating grains and a probability of reptation hop distance. Initial conditions consisted of a slightly perturbed surface which was argued to be representative of natural undulations on a flat bed. Saltating grains were considered simply as an ‘external reservoir’, imparting energy equally to the entire bed. Anderson’s (1987) results suggest that the development and subsequent migration of ripples results from spatial variations in the reptation process and the related splash function, in agreement with Sharp’s (1963) hypothesis. Anderson (1987) showed that the fastest growing ripple wavelengths are six times the mean reptation length which is supported by field observations. Whilst the model performs well for initiation of a rippled surface from a flat bed, it diverges from reality once the ripples are developed and begin to migrate. Therefore it is unable to describe the increase in ripple wavelength observed in a natural setting (Manukyan and Prigozhin, 2009). A number of other assumptions inherent in the model also exist, such as fixed impact angle, and a homogenous grain population is used which is unrepresentative of a natural system.

To further study the interactions of fully formed aeolian ripples Anderson (1990) developed a numerical model to study ripples within the context of self-organisation. Self-organisation refers to the production of a complex pattern by relatively simple processes, a process displayed by wind ripples (Coco and Murray, 2007). The model improved on Anderson (1987) by adding a distrainment function whereby a reptating grain can continue to move providing the slope is steep enough. The results suggest that ripple wavelength increases rapidly after the transport system has been initiated due to the absorption of smaller faster moving ripples into larger ripples. The model also provides support to Sharp’s (1963) shadow zone theory, as ripple wavelengths appear to be controlled by saltation impact angle.

The self-organisation behaviour displayed by ripples is suited to a cellular automata modelling approach. Cellular automata are discreet models consisting of cells in a number of ‘states’. Rules representing fundamental processes manifest themselves in large-scale emergent patterns (Werner, 1995). Werner and Gillespie (1993) and Landry and Werner (1994) have developed cellular automata models to study ripple dynamics. Werner and Gillespie (1993) show that ripple wavelength increases linearly with time, before ripple mergers causes a reduction in the rate of increase and a subsequent stabilisation of the ripple system. They also find proportionality between grain size and ripple height which is consistent with field and wind tunnel observations (Anderson 1990).

Werner (1995) developed a dune evolution model where sand slabs are positioned on a discrete grid space to represent topography. Erosion and deposition of individual slabs are probabilistic, depending on the presence or absence of slabs in each eroding and depositing cell. Transport length is fixed at a user defined length as is transport direction, the angle of repose is set at 30° and a shadow zone is applied to the lee side of the slab stack at an angle of 15°. The model appears to replicate a number of different dune morphologies, with barchans, crescentic dunes, linear dunes and star dunes replicated by adjusting transport direction. This model is mentioned here as the Werner model is essentially non-dimensional. It is unclear whether the processes represented and subsequent landforms produced represent ripples or dunes (Nield and Baas, 2008). Both Wilson (1972) and Ellwood (1975) show a clear distinction between ripples and dunes in both their dimensions and formation mechanisms.

There have been a plethora of ripple models produced over the past 20 years, with the modelling approach typically being divided into cellular automata or reductionist continuum models. Werner and Gillespie (1993) argue that the continuum model approach is unsuited to modelling wind ripples, as they fail to capture the main self-organisation behaviour due to ripple merger. However this notion is disproved by Prigozhin (1999) and continuum models have been developed as a useful tool for analysing ripple dynamics. Hoyle and Woods (1997) extend Anderson's (1987) analytical model to include the rolling and avalanching of grains under the influence of gravity. The inclusion of an avalanching component appears to be questionable, as field observations suggest that ripples do not reach the sand angle of repose (Sharp 1963). The rolling of grains adds an important feedback whereby surface irregularities are smoothed out. Rolling, within this model, is the dominant process in the ripple shadow zone, a component of the model which Hoyle and Woods (1997) add to introduce a characteristic wavelength. When the shadow zone is not included then no characteristic wavelength is observed, which leads to the conclusion that the shadow zone governs the ripple wavelength. Another important finding is the impact of saltation intensity. They argue that the saltation intensity has to be above a certain threshold whereby the resultant reptating grains accumulate faster than they roll back to the bed under the effects of gravity. One weakness of the rolling component is that grain rolling is proportional to the slope angle. However, friction effects are excluded so rolling still occurs even on very shallow slopes. This is unrealistic and Hoyle and Woods (1997) are forced to acknowledge that ripples may form at lower saltation intensity thresholds than they predict. It also means that this model predicts that ripples cease to exist when saltation halts, as rolling would flatten the surface (Csahòk *et al.,* 2000). This again is unrealistic.

Prigozhin (1999) offers an alternate approach to representing the rolling and trapping of reptating grains by applying a simplified version of the Bouchard, Cates, Ravi Prakash and Edwards equation for sand flow and surface evolution (BCRE equation, Bouchard *et al.,* 1994). This equation is also utilised by Terzidis *et al.,* (1998), Csahòk *et al.* (2000) and Misbah and Valance (2003). The BCRE equation adds a component whereby grains at the top of ripple crests are more easily dislodged by impacting grains than those in ripple troughs. This is a logical process to model, but has been ignored in previous models where a uniform ejection rate is used. As a result, ripple merger displays different behaviour to previous models. Instead of simple merger of smaller ripples into larger ones, a different bedform interaction is observed. When a smaller ripple approaches a larger one, a 'two-headed ripple' is formed, from which the downwind head eventually splits from the feature as a smaller ripple and moves downwind. The ripple left behind is larger than both of the previous ripples. The smaller ripple migrates downwind and the process is repeated. This interaction has also been observed by Landry and Werner (1994) and is termed bedform repulsion by Kocurek *et al.*, (2010) however this process hasn't been documented in field studies concerning wind ripples. The model does, however, accurately show ripple coarsening and wavelength increase.

Vandewalle and Galam (2000) present an alternate ripple formation model which utilises an Ising spin model. The 'spins' are arranged onto a one-dimensional framework, and either represent a positive or a negative slope. Initial topography is random, and the surface evolves through saltation and avalanching only. Grain size is determined by pairing the spins, so each saltation hop results in two spin flips, and the dynamics proceed by spin pairs. A metastable ripple field is produced which is in agreement with previous work which use a cellular automata approach and shows correlation with field studies concerning subaqueous ripples. However this model has a number of flaws which call into question the results. The model does not have an explicit reptation component, which seems surprising considering the general consensus does suggest that reptation is the key process in ripple formation (Niedzielski, *et al.*, 2006). Furthermore a homogenous grain size is used and the saltation path length is fixed.

Yizhaq *et al.*, (2004) develop a variation on the Anderson (1990) model by adding the third dimension to consider ripples in two-dimensions. The third dimension is added by allowing reptating grains to be distributed at random angles and distances. This component is limited however by a lack of experimental data regarding the angular direction of the splash function (Andreotti *et al.*, 2002). The results show ripple defects and bifurcations which are common features in natural ripple beds. These features are also shown to propagate downwind and interact with other ripples in a way which is supported by sequenced images of sand ripples (Anderson and McDonald, 1990). The authors note that whilst the results share many common features with observations of natural ripples, they have avoided undertaking any detailed parameter fitting. This limits the results to qualitative discussions of model performance. Indeed, the model does differ from reality in two areas, namely that the model ripples do not disappear when subject to high winds and large amplitude bedforms are not accounted for. Reasons for these shortcomings in the model are not forthcoming within the literature.

Perhaps the most complete ripple model to date is proposed by Manukyan and Prigozhin (2009). Again it is a continuum model based on the work of Anderson (1990). The model employs a simplified BCRE type model, applying the findings of Sauerman *et al.*, (2001) to describe exchanges between the saltating cloud and the sand surface, and also accounts for a heterogeneous grain size population. As a result, a large number of ripple features are exhibited within the model such as the asymmetric shape, crest coarsening, growth saturation, grain size segregation and armouring layers.

Ripple models have yet to be incorporated into aeolian saltation models to create a more complete physical or analytical model of the entire aeolian transport system

(Baas, 2007). Saltation models ignore the effect of ripple formation on saltation, and ripple models ignore the increased roughness imposed on the wind by the ripples themselves. The nature of this feedback effect is not well understood. Baas (2007, pp 315) postulates that “the self-organised ripple field may ultimately induce a harmonic effect on the saltating layer”. How this effect manifests itself is unclear, with a correlated transport response or a chaotic response both possible. Variation in the spatial extent of the saltating layer may also drive crest termination and introduce bedform defects. Baas (2007) explores the validity of this link through a complexity analysis of the aeolian transport system. The approach used is the loop analysis of digraphs, first put forward by Puccia and Levins (1985). This involves identifying the positive and negative feedback loops within a system and the relative strengths of one over the other (Figure 2.8). If positive feedbacks are stronger than negative ones, the system is likely to display non-linear, chaotic behaviour. The four components are wind forcing, U, saltation flux, S, reptation, R, and ripple development, B. A number of assumptions are imposed in order for the Routh-Hurwitz stability criteria to function. These are, that reptation is not strong enough to maintain itself, that reptation is detached from the influence of the wind and that the ripple bed formation does not influence saltation. Whilst the first two assumptions appear likely, Baas (2007) concedes that a link between bedform formation and saltation is conceivable.

The analysis suggests that the system is inherently unstable, or at least meta-stable therefore chaotic behaviour is likely, supporting the conclusions of other work (McMenammin *et al.,* 2002). The analysis is limited however to a qualitative assessment of system dynamics. Whilst the wind, saltation and reptation can be quantified, Baas (2007) argues that quantifying the ripple morphology and subsequent 3D patterns formed is difficult, limiting the possibility of producing a quantifiable interaction matrix. Quantitative estimation of the link between bedform formation and saltation dynamics may provide the ability to undertake a fully quantitative Routh-Hurwitz criteria analysis of the aeolian transport system.

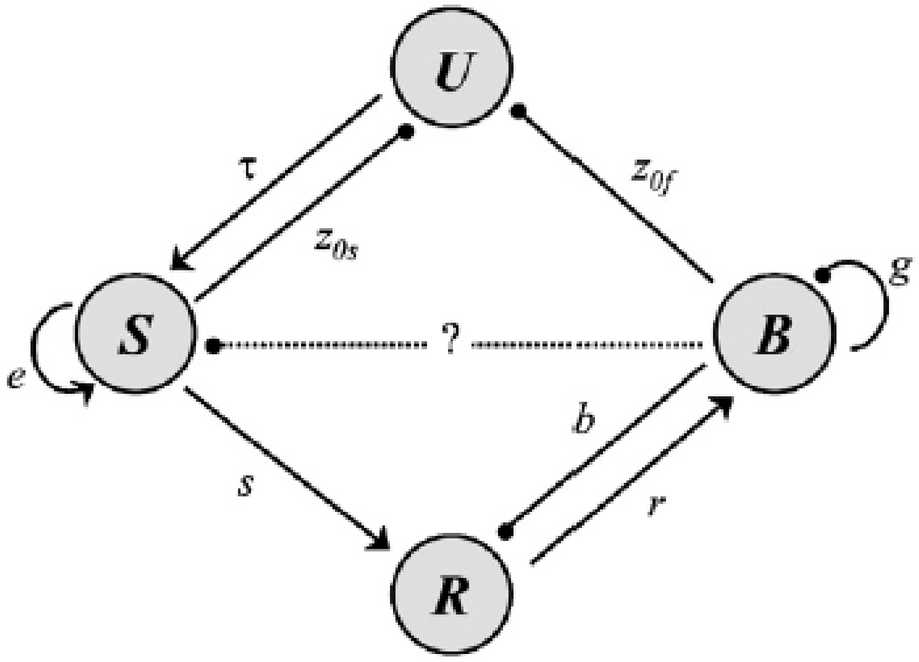

Figure 2.8. Digraph showing aeolian transport system. Arrows represent positive links whilst circles represent negative links. The dotted line represents a potential negative feedback link between bedform development and saltation. τ = shear stress driving saltation, z_{0s} = saltating grains extracting momentum from the wind, s= saltation driving reptation, r = reptation driving ripple formation, b= bedform growth limiting reptation, z_{0f}= bed morphology effecting shear stress through drag, e=positive saltation feedback through ejection and g = a negative feedback imposed by gravity on ripple extent. Digraph source: Baas (2007).

Whilst ripple models have provided useful insights into ripple dynamics, they have suffered from a lack of empirical data to validate model output. Indeed a number of authors have called for further empirical research into ripple dynamics to improve our understanding of aeolian transport system (Csahòk *et al.,* 2000, Yizhaq *et al.,* 2004, Manukyan and Prigozhin 2009), and to provide empirical data sets for purposes of ripple model validation (e.g. Andreotti *et al.,* 2006).

Measurements of ripple morphology in the field are difficult to obtain due to their small scale (Werner *et al.,* 1986). A number of different techniques have been developed. Early research relied on measuring ripple crest heights and wavelengths with thread (Cornish, 1933). Plexiglass sheets have been laid across ripples to measure trough depth wavelength (Sharp, 1963). Sharp also fixed a number of ripples using a glyptol solution to extract them from the field and study internal ripple stratigraphy. Plaster of paris moulds from in situ sub aqueous ripples have been taken (Allen 1969), however this appears unlikely to have the desired results if applied to aeolian ripples due to their fragile nature. Stereophotography has been applied to produce topographic maps of ripples created in a wind tunnel (Seppalla and Linde, 1978). However, this procedure is argued to be too delicate for application in the field (Werner *et al.*, 1986) and requires a significant amount of data reduction. Werner *et al.*, (1986) develop a method of capturing in-situ ripple morphology known as the shadow-cast technique. Light is reflected by a mirror onto a straightedge, which then casts a shadow onto the perpendicular ripple bed. The shadow is then photographed which records the ripple shape relative to the straight edge. Post processing of these photographs allows ripple height calculation as a function of trough to trough distance. This method provides morphologic data useful for comparing ripple metrics; however it has a number of shortcomings. Firstly photograph digitisation is likely to introduce errors to overall height obtained. Secondly, only two adjacent ripples can be measured at any one time due to the small extent of the straight edge. Thirdly, the requirement of a natural light source means this technique is dependant on current weather conditions. Using this technique in overcast conditions may not be possible. Niedzielski *et al.*, (2006) extend the Werner *et al.*, (1986) study by using a longer straight edge to enable concurrent measurements of seven adjacent ripples. However, the shadow cast technique is inherently limited as the height is only recorded at one point along the ripple extent which may not be representative, especially if the defect or bifurcation densities are high. This method is also limited to two dimensions, so does not capture the three dimensional nature of the features. The results of both shadow cast technique papers appears to have been largely ignored within the wider ripple modelling literature.

Due to these limitations, there is a need for further empirical data to validate the results obtained within the ripple models. A more accurate representation of surface topography would provide more detailed ripple analysis. Furthermore, the ability to capture surface topography during active saltation may provide knowledge regarding feedback loops between ripple development and the saltating layer. The ability to capture sequential surface topography during ripple field evolution would provide data, to which ripple models could be validated.

2.4 Proto Dunes

There is a general consensus that wind ripples do not continue to develop into dunes. Fundamental differences in the initiation of dunes and ripples have been described in the literature (Lancaster, 1995). Ripple formation is the first response of a sand surface to sand transport, whilst dunes are thought to form as a result of wind speed reduction due to changes in aerodynamic roughness, micro topography, erosional depressions, relict topography or vegetation (Kocurek *et al.,* 1992). This encourages deposition and, provided there is a large enough sediment source, proto-dune formation begins. Kocurek *et al.,* (1992) propose five stages of dune evolution, with the final stage being a dune with an angle of repose and airflow separation on the lee side. Very few studies into the formation of proto dunes have been undertaken (Lancaster, 1995; Lancaster, 1996; Momiji *et al*., 2002; Nield *et al*., 2011;), despite being of major importance to how dune and dune field patterns emerge. There is therefore a need to provide further empirical data regarding the processes involved in dune initiation. Again this calls for a more detailed understanding of the surface topography, collected on a temporal scale low enough to link form and process (Baas, 2008).

2.5 Bedform Patterns

The patterns formed by aeolian bedforms are indicative of self-organised behaviour, as a pattern emerges from random state (Hallet, 1990). Self-organisation can be indicative of a complex system, when displayed in an open dissipative system with energy sources and sinks, that consists of a large number of elements that themselves display non-linear behaviour. The aeolian sediment transport system fits these criteria, and is regarded as a classic complex system (Werner, 1995, Baas, 2007, Coco and Murray, 2007). Two main theories exist for self organised behaviour. The reductionist hypothesis suggests that large scale patterns are a result of the summation of small scale processes (Werner, 1995). In contrast, the self-organisation hypothesis suggests it is the interactions between bedforms themselves that give rise to the self-organised pattern (Kocurek *et al*., 2010). The self-organisation hypothesis argues that the wind ripple pattern governs the sediment transported over them. Kocurek *et al.,* (2010) note that whilst bedform interactions give rise to large-scale patterns, the understanding of these interactions is limited, and represents a knowledge gap. Interactions between bedforms, the influence of the bedform on the flow field and metrics for pattern analysis are not well developed. This is largely due to the low number of time series data sets concentrating on bedform pattern development and interactions. Three main bedform interactions exist, (i) those involving whole bedforms, (ii) the effect of bedform defects, and (iii) remote interactions where bedforms do not meet, but modify the down wind flow (Hallet, 1990; Kocurek *et al*., 2010). A spectrum of specific interactions exist, ranging from constructive to regenerative interactions. Constructive interactions, those which reduce the number of bedforms within a system, increase bedform wavelength, crest length and height. Regenerative interactions increase bedform density through either bedform splitting or the generation of entirely new features. A summary of the interactions proposed is shown in Figure (2.7). However, it is important to note that these interactions are idealized, and represent not only wind ripple interactions, but span a range of bedform fluids and types.

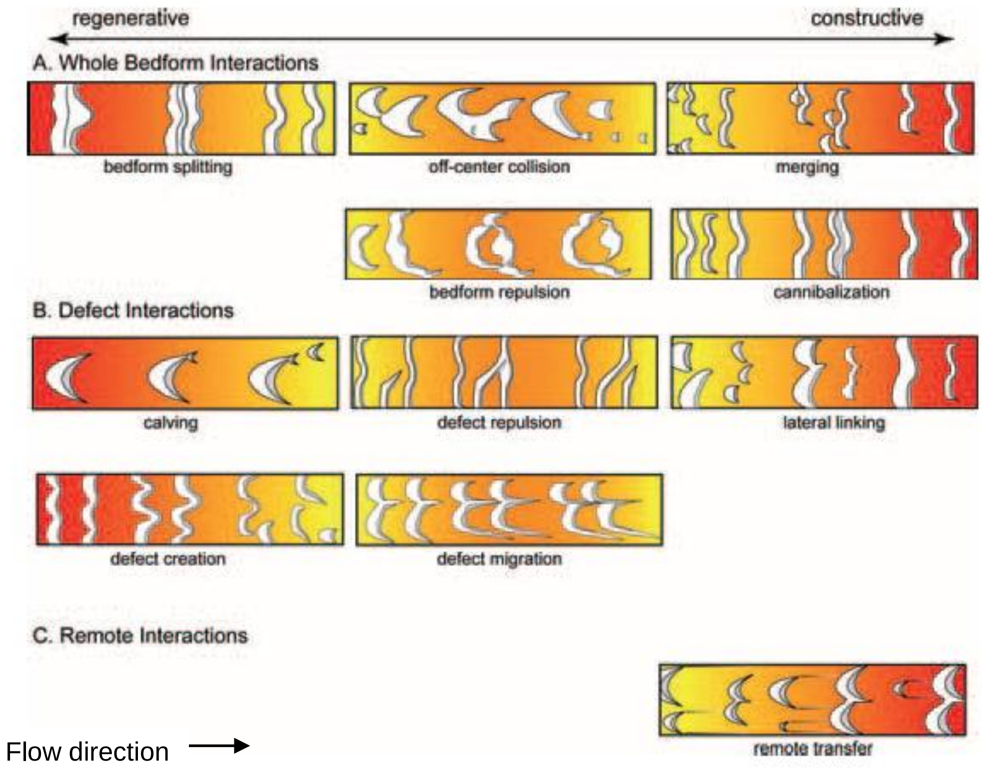

Figure 2.9. Schematic highlighting the different types of bedform interaction. Source: Kocurek *et al*., 2010.

Diversity in natural bedform patterns arise as a result of a diversity of boundary conditions (Landry and Werner, 1994; Ewing and Kocurek, 2010). These are the environmental variables which influence the evolution of the bedforms. Whilst these are largely similar within system types, the differences are thought to account for the variety observed in bedform fields to the point where each is thought to be unique. Werner (1995) demonstrates this using a phase space diagram showing the trajectory of different dunescapes towards a particular attractor from a broad range of initial conditions. There are five different boundary conditions which influence the attractor a system will evolve towards; (i) the wind direction (influences crest orientation), (ii) the nature of the sediment supply (will produce different dune types), (iii) geometry of the sediment source area (again will govern dune type), (iv) spatial limits of the bedform field (may influence optimal dune size), and (v) pre-existing conditions (Ewing, *et al.*, 2006; Coco and Murray, 2007; Kocurek *et al.*, 2010). Ewing and Kocurek (2010) demonstrate the role of two boundary conditions, areal extent and sediment source geometry, on pattern development. This later study analyses the crest spacing and length from a number of dunefields processed using satellite images. The results suggest that point and line source geometries produce increasing bedform wavelengths and crest lengths with downwind distance, whilst plane sources show equal spacing through the system. The effect of areal extent of the dune field is a limit on the maximum possible spacing between dunes. As noted, linking boundary conditions to pattern formation is in its infancy and, to the author's knowledge, has not been undertaken for aeolian ripples. Anderson and McDonald (1990) provide images of ripple fields evolving, but this is only to analyse bifurcation and defect progression.

There is a need for quantitative data regarding not only bedform morphology, but the development of the bedform field and the dynamic feedback effect between the saltating layer and the bed. These interactions ultimately influence the patterned state produced. Moreover, it would be beneficial to analyse these parameters whilst active transport is occurring. In order to develop a complete overview of the aeolian transport system, accurate in-situ surface wind measurements are also required to relate bedform development to flow conditions.

2.6 Surface Winds

Aeolian transport occurs when there is an availability of sediment capable of being transported by the wind (typically particles ranging from 60-2000 μm in diameter) and a surface wind strong enough to entrain these particles (Greeley *et al.*, 1996). Wind is the result of atmospheric pressure differences which, on a global scale, are created by differential heating between the poles and the equator and the effect of the Earths rotation. Only the surface wind is important when considering aeolian transport on a scale relevant to specific bedforms. Airflow is typically turbulent and consists of eddies moving at different speeds and in different directions (Baas and Sherman, 2005). These eddies are typically organised into layers which transfer momentum from one to another, resulting in a shear stress (τ) being applied to the surface:

$$\tau = \rho u_*^2 \tag{2.1}$$

Where ρ is the air density (typically 1.22kg m^{-3} at sea level) and u_* is the shear velocity (m s^{-1}). A thin (< 1mm) laminar sub flow layer forms when air flows over a surface consisting of fine sediments (< 80μm) which is replaced by a viscous sub-layer when wind flows over an aerodynamically rough surface (>80μm) defined as a surface where the turbulent boundary layer reaches the surface due to surface irregularities (Lancaster, 1995). The velocity profile above this sub-layer has been shown to typically obey the logarithmic law of the wall:

$$\frac{u}{u_*} = \frac{1}{k} ln \frac{z}{z_o} \tag{2.2}$$

Where u is the wind speed (ms^{-1}) at elevation z (m) above the bed, κ is the von Karman constant (0.4) and z_o is the aerodynamic roughness length (m). Estimates of z_o and u_* are typically calculated using regression analysis of measured vertical velocity profiles (Sherman and Farrell, 2008). The aerodynamic roughness length represents the height at which the wind profile, plotted on a logarithmic axis, intersects the y axis over a time averaged period (Lancaster, 1995).

Surface winds have been shown to be non uniform under natural conditions, containing gusts and fluctuations across spatial and temporal scales (Wyngaard, 1992). Turbulent structures in the wind create burst-sweep events which create high temporal and spatial variability in aeolian sediment transport (Bauer *et al.*, 1990). Sterk *et al.*, (1998) documented high saltation intensities during such events, which accounted for 60% of the study periods' average shear stress, despite occurring for 20% of the time. These coherent structures are difficult to predict or indeed measure, due to their three dimensional and chaotic nature (Bauer *et al.*, 1998; Baas and Sherman, 2006). As a result, predicting sediment entrainment and overall transport rate has proved difficult.

2.7 Aeolian Transport Equations

Current predictive models relate aeolian sediment transport rates (q) to a cubic term of shear velocity. The seminal work of Bagnold (1941) has provided the theoretical background for nearly all the subsequent research regarding aeolian transport rates. Bagnold proposed that the mass flux could be calculated using:

$$q = \sqrt{C\frac{d}{D}}\,\frac{\rho}{g}{u_*}^3 \tag{2.4}$$

where d is the mean grain diameter (mm), D is a reference grain diameter of 0.25mm, C is a sorting coefficient ranging from 1.5-3.5 dependant on sand grading, with 1.8 representing naturally graded dune sands, ρ is sediment density (kg m^{-3}). This equation is the most widely used and represents a simple, non-stochastic approach, however, the fundamental issue with this equation is that it does not include a threshold shear velocity term, therefore predicts transport even when shear velocity is below the threshold needed for the initiation of grain movement (Sherman *et al.*, 1998). Kawamura (1951) was the first to include a component for threshold shear velocity, u_{*t}:

$$q = C\frac{\rho}{g}(u_* - u_{*t})(u_* + u_{*t})^2 \tag{2.5}$$

This model performs well at higher shear velocities, however Kawamura suggested a fixed value of 2.78 for C which was later shown to limit the predictive capabilities of the model by Horikawa *et al.,* (1984).

Zing (1953) puts forward another transport equation which is essentially a reproduction of the Bagnold (1941) equation (4).

$$q = C\left(\frac{d}{D}\right)^{\frac{3}{4}} \frac{\rho}{g} u_*^3 \tag{2.6}$$

Where C is a fixed value of 0.83 regardless of surface sediments. This equation has been shown to consistently underestimate sediment transport, when compared with both field measurements, and predictions from other equations (Sherman *et al.*, 1998).

The Kadib (1965) model makes use of a transport intensity function (ɸ) based on Einstein’s bedload transport model:

$$q = \phi \rho_s g \sqrt{\frac{(\rho_s - \rho)}{\rho} g d^3} \tag{2.7}$$

Lettau and Lettau (1977) developed a model based on experiments in arid environments, in which C is given a value of 4.2:

$$q = C\sqrt{\frac{d}{D}\frac{\rho}{g}}(u_* - u_{*_t})u_*^2 \tag{2.8}$$

The above equations represent some of the most widely applied aeolian transport equations. Whilst other aeolian transport models exist (Hsu, 1973; White, 1979; Horikwa *et al.,* 1984; Chapman, 1990; and McEwan and Willets, 1994), the above represent the most commonly utilised and tested equations. These equations have been shown to estimate transport to within an order of magnitude when undertaken in ideal conditions. (Greeley *et* al., 1996). Ideal conditions are considered as a wide horizontal bed, with the absence of moisture, vegetation and anthropogenic influence (Baas, 2008). The Bagnold equation has been shown to be the most reliable way of estimating sediment transport (Sherman *et al*., 1998). However when these models are compared against empirical field observations, their performance is poor (Figure 2.10) (Haff, 1996; Arens, 1996; Sherman *et al*., 1998; Liu *et al*., 2006). The Bagnold model for example, has been shown to over predict mass flux by ratios of 3:1 to 300:1 (Bauer *et al.,* 1990; Nordstrom and Jackson, 1992). Sherman *et al*., (1998) found the Zing (1953) equation provided the best results when compared to field measurements of transport.

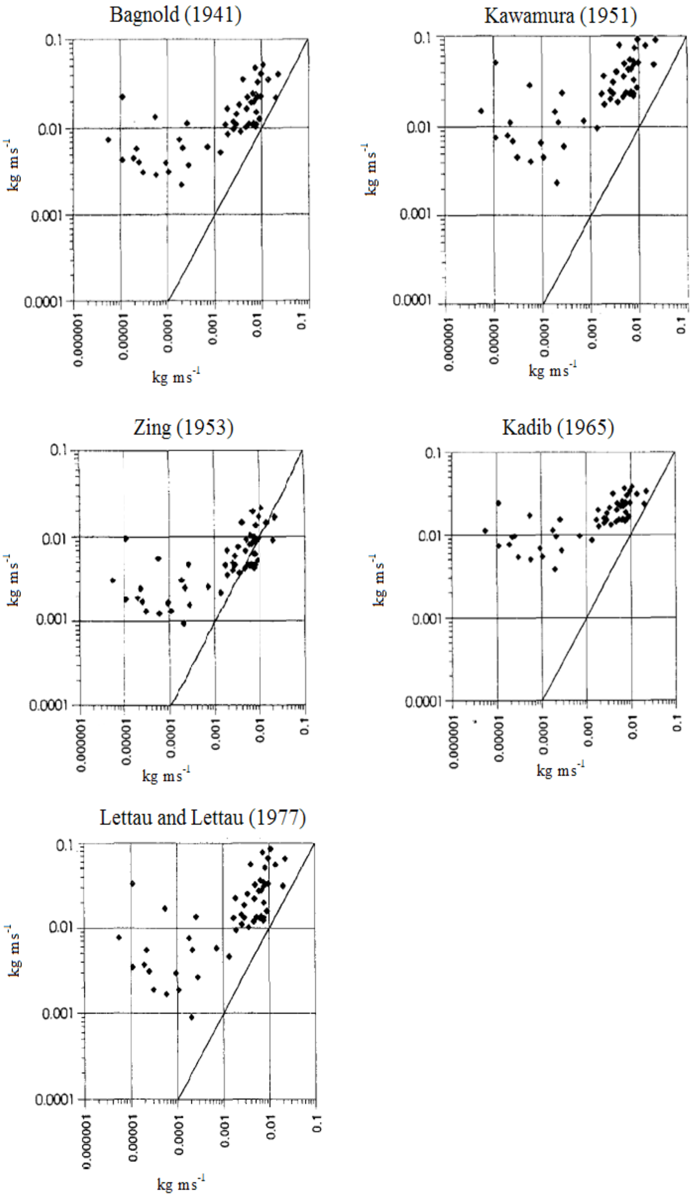

Figure 2.10 Comparison between predicted sediment transport equations and observed sediment transport in the field (After Sherman *et al*., 1998). Sediment transport was measured using a Leatherman (1978) cylindrical trap.

A number of corrections exist to account for site specific variations that effect overall transport rate. The most common corrections are for slope or moisture effects (Bagnold, 1973; Iverson and Rasmussen, 1994). However, Sherman *et al.,* (1998) note that the improvement offered by slope correction equations are minimal unless the slope exceeds 15°. Several corrections for moisture have been developed, however these yield large ranges in the results which suggests that the corrections applied are largely site specific (Namikas and Sherman, 1995; Namikas *et al.,* 2010). The reason for the observed discrepancies between predicted values and measured values is not evident. A number of explanations for these discrepancies have been offered, the most obvious being inadequate transport formulae, or incorrect application of these formula (Bauer and Davidson-Arnott, 2002). Comparing equations with field measurements presumes a level of accuracy in the ability to accurately measure sediment transport in the field. However, there are also numerous difficulties in measuring aeolian transport, such as trap inefficiency, disturbance to the surface wind and assumed spatial homogeneity in sand transport (Jackson *et al*., 2006) despite evidence to the contrary (Baas and Sherman, 2005). Due to these factors, it is difficult to determine whether predictive transport equations perform poorly due to the equation itself, the sand traps deployed or a combination of the two.

2.8 Measuring Aeolian Transport

A variety of methods have been employed to measure mass flux. Vertical sand traps are the dominant method employed to collect mass flux data due to ease of use and low cost (Jackson 1996b). These traps exist in a variety of forms such as wedge shaped (Nickling and McKenna Neuman, 1997) and cylindrical (Leatherman, 1978) although all attempt to capture sand in compartments at various heights within the saltating layer (Ellis *et al.,* 2009a). This protrusion into the wind field significantly affects the ability of the trap to capture saltating grains due to interference the wind flow. Scour at the base also reduces the ability for the trap to capture grains moving by either reptation or creep (Wang and Kraus, 1999). Stagnation zones at the trap entrance can be created by the generation of back pressure and eddies. Isokinetic traps are preferable in this regard, as wind speed through the trap is equal to the ambient wind speed. This minimises the distortion of particle trajectory (Goosens *et al*., 2000).

Active isokinetic samplers draw in air and therefore sediment at a rate adjusted to the wind speed. These traps are thought to offer the best efficiency, yet are costly and suited to wind tunnel experiments where wind speed can be kept artificially steady (Goosens *et al*., 2000).

Ellis *et al.*, (2009a) point out that there is no standard protocol for the measurement of mass flux using vertical traps. Trap heights are inconsistently represented as trap openings span several centimetres, yet only a single elevation is used to represent them. The regression analysis performed in previous studies are shown to be inconsistent and bed heights are ambiguously recorded. Changes in wind direction also limit the effective trap width which again reduces the effectiveness of the trap (Illenberger and Rust 1986). Vertical trap efficiencies as low as 15% have been reported by Arens and van der Lee (1995). Namikas (2003) argues that traps perform well at heights above 10mm, however the lower compartments consistently under-represent mass flux. These observations are supported by Li and Ni (2003) which suggests that the creep and reptation components of flux are systematically ignored when using vertical traps, thus the primary transport component of ripple migration are underrepresented. Ripples are likely to migrate beneath the sand trap due to scour at the base, thus their contribution to mass flux is ignored.

The use of horizontal traps removes measurement errors associated with vertical traps as wind field disturbance is removed (Jackson, 1996b). This method gives a total sediment flux, but no means of calculating the proportions of saltation and bedform flux. Traps of this type are difficult to install as they are typically at least one saltation hop length in width to ensure grains do not miss the trap while entrained in transport. As a result the traps are large, difficult to install and have a reduced functionality as changes in wind direction limit the traps ability to capture sand. The subsequent weighing of sediment can be difficult in the field (Pye and Tsoar, 1990, Wang and Kraus, 1999). Jackson (1996b) provides an alternative approach utilising a compact (24cm diameter), circular, continually weighing horizontal trap. The size allows the trap to be installed quickly, whilst the weighing element provides the ability to relate sand transport to wind speed recordings. However, this trap is reliant on the assumption that sand transport is homogenous over a given area, which the findings of Baas (2004) would dispute.

The temporal resolution of sediment traps is also problematic. Traps require an extended period of time to allow enough sediment to be accumulated. While automated weighing systems (such as Lee, 1987; Jackson 1996b and Bauer and Namikas, 1998) have offered an improvement to the temporal resolution, traps still remain insufficient for capturing small scale aeolian processes (Ellis *et al., 2009b*). Wind tunnel investigations have shown the response time of the saltating system to wind flow fluctuations is in the order of 1 to 2 seconds (McEwan and Willets 1991, Butterfield 1998, Spies *et al.,* 2000). Therefore to capture processes at this temporal scale, sensors with much higher monitoring resolutions are required. Butterfield (1998) deployed an optical mass flux sensor which operated at a 40Hz sampling rate and is non intrusive to the wind field, though this instrument has only been deployed in the laboratory. Stockton and Gillete (1990) apply the Sensit, a piezo-electric crystal based sensor which has been applied successfully in the field (Gillete *et al., 1997*) but this instrument is expensive. The Saltiphone (Spaan and Van den Abele, 1991) is a microphone based sensor which again can be utilised in the field (Arens, 1996, Sterk *et al.,* 1999). However both the Saltiphone and the Sensit are based on the momentum imparted by the saltating grain rather than individual impacts which makes it difficult to relate the response to an overall mass flux rate (Barchyn and Hugenholtz, 2010). The Safire (saltation flux impact responder, Baas 2004) again utilises piezo-electric technology and records individual grain impacts, and is relatively cheap compared to the Sensit. A correlation within an order of magnitude is shown between mass flux rate calculated from the Safire and a sand trap, despite making a large number of assumptions (Baas 2004). These instruments however are not omni-directional so are affected by changes in wind direction and the maximum impacts per second is limited to 200. Careful calibration is also required to relate the responses of multiple Safires in an array (Baas 2004, Baas 2008), and only impacts by grains greater than 0.4mm in diameter are recorded (Baas and Sherman 2006). Ellis *et al.,* (2009b) utilise a miniphone to detect individual saltation impacts as an alternative to Safires. This device is cheap ($10) so can be deployed in high numbers and is relatively successful in detecting impacts. However the device itself is degraded rapidly when placed within the saltating layer, to the point where the sensor melts after around 20 minutes.

Inconsistencies between different models of saltation impact sensors (SIS) have been demonstrated in a number of investigations (Baas, 2004; Van Pelt *et al*., 2009). These discrepancies limit the usefulness of comparison between studies utilising different SIS.

Van Pelt *et al*., (2009) compare the effect of sediment size at different wind speeds on the sensit, safire and saltiphone responses. Threshold sediment size detection was different for all three sensors. The efficiencies of the sensors also improved with increasing wind speed which demonstrated a variable threshold detection level. This is a result of the momentum imparted by the grain impact, which is a function of particle mass and velocity. This study was conducted in a laboratory wind tunnel which makes relating the synthetic response sensitivity to field response sensitivity difficult (Baas, 2004). A direct comparison between sensors employed in the field is offered by Barchyn and Hugenholtz (2010). In this study, four different piezo-electric SIS (three different sensit models and a Safire) were deployed 5-10cm apart in a row. The study concerned sediment transport detection during an 11 day run. The sensor results showed large variability, with transport detection ranging from 0.089% to 7.212% of the total run time. Whilst each SIS had a different minimum particle momentum, the authors argue that this alone cannot account for the discrepancy observed. SIS only detect grains being transported by saltation, so will not detect transport by other mechanisms. As a result, ripple migration is also not detected when using SIS.

There have been few studies concerning the spatial variability of aeolian sand transport. Typically one trap is deployed in the field which is assumed to be representative of the mass flux over the study area. However, transport variability of 50% (Gares *et al.,* 1996) 200% (Jackson *et al.,* 2006) and 266% (Baas and Sherman, 2006) have been recorded when multiple traps or sensors have been deployed in the field. Variability of this extent suggests that gaining an accurate picture of in-situ aeolian sediment transport is difficult. As a result this limits our ability to accurately model sediment transport. Spatial variability in transport manifests itself in spatial variability in bed deformation, and gaining an accurate picture of the aeolian sediment surface is desirable for a number of applications as discussed previously. An alternative method to calculating aeolian transport is presented below.

2.9 Morphologic Method

Given the limitations of traditional techniques for measuring aeolian transport, reviewed above, it is worth considering the merits of an alternative approach to estimating total mass flux, namely the morphologic method. In this technique, mass flux is estimated using the principle of conservation of mass. In this approach repeat topographic surveys are undertaken, which can be used to produce digital elevation models (DEM). Provided the spatial extents match, the later DEM can be subtracted from the former to provide a total volumetric change (Figure 2.10) (Brasington *et al.*, 2000). The time and space average transport rate can then be determined using the mass continuity equation:

$$QS_0 = Qs_i - \rho s\ \Delta V/t \tag{2.9}$$

Where Qs_i and QS_0 are the volumetric sediment flux into and out of the study area, ρs is the sediment density, ΔV is the volumetric change in sediment storage, and t is the time interval between studies. Depending on this time interval, this method can be employed to study event based transport rates or longer term sediment budgets. This is also inherently dependant on the spatial resolution of the method utilised to collect the topographic data. Coarse resolution methods require longer time periods or the occurrence of significant geomorphic events between surveys to allow change detection (Brasington *et al.*, 2003).

The morphologic method has largely been developed within fluvial geomorphology (Fuller *et al.*, 2003; Wheaton *et al.*, 2010) and has followed developments in topographic mapping techniques. This technique has been applied in the field to study braided rivers (Lane *et al*., 2003) wetlands (French, 2003) floodplain systems (Charlton *et al*., 2003) and proglacial rivers (Milan *et al*., 2007). The morphologic method has also been applied to laboratory experiments, where small scale physical models are used to study channel incision, threshold hydraulic conditions and as analogues for drainage basin systems (Stojic, *et al*., 1998; Hancock and Wilgoose, 2001; Brasington and Smart, 2003). Assement of bedload transport formulae has also been undertaken using the morphologic method (Lane *et al*., 1995; Martin and Church, 1995). Martin (2003) tested various bed load transport formulae over decadal time scales on the Vedder River. Repeat cross section surveys covering an 8000m stretch of river were used to elucidate volumetric change over the study period, with formulae underestimating the amount of sediment transport that had occurred.

More recent developments have seen the use of new technologies to gather topographic data for change analysis at much higher spatial resolutions. For example, Nitrouer *et al.,* (2008) utilised a multibeam swath profiler to collect bathymetric profiles within the Mississippi River. Bed elevation changes as a result of subaqueous dune migration were measured daily and DEMs of difference (DoD) were produced to highlight dune migration rates and areas of change. Bedform flux associated with dune migration was also calculated (Figure 2.11). Utilising this methodology with techniques suited to an aeolian bedform field could provide the ability to constrain the proportion of reptation and creep towards total mass flux.

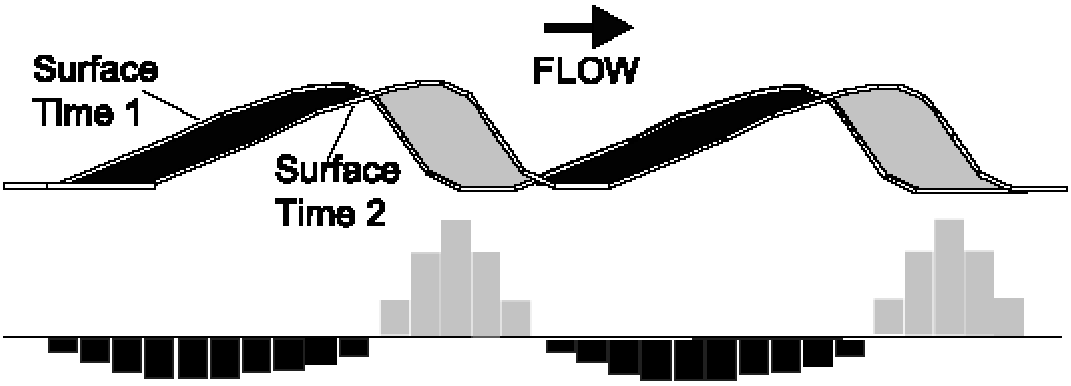

Figure 2.11. Schematic showing the elevation changes associated with bedform migration. Areas of black represent erosion whilst grey represents deposition. After Nitrouer *et al.,* (2008).

This methodology, in contrast to fluvial geomorphology, has been applied to relatively few aeolian studies. Arens (1997) used ranging poles to create four DEMs of a 250x 50m area of the Schiermonnikoog coastal sand dune in the Netherlands. The periods between the surveys ranged from two weeks, to three months, and continuous meteorological data was recorded along with saltation intensity recordings from a Saltiphone. These instruments allowed calculation of a predicted transport rate based on the White (1979) transport equation, to be compared with volumetric change calculated from differencing the DEMs. The results show a large disparity between volumetric changes observed and predicted sand transport (2.1m^3 observed, 18.0m^3 predicted to be delivered to the study area) even after site specific corrections are applied. Arens (1997) notes that the predicted volume of sand transport is the maximum potential transport that could occur for a given wind speed. This is rarely met in natural conditions due to the effects of other environmental variables such as surface moisture, rainfall, fetch distance and slope angle. Sherman (1995) points out that only sediment that is deposited in the dune will be detected by volumetric change analysis, as the bulk of the sediment is transported to outside the study area. Another potential reason is the field set up employed. Saltiphones were only installed at two locations in the 250m by 50m study area which, given the above conclusions concerning spatial variability in aeolian sediment transport, is limited. The 5m pixel size used is also a rather coarse resolution to use to represent the dunes and subsequent volumetric changes. Topographic recordings were taken at obvious changes in the slope angle which introduces operator bias into the research. Interpolating these points onto a 5x5m grid means that only extreme changes in the dune profile over the study period will be represented.

Woolard and Colby (2002) show that resolutions used to represent coastal dunes should not be larger than feature it is representing. In their study, airborne LiDAR (Light detection and Ranging) is used to collect topographic data over two 100 x 200m study zones in Cape Hateras, North Carolina. Two surveys were undertaken, separated by 12 months, to construct two DEMs of the dunes which can then be differenced to calculate an annual sediment budget. Data collection is automated so operator bias is removed, and the 1m resolution applied offers a significant improvement on the study by Arens (1997). However the high cost of collecting such data, coupled with the reported accuracy of 15cm means that linking data of this type with short scale spatial and temporal changes in aeolian transport is not feasible.

The morphologic method is limited by the inherent uncertainty associated with the individual DEMs used. This level of uncertainty is influenced by the survey method used, and is important to consider when trying to detect meaningful change. Errors in DEMs will propagate when a DEM differencing operation is undertaken (Lane *et al.*, 2003; Lane and Chandler, 2003). If the errors associated with a point within the DEM of difference (DOD) are greater than the change that point is representing, then it is difficult to separate geomorphic change from the background noise. Errors in DEM surface representation can arise in a number of ways such as survey point quality, method of interpolation, surface complexity, and sampling strategy (Wechsler and Kroll, 2006). Developments in survey technology have increased surface point quality, and enabled higher resolution surface data to be collected (Wheaton *et al*., 2010). Such advancements may now provide the opportunity to link surface form and process in aeolian environments at a spatial resolution greater than previously available. Terrestrial laser scanning is an emerging high resolution survey technology that offers the ability collect high resolution surface data quickly, and with little, if any, disturbance to the surface of interest (Heritage and Hetherington, 2007).

2.10 Terrestrial Laser Scanning

Terrestrial laser scanning (TLS) offers an alternative approach to traditional survey equipment, capable of capturing topographic data at spatial and temporal resolutions small enough to link process and form in aeolian environments. TLS utilises electro-optical distance measurement to obtain a point cloud of a required surface. The distance of each point from the scanning position is calculated using either phase difference or a time-of-flight laser pulse (Hodge, 2010). In phase difference scanning, a continuous laser beam is emitted between a transmitter and receiver. The phase difference is recorded, and the distance is calculated by using the time taken for light to travel equal to one wavelength. Time-of-flight systems record the time taken from the emission of a laser pulse, to its return having been reflected from the scan surface along with scan angle to produce an x,y,z coordinate (Heritage and Large, 2009). Time-of-flight systems are the most commonly used due to their superior range. TLS of a sediment surface can collect data capable of producing DEMs with millimetre resolution, at rates of up to 50,000 points/second (e.g. Leica Scanstation 2). Originally designed for use in structural engineering, TLS is increasingly being utilised in a host of geomorphic applications such as monitoring cliff retreat (Rosser *et al., 2005*; Lim *et al.,* 2006), volcanic forms (Pesci *et al.,* 2007) investigating rock falls (Pieraccini *et al., 2006*) tree morphology (Antonarakis *et al., 2009*) and fluvial environments (Heritage and Hetherington 2007; Milan *et al., 2007*).

TLS has been applied in a number of aeolian environments, principally to study desert dunes or coastal dunes. Nagihara *et al.,* (2004) use TLS to capture barchan morphology in White Sands, New Mexico, in a study concerning the feasibility of applying TLS to capture dunes. Point density was set at 10cm at a distance of 60m, and 260000 points were collected over a 2500m^2 area, by registering 11 scans to a common coordinate system. Positional error was calculated as 3mm, by taking high resolution scans of registration markers. Ochoa (2005) utilises TLS and the morphologic method to map and calculate volumetric change associated with a barchan dune migration at White Sands over a twelve month period. Scan point spacing was set at 2cm, and the barchan was observed to increase in size by 150m^3. Pietro *et al*., (2008) study the performance of a beach nourishment scheme in Delaware using TLS. Volume estimates are calculated from subsequent scans and highlight areas most susceptible to change during storm events.

The above studies have focussed on capturing small scale features within large scale systems. More recently, work has been carried out to collect sub-centimetre elevation data in vegetation (Clawges, 2007; Eitel *et al*., 2010), surface roughness (Eitel *et al*., 2011; Sankey, *et al*., 2011) and fluvial (Hodge *et al.,* 2009a; Hodge *et al.,* 2009b*;* Hodge *et al.,* 2010; Wang *et al*., 2011) studies. Hodge *et* al., (2009a) utilise TLS to measure fluvial gravel beds (D_{50} 32-63mm). Scan resolution was limited by the size of the laser footprint at 4mm, which is below the extent of aeolian ripples (Sharp, 1963) suggesting TLS would be a viable tool to study these bedform features. Ripples have been measured using TLS, Nield *et al*., (2011) detecting them alongside other small scale bedforms such as adhesion structures. As noted by Baas (2008) the application of TLS in aeolian environments allows non-interfering measurement of the surface conditions and shows promise for collecting data alongside other instrumentation such as sand traps, saltation probes and anemometers. Application of this set up may enable invaluable links between form and process, which have been largely treated separately within aeolian geomorphology.

TLS offers a number of advantages over other survey techniques. The process of data collection is automated to the extent where the user chooses an area to scan and the point spacing, but not the individual points within the study area. This removes the operator bias associated with the use of ranging poles and total stations (Heritage *et al*., 2009). The number of points collected is also superior to other manual surveying methods and as such offers a decrease in time taken to survey a given area (Wheaton *et al*., 2010). This improves the surface representation that is reproduced in a DEM (Pietro *et al*., 2008). TLS offers three dimensional surface data, an improvement over the shadow-cast technique previously used to capture ripple morphology (Niedzielski *et al.,* 2006). Stereo-photogrammetry can also capture three dimensional surface elevation data. However this method is reliant on indirect elevation measurement, which is influenced by the image quality or texture which is problematic on homogenous grain surfaces (Carbonneau *et al*., 2003).

The use of TLS to collect data during transport events is novel, as scans are typically undertaken before and after significant levels of transport have occurred (Hodge, 2009a). Using TLS during aeolian transport provides the opportunity to capture information about the saltating layer. Whilst the scan rate is too slow and laser footprint too large to capture individual grains, parameters such as saltation cloud height and intensity is be achievable using TLS (Nield and Wiggs, 2011). However undertaking scanning during transport events removes the ability to take convergent scans of the same surface. As TLS relies on line of sight, repeat scans are typically used to complete areas of point clouds that are occluded from the first scan. They can also be used to remove erroneous data points that occur during laser scanning, as they provide the ability to validate registered point clouds (Hodge *et al*., 2009a). However, repeat scans are time consuming, as multiple scan locations are required. This is not feasible when undertaking scanning during transport events, especially in an aeolian environment experiencing rapid change. Therefore an understanding of the errors experienced during laser scanning as well as best field protocols to minimise errors is essential (TLS errors are discussed in depth in Chapter 3).

Hodge *et al*., (2009) list four main sources of error when using TLS: scanner design, surface reflectivity, imaging geometry and post-processing. The scanner hardware design affects the precision to which the laser can be directed at the required angles, in terms of both the scanner rotation and the laser deflection with mirrors (Lichti *et al*., 2005). Electrical cross-talk and construction defects are also possible sources of error (Lichti, 2007). Surface reflectivity can affect the time of flight recorded for a point. A highly reflective surface will reflect a higher proportion of the laser pulse, which has the potential to saturate the detector before all the light is recorded. Therefore a shorter time-of-flight is produced, and the target distance is underestimated (Hodge *et al*., 2009a).

Imaging geometry involves a number of errors. Mixed pixels occur when the laser footprint falls on two or more surfaces of different distances from the scanner. The time of flight recorded is an average of the surfaces recorded, and is therefore a false surface representation. Mixed pixels are recognisable as point trails at the edge of discrete objects. Angular displacement errors occur when a laser pulse is returned from the edge of the laser footprint, but accredited to the centre of the point. This may cause objects to be enlarged within a point cloud. The laser footprint also influences the data resolution. The point recorded is averaged from the entire laser footprint, so whilst point spacing can be less than the stated footprint size, the resolution is determined by the footprint size as the smallest area surveyed (Lichti and Jamtsho, 2006). The placement of the scanner to the object of interest, the scanning geometry, can also have an impact on the quality of the point cloud produced (Soudarissanane, *et al*., 2011). Errors can also be introduced during post-processing. The most likely source is during the co-registration process. A number of filters exist to remove erroneous points, such as cone, repeat scan error and high point filters (Hodge *et al*., 2009a). However these rely on removing variation between multiple scans of the same surface which is not possible when only using single scans. Therefore the best method for the minimisation of errors is to develop protocols to reduce the number of errors collected in the field. Heritage and Hetherington (2007) offer a rudimentary protocol for laser scanning in fluvial environments, however aeolian specific protocols have yet to be developed.

2.11 Summary and Aims

Accurate estimation of aeolian sediment transport is important for many applications, yet current predictive models overestimate transport rates when compared to physical measurements. However it is unclear whether this discrepancy is cause by the models themselves or the methods used to gain measure transport rates. Current methods used to measure aeolian sediment transport tend to ignore the high spatial and temporal nature of aeolian sediment transport, and treat the saltating surface as uniform, despite observations to the contrary (Baas and Sherman, 2005). Recently, new developments in high resolution topographic surveying in the form of terrestrial laser scanning may provide the opportunity to accurately measure aeolian sediment transport using the morphologic method. This method has the potential to capture the migration of aeolian wind ripples and link their migration to an overall transport rate. TLS provides the ability to measure the surface remotely, thus providing minimal interference to the wind flow. TLS also provides the 3D surface representation which would be beneficial for studies linking saltation with bed development, surface roughness, and those concerning the development of self organising systems.

However, TLS is a relatively new technique and knowledge of errors sources is important to gain accurate data. The novel use of TLS during active saltation events introduces new challenges, as typical field methods (multiple convergent scans) can not be undertaken due to time restraints. Therefore typical methods used to reduce errors that rely on multiple scans of the surface, cannot be used. As such, information is needed regarding the sources and extent of errors when scanning from a single position. Due to the infancy of the technique, and application within aeolian environments, there is the opportunity to develop standardised protocols for using TLS to measure aeolian sediment transport. Therefore the aims of this thesis are:

- Explore and quantify the sources of errors in TLS when scanning from a single position, and whether these are different for bedforms of varying extents.

- Develop a set of best practice protocols that should be followed when conducting research utilising TLS in aeolian environments.

- Use these practices to reduce erroneous results when scanning ripple migration during active aeolian sediment transport.

- Use the morphologic method to estimate aeolian sediment transport, on a ripple scale, during a saltation event.

Chapter 3: Towards a Protocol for Laser Scanning for the Estimation of Aeolian Sediment Transport

As highlighted in the previous chapter, there is a need to collect high-resolution and accurate topographic data in aeolian environments and Terrestrial Laser Scanning (TLS) provides an opportunity to do this. The use of TLS shows promise for undertaking aeolian research (Baas, 2008) through its ability to capture high resolution topographic data however its use has been limited (e.g. Nagihara, 2004; Ochoa, 2005; Nield *et al.*, 2011). The use of TLS for geomorphic research remains poorly constrained in terms of standardised protocols and error assessment (Heritage and Hetherington, 2007; Hodge, 2009a). This is due in part to the relative infancy of the technique compared to other survey methods and the data quantity and quality produced. There remains a tendency to accept high resolution data as the most accurate surface representation, without full consideration of the means by which the data is collected, or the sources of error that can influence the recorded data (Lim *et al.*, 2009). Heritage and Hetherington (2007) propose a protocol for undertaking scanning in fluvial environments. They develop 11 protocols to optimize scanning in the field, however, these are largely based on qualitative observations from the field, without quantitative validation of optimal scanning positions. Errors in TLS are spatially variable, dependant upon variation in incident angle, survey range and laser footprint (Hodge *et al*., 2009a). This raises the issue of the methodological protocols that should be followed when utilising TLS in such environments (Heritage and Hetherington, 2007). The relative infancy of applying TLS in aeolian environments provides the opportunity of outlining standardised protocols to reduce errors in TLS data before its use becomes more widespread. This chapter therefore seeks to detail the field procedures that should be employed to ensure that potential problems with TLS data collection are minimised.

3.1 Sources of error in TLS

When utilising single scans therefore, an understanding of the source of error in individual points is vital to minimise error propogation through subsequent analysis

(Greun and Akca, 2005). Four main sources of error can be identified: (i) scanner hardware, (ii) atmospheric conditions, (iii) object properties and (iv) scanning geometry.

i. Scanner hardware refers to the scanner properties, calibration and settings. The precision of the TLS will determine the extent of random errors within any point cloud produced. This is influenced by the ability of the scanner to direct the laser beam in a specified direction, both through instrument rotation and mirror deflection of the laser beam (Zhuang and Roth, 1995). The effect of laser beam width (Lichti and Jamtsho, 2006), detection of returned laser pulse (Pesci and Teza, 2008) and geometric defects in construction (Lichti, 2007) have all been investigated.

ii. Atmospheric conditions can also influence point accuracy. Temperature, humidity, pressure, ambient lighting, and the effect of indoor and outdoor scanning have all been documented (Pfeifer *et al*., 2007; Voisin *et al*., 2007; Heritage and Hetherington, 2007; Borah and Voelz, 2007).

iii. Object properties concern the reflectivity and roughness of the surface material which has been shown to influence point precision (Kaasalainen, *et al*., 2009).

iv. Scaning geometry. The placement of the scanner relative to the surface of interest influences a number of variables shown to effect point accuracy. Incidence angle of the incoming laser beam, local range and local point density are all influenced by the scanning geometry employed (Mechelke *et al*., 2007; Soudarisanane *et al*., 2007).

Terrestrial laser scanning relies on line of sight and therefore portions of a scan area can be occluded by topographic or other features (such as vegetation, buildings or fences). Occlusion can be avoided through the undertaking of multiple, convergent scans from different scan positions. This practice has also shown promise in the identification and removal of erroneous data points. Hodge *et al*. (2009a) utilise a repeat scan error value, defined as the maximum 3D distance between repeat measurements of a point. A threshold error value is then applied to the point data, above which all points are removed. This has proved successful in the removal of mixed pixels. Mixed pixel errors are inherent within TLS point data, and are a function of imaging geometry. The time of flight recorded by the scanner is an average of reflections recorded from all surfaces within the laser footprint. When the laser footprint falls upon multiple surfaces of different ranges, the point will be recorded somewhere along the ray line from the scanner (Lichti *et al.*, 2005). Two further filters, a cone filter and a local high point filter are outline by Hodge *et al.*, (2009a) which both aim to identify areas containing large elevation ranges over small areas, indicative of re-entrant curves in the scan data. This issue is prevalent when complex 3D points are interpolated using standard 2.5D methods.

Although the undertaking of multiple scans has many practical advantages particularly in error identification, the time required to relocate to numerous scan positions can be prohibitively long. This is the situation encountered when seeking to quantify change in surface topography of rapidly evolving landforms, such as aeolian bedforms. Scanning during active aeolian transport presents a situation whereby the collection of topographic data from a single location would be beneficial as used by Nield *et al.*, (2011). Yet error identification using single scans is challenging. One possibility for error filtering during post processing is to apply a filter based on the angle of repose. Nield *et al.*, (2011) apply such a filter by analysing point pairs and removing points where the angle exceeds the angle of repose, defined as 35°. However the general lack of consideration of error filtering issues for applications involving single scans requires a more detailed examination of the scanning protocol used in the field to collect topographic data. Criteria regarding optimal scanning positions to reduce occlusion, time taken to undertake the scans and error minimisation would be beneficial. Similarly, quantification of the quality of scan data when optimal conditions are not attainable in the field would also be useful. As noted by Baas (2008) ideal conditions in which aeolian research can be undertaken are rarely encountered in the field.

Whilst the influence of scanning geometry has been recognised for TLS in previous studies (Kaasalainen, *et al.*, 2005), quantification of the effects of incidence angle has only recently been attempted (Lichti, 2007; Kukko *et al*., 2008; Soudarissanane, *et al*., 2009; Soudarissanane, *et al*., 2011; Schürch *et al*., 2011). Significant deterioration of point accuracy has been observed at incidence angles of 65° or above have been documented (Lichti, 2007; Soudarissanane, *et al*., 2011). Schürch *et al*., (2011) suggest incident angle has a negligible effect on the quality of a registered point cloud, however this is when compared to the errors produced during registration. Studies focussing on the effect of incident angle on scan quality have focussed on the horizontal planar effects of incidence angle (Lichti, 2007; Soudarissanane, *et al*., 2009; Soudarissanane, *et al*., 2011). Whilst this is important for architectural studies, TLS also has the ability to capture vertical geometry, and the vertical effects of incidence angle are likely to be more prevalent in geomorphic studies as many features of interest (such as small scale dunes and aeolian ripples) will be below the horizontal plane of the TLS. This effect has yet to be documented.

3.2 Incidence angle

The incidence angle, i, is defined as the angle between the laser beam and the surface of interest. Due to laser beam divergence, a beam hitting a perpendicular surface will result in a circular footprint (assuming a Gaussian beam emission) with normally distributed energy within that footprint (Figure 3.1). A non-zero incident angle results in an elongated laser footprint, which results in less light being returned to the scanner, and an increase in point spacing across the surface of interest. At great incident angles, signal detection becomes difficult and will ultimately result in the signal not being detected.

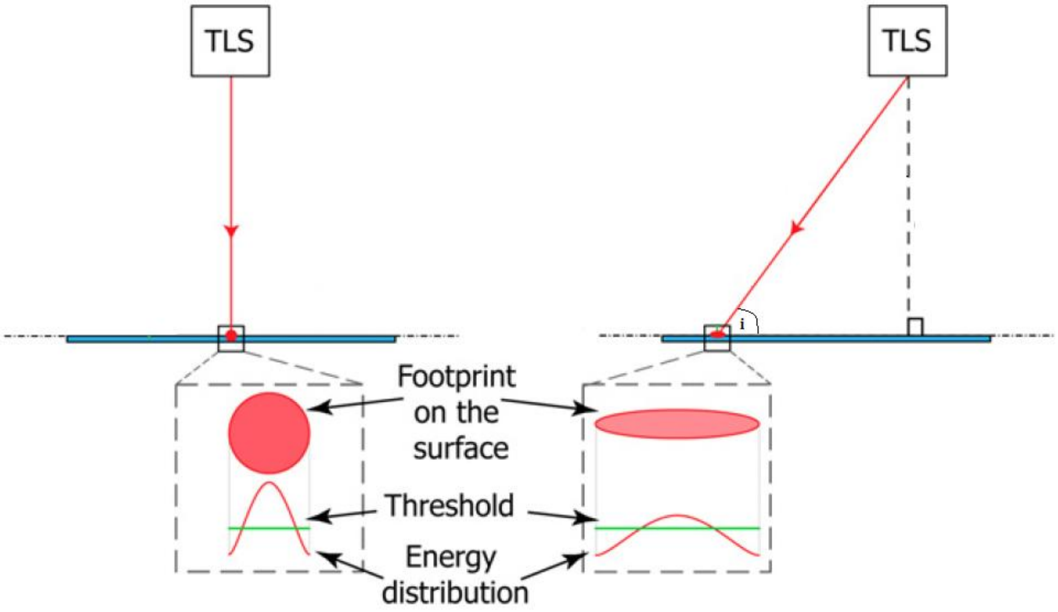

Figure 3.1: Schematic highlighting the influence of scanning geometry on the laser footprint and subsequent energy distribution at perpendicular (left) and non- zero (right) incidence angles where i is the incidence angle. Adapted from Soudarissanane *et al*., (2011,p3).

As previously discussed, the incident angle has been shown to influence point precision (Soudarissanane *et al*., *2011*). However previous control experiments investigating this have used highly reflective, smooth surfaces which are not truly representative of typical scanning environments. One of the main advantages of TLS is the ability to capture complex surfaces at high spatial resolutions (Hodge *et al*., 2009a), and the influence of incident angles on these surfaces is important to characterise.

3.3 Control Experiment

In order to look at the effects of incident angle on point cloud accuracy, a control experiment was devised. Two aeolian bedform features were investigated, ripples and small scale dunes (Figure 3.2).

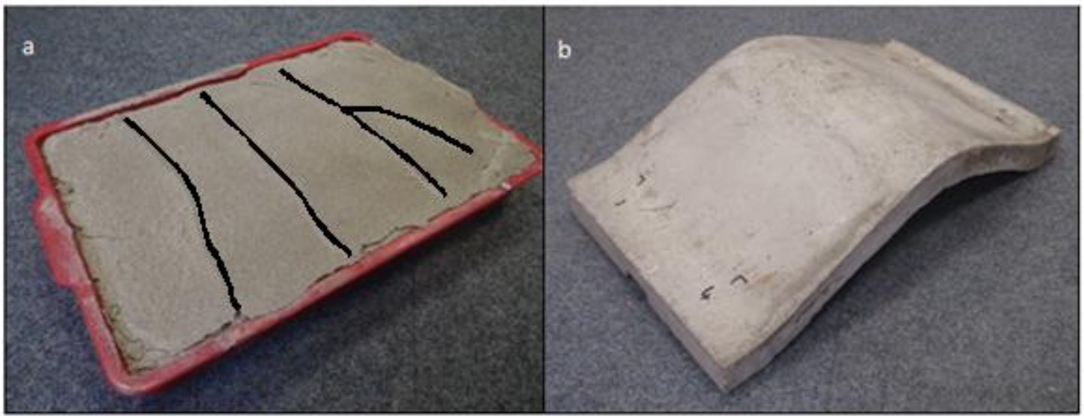

Figure 3.2: The two bedforms used in this experiment (a) ripples captured from the field (tray length 34cm) (b) artificial dune (length 65cm). Ripple crests are highlighted in black.

3.3.1 Control ripples

In order to produce a control topography representative of ripples for scanning, it was decided to collect a rippled surface from a natural setting. Sharp (1963) successfully collected ripples from the field in order to study their internal stratigraphy. This was achieved using a quick drying plastic (5-10% solution of Glyptol) which was applied to the ripples and allowed to permeate through to fix them in order for extraction. A similar approach was applied in this study, specifically a set of ripples were stabilised from the East Head Spit, on the Southern coast of the UK (site location: 50.47ºN 0.54ºW, Figure 3.3)). This collection took place on the 22/7/2010. The wind direction was consistently SSW (approximately 207º ± 5º (standard deviation) as measured at a site approximately 2.7 km SW from the East Head dunes (Anemometer location: 50.46 ºN 0.54 ºW). The wind speed, measured at a height of 5m, ranged from 4.7 ms^{-1} to 8.3 ms^{-1} with a mean speed of 6.6 ms^{-1} (Figure 3.4). The day was dry and sunny.

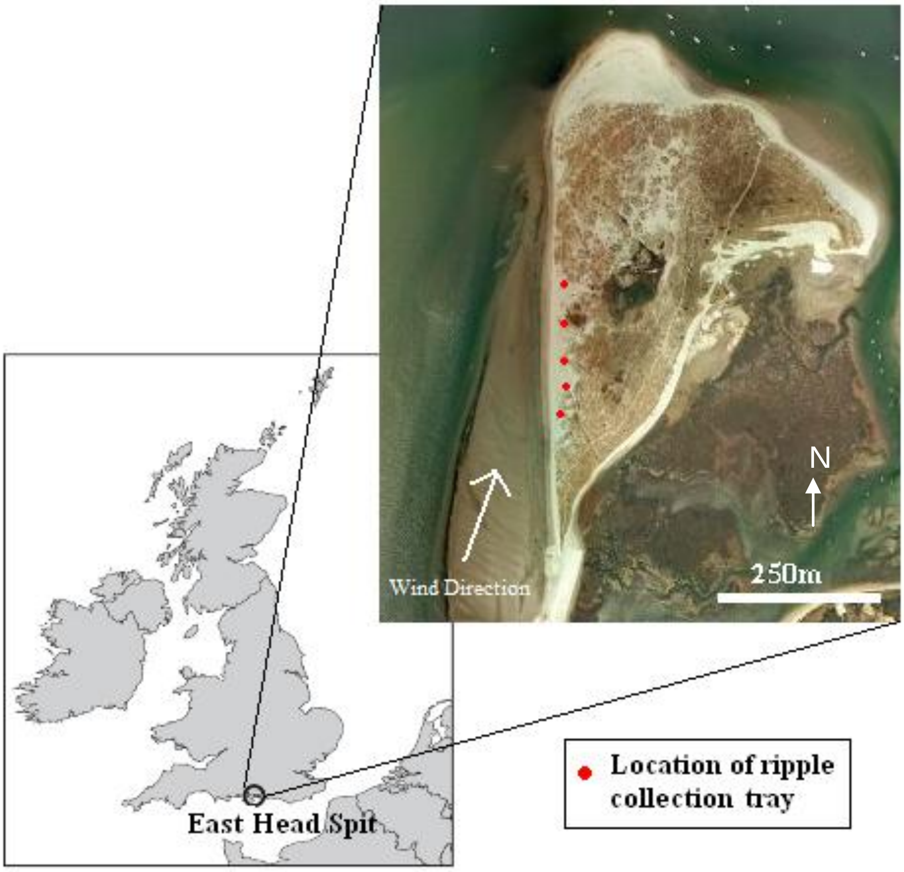

Figure 3.3: Map showing the locations of the East Head Spit. Locations of the ripple collection trays are shown top right, the second most southerly tray was utilised in the subsequent scanning experiment. Image source: Google Earth

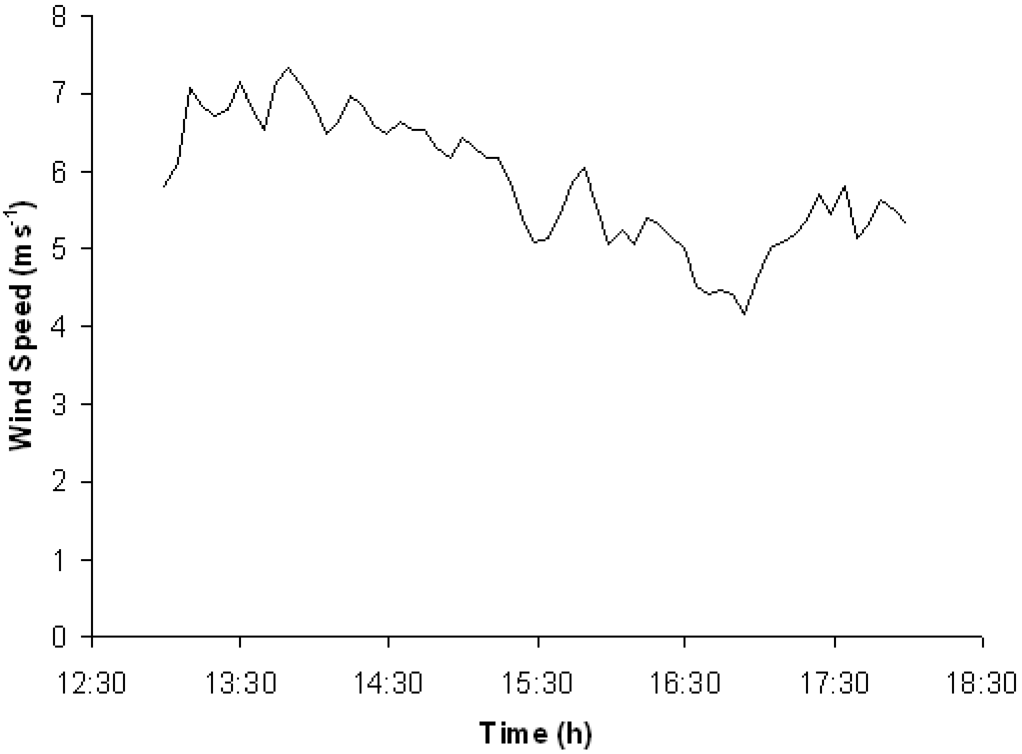

Figure 3.4: Wind speed, measured at a height of 5m, during the ripple collection period from the nearby weather station, recorded at 1 second intervals and averaged over 5 minutes.

Five shallow plastic trays, 34cm in length, 24cm in width and 2cm deep, were installed at different locations separated by 5 metres along the base of the foredune. The trays were orientated so the length was facing the same direction as the wind, and the tray was buried flush with the surface of the sand. Active transport was only intermittent as the wind strength varied. Therefore sand was mobilised upwind by manually disturbing the sand surface by hand, thus lowering the transport threshold needed for entrainment. This resulted in sediment being delivered over the trays and allowing ripples to form naturally. Once a rippled pattern had formed on the tray, a barrier was placed upwind of the ripple to prevent active transport during the fixing process. The ripples were fixed using a clear lacquer, more commonly used for automotive paint finishes. The lacquer was delivered by an aerosol spray which allowed even distribution. The aerosol was held approximately 30cm above the surface to prevent disturbance. Five coats of lacquer were applied and allowed to dry for 2 hours before the trays were carefully removed and transported back to the lab. The lacquer was then left to harden for five days. Of the five samples collected, the tray with the most developed ripples was used for analysis. Three full ripples were captured, with wavelengths of approximately 10cm, and amplitudes of approximately 0.5cm. The central ripple included a defect and showed lateral linking between crest terminations (Figure 3.2a).

3.3.2 Artificial Dune

A control dune was used to assess at the effect of scanning larger bedforms, because the capture of a physical dune from the field was not possible. The concrete dune measured 65cm in length, 35cm in width, with an amplitude of 10cm running lengthways. The dune was symmetrical in shape with a maximum slope angle of 25°. The dimensions of the artificial dune are consistent with observations of protodunes made by Kocurek *et al* (1992), with symmetrical protodunes 10cm in height observed forming from sand patches. These dimensions were also manageable in terms of manipulation within a control environment. In the control experiment, three dunes were placed alongside each other to replicate a natural dune field. The wavelength of the dunes was 65cm.

3.4 Experimental Procedure

The control experiment was undertaken over a two day period from the 14th-15th December 2010. The Experiments took place outside on a dry, calm sunny day. The terrestrial laser scanner used in this control experiment was a Leica Scanstation, a time of flight, pulse based scanner. This equipment utilises a ndYAG 532 nm laser and can collect up to 4000 points s^{-1} over distances of up to 300m. The minimum point spread function is 4mm over ranges of up to 50m. The precision of the Scanstation as stated by the manufacturer (as one standard deviation) is 4mm for distance, 6mm for position and 60 μrad for angles (Leica Geosystems, 2007), and these determine the extent of random errors within the scan data (Hodge *et al.*, 2009a). Additional experiments into the accuracy of the ScanStation have shown the precision of TLS data over short distances to be approximately 2mm (Hodge *et al.*, *2009a*, Reshetyuk, 2010). The minimum point spacing was 1.4mm at a the distance from the centre of the bedform; therefore the resolution was limited by the size of the 4mm size of the laser footprint at 50m. The scanner has a 360° horizontal and 270° vertical field-of-view (FOV). The vertical FOV limits the maximum incident angle achievable by the scanner to 45° below horizontal, as the dual axis compensator maintains a level scanning position. The incident angles investigated therefore ranged from 0-45° (Table 3.1). These values were also governed by the swath range of the laser over the bedform, and it was ensured that none of the ranges overlapped. The incident angles of the incoming laser beam were altered by changing the distance of the TLS relative to the bedform. Instrument height is recorded at a mark on the scanner. The scanner was set up at a height of 2.5m on a flat area, 30m in length which was large enough to scan at the distances required by the experiment. The incident angle was calculated trigonomically, and the distance from the scanner to the centre of the bedform was measured using a tape.

Table 3.1: Incident angles, range in the angle and the distance of the scanner to the bedform.

Incident Angle (°)	Range +/- (°)	Distance from bedform (m)
43	1.55	2.6
40	1.5	2.9
37	1.47	3.3
34	1.43	3.7
31	1.4	4.1
28	1	4.7
25	0.94	5.3
20	0.63	6.8
15	0.3	9.3
10	0.17	14.1
5	0.04	28.5

The bedform features were placed with the crests parallel to the scan direction (Figure 3.5). Placing the TLS parallel rather than perpendicular to the crest is desirable so that scanning during active saltation will have less interference with the local wind conditions. This also maintains a low incident angle range over the bedform compared to scanning from a transverse position. Four targets were placed around the scan area in order to register the scans to a common coordinate system. The workflow for scan acquisition is shown below (Figure 3.6). Scans were undertaken at the minimum point spacing, 1.4mm. Further scans were also carried out to produce a validation data set (Section 3.4.1).

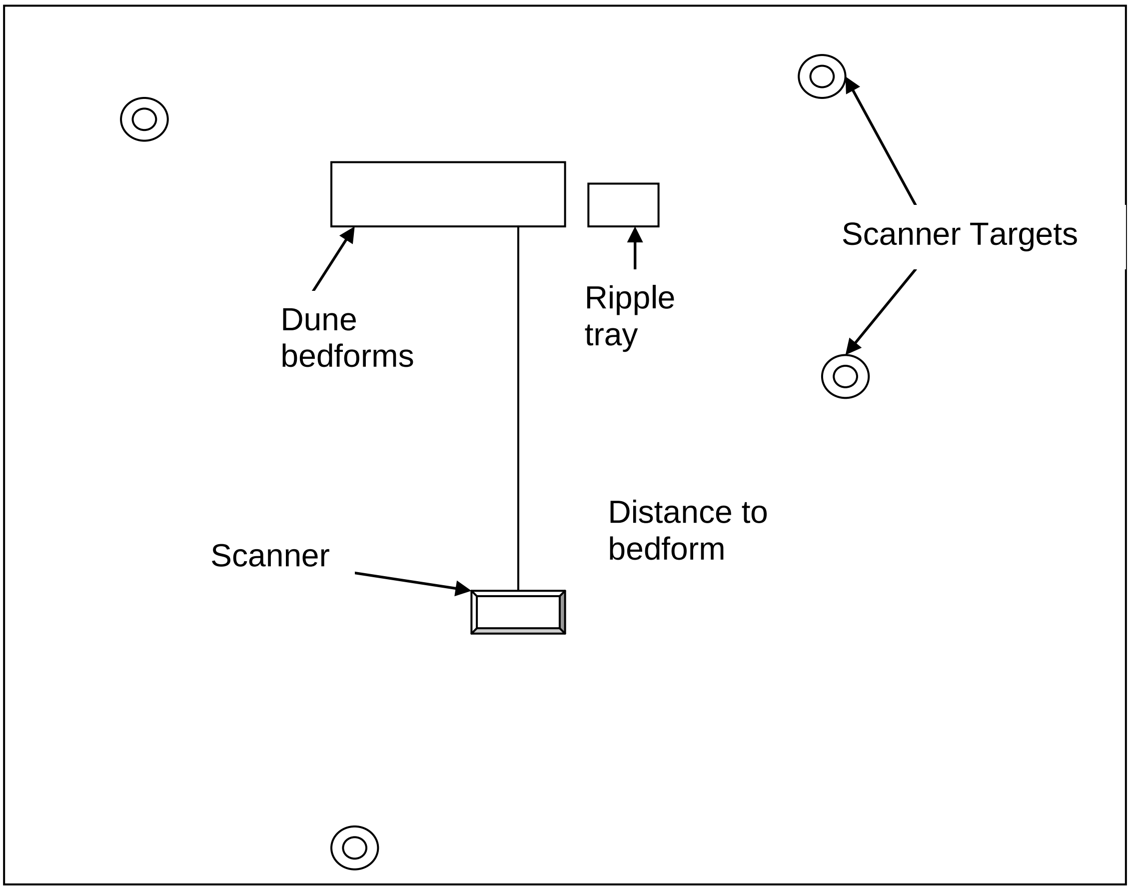

Figure 3.5: Overview of control experiment set up.

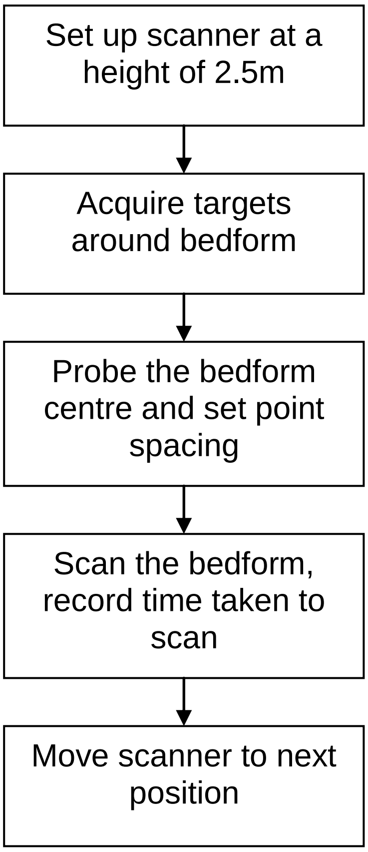

Figure 3.6: Workflow for scanning experiment.

3.4.1 Validation Data Set

A problem that arises when using TLS data is a lack of independent surface elevation data to check the accuracy of the digital terrain model produced by the scanning (Hodge, 2009a). However, there are a few methods available that match the quality and resolution produced by TLS points. Total stations have been used (Heritage and Hetherington, 2007, Hodge *et al.*, 2009a, Lim *et al.*, 2010), however, these are subjective as the operator chooses the points to sample (opposed to TLS) and are only useful in checking TLS points in the immediate area of the total station recording.

This experiment utilises TLS data to validate the single scanned data. As discussed above, multiple scans from different scan positions provide the ability to filter the point cloud to remove errors and provide more accurate digital terrain models.

Where overlap occurs from the multiple scans, point density is increased providing a further advantage over single scans. Therefore point clouds of the two bedforms used from multiple scan locations were used to validate the single scan data, in an effort to provide quasi independent surface data.

The scanner was set up at four positions surrounding the bedform at approximately 90° intervals. The scan head height was set on a tripod at 2.5m, with a distance of 3m to the bedform which provides a high incident angle. A scan was conducted at each scan position with a point spacing of 1.4mm at the bedform centre. Registration of the scans was performed using the four fixed targets as shown above (Figure 3.5).

3.5 Post Processing

Point cloud processing was then undertaken in order to prepare the scan data for analysis. This was undertaken in Leica's propriety software, Cyclone 5.8. Firstly, both the control experiment scans and the validation scans were registered to a single common coordinate system. The clouds were registered by a bundle adjustment programme within Cyclone (Leica Geosystems, 2007), transforming each point cloud so that the errors between survey targets are minimised. In the scans collected, the mean registration error of the targets was 1mm. The point cloud was then manually cleaned to remove the areas surrounding the bedforms captured during the scanning process. This resulted in a point cloud containing the bare surface of the scanned bedform. Individual scans were exported for further analysis, as were the four scans making up the validation data set.

3.6 Point Densities

Point density has been shown to be a useful metric for the comparison of scan data (Behan, 2000; Lindenbergh et al., 2005; Hodge et al., 2009a). In order to analyse the influence of the four variables used, the point densities of the scans were used as a metric for comparison. Point density will influence the accuracy of the subsequent digital terrain model produced from the scan data. As noted by Olsen and Stuedlein (2010) the strength of TLS lies in its ability to produce dense point clouds, rather than in the individual points collected. To calculate the point density, firstly the surface area was calculated using the topographic surface area function within Cyclone. The number of points per scan was then divided by the surface area to produce number of points per cm^2. The results for both the dune (Figure 3.7) and ripple (Figure 3.8) are shown below.

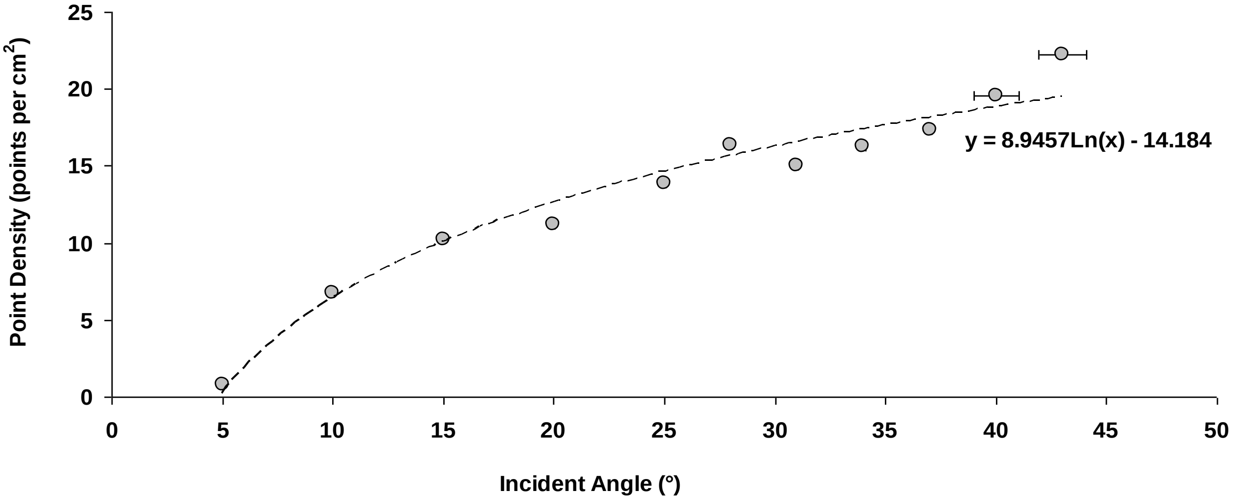

Figure 3.7: The relationship between incident angle and point density for the dune surface. R^2= 0.92. X Error bars show the range in incident angle, however these are minimal (within the point) for all except 40° and 43°

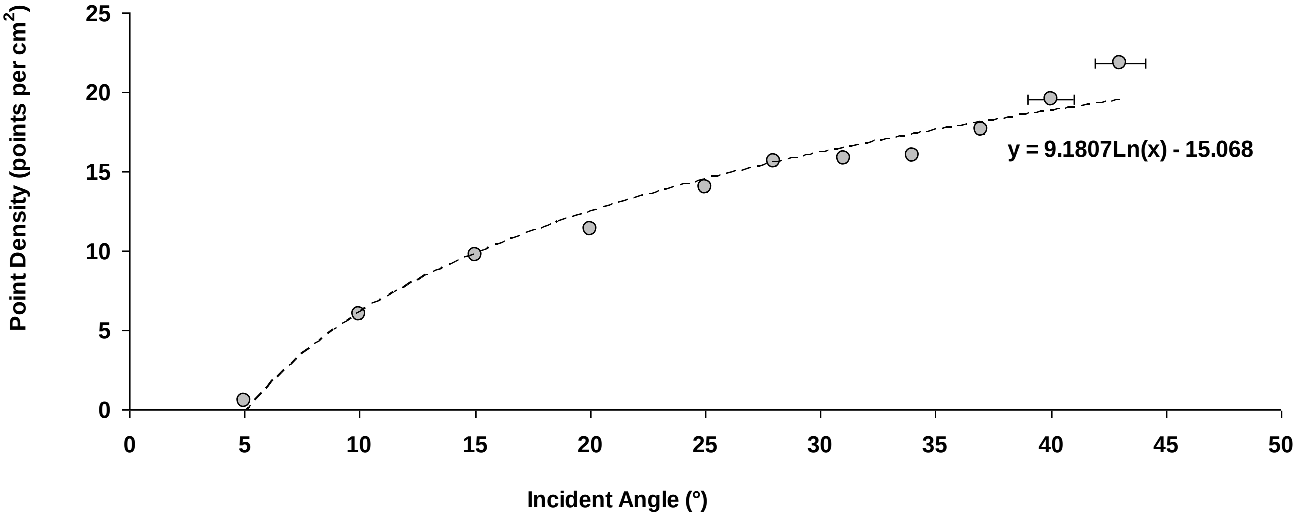

Figure 3.8: The relationship between incident angle and point density for the rippled surface. R^2= 0.91. X Error bars show the range in incident angle, however these are minimal (within the point) for all except 40° and 43°

The results show a strong correlation between incident angle and point density. The results for the dune and ripples are comparable, with both bedforms showing very similar point densities despite differences in bedform size. Both bedforms show increases from less than 1 point per cm^2 at an incidence angle of 5° to over 21 points per cm^2 at incidence angles of 43°, representing a significant increase. It is important to note at this stage that each scan collected was set a point spacing of 1.4mm, which is not achieved at the lower incidence angles. This is not surprising as the specified point spacing applies to a perpendicular scan angle which is not the case in this study. Whilst point density provides a useful metric for initial comparison, it does not provide information regarding the accuracy of the point cloud in representing the surface of interest. Mixed pixels and angular displacement errors could contribute to a higher point density. Therefore, more pertinent metrics related to the bedform of interest may be more useful when studying the applicability of TLS in aeolian environments. These are discussed in the following section.

3.7 Bedform Metrics

The influence of scanning geometry on the measured value of bedform metrics are more suitable in determining the applicability of TLS in aeolian environments. TLS has been used to extract ripple wavelengths and amplitudes (Nield *et al.*, 2011) and these metrics have the potential to determine the influence of TLS scanning geometry on the measured value of key bedform features.

To explore this further, the following methodology was used. Firstly the scan data was reorientated in cyclone so the bed was horizontal and the ripple crest lines are parallel to the y axis. This point cloud was then exported and gridded onto an arbitrary grid within Matlab by taking the mean elevation of the points within the grid cell. The effect of cell size was explored by altering the cell dimensions. For the ripple bedform, resolutions of 0.002m, 0.005m and 0.01m were utilised. These values were selected as they are smaller than the feature being studied. It has been documented that when using cell resolutions greater than the feature being studied, the ability to accurately represent the surface is lost (Woolard and Colby, 2002; Hodge *et al*, 2009a). For the dune, the resolutions chosen were 0.002m, 0.01m and 0.1m. To extract bedform wavelength and amplitude five separate cross sections of the scan data were taken for each incidence angle. The cross sections were then analysed by automatically selecting local maxima and minima within the cross section. A schematic of this process is shown in Figure 3.9. An average of the bedforms amplitudes and wavelengths was then taken to reduce the effect of erroneous scan data points.

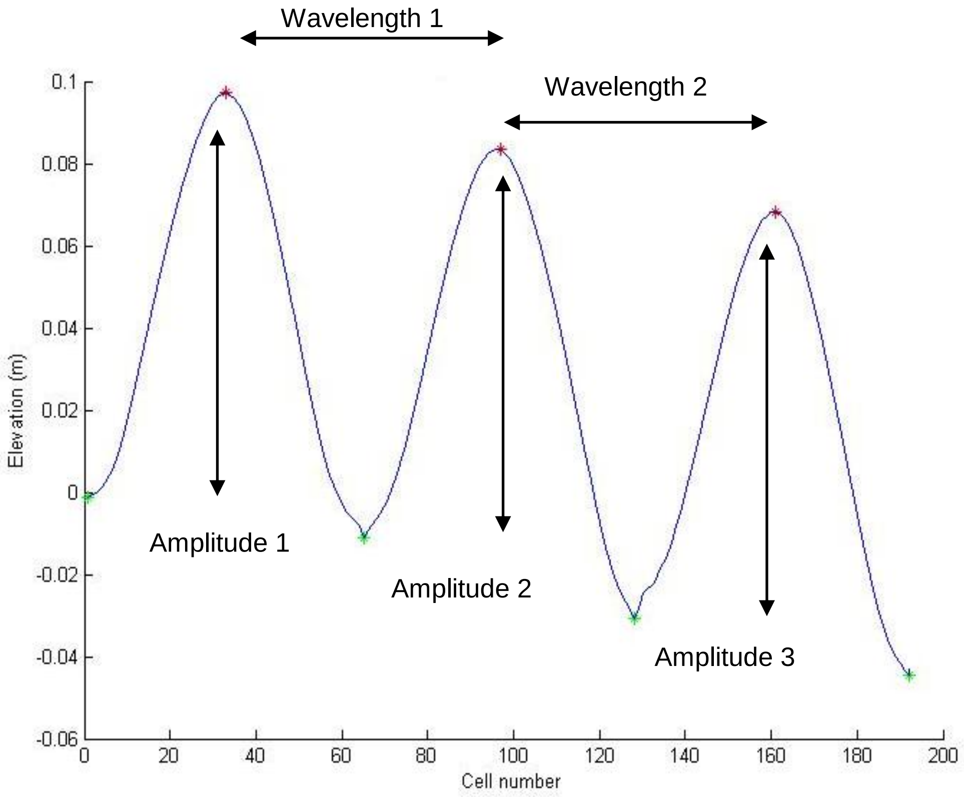

Figure 3.9: Cross section from a dune scan and the method used to extract the bedform wavelength and amplitude. The red points represent the highest points within the data set and green points the lowest.

The amplitudes were calculated by subtracting the lowest point on the left hand side, from the highest point in each corresponding peak to the right. The wavelengths were calculated as the distance between subsequent highest peaks, subtracting the first highest peak from the second highest peak. The validation scan data was also subjected to this analysis in order to produce an “actual” amplitude and wavelength, to which the single scan data was compared. The validation data set was gridded at the smallest cell size depending on the bedform analysed (0.002m for the ripple and 0.01m for the dune). The ripple grid size is the smallest possible grid size before the cell became less than the scanner resolution. The Dune grid size was chosen as anything smaller would result in data redundancy (Heritage and Large, 2009). This process was automated within Matlab. The values calculated for the wavelengths and amplitudes were subtracted from the corresponding validation data set to provide a means of comparison. The results of this analysis are shown below for the dune bedforms (Figures 3.10 and 3.11) and ripple bedforms (3.12 and 3.13).

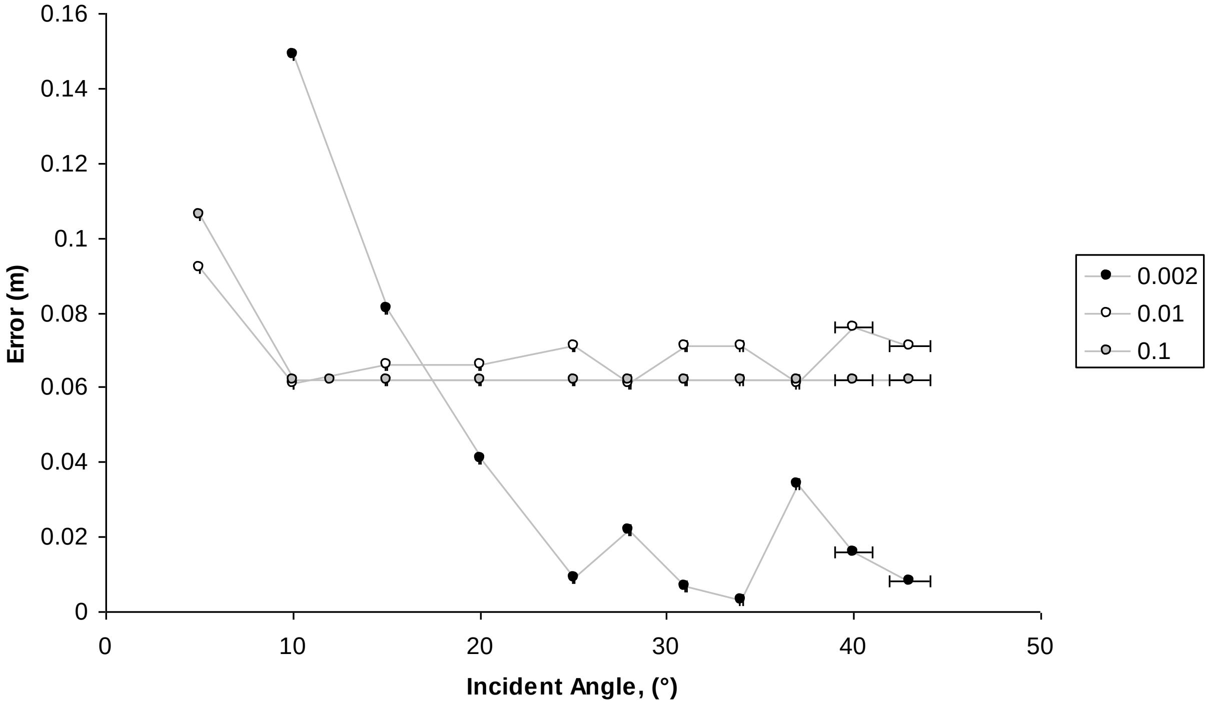

Figure 3.10: The mean error between the extracted dune wavelengths and the mean actual wavelength. . Legend shows the grid resolution. Error bars show the range of incident angle experienced over the bedform, and are included within the point for the majority of data points.

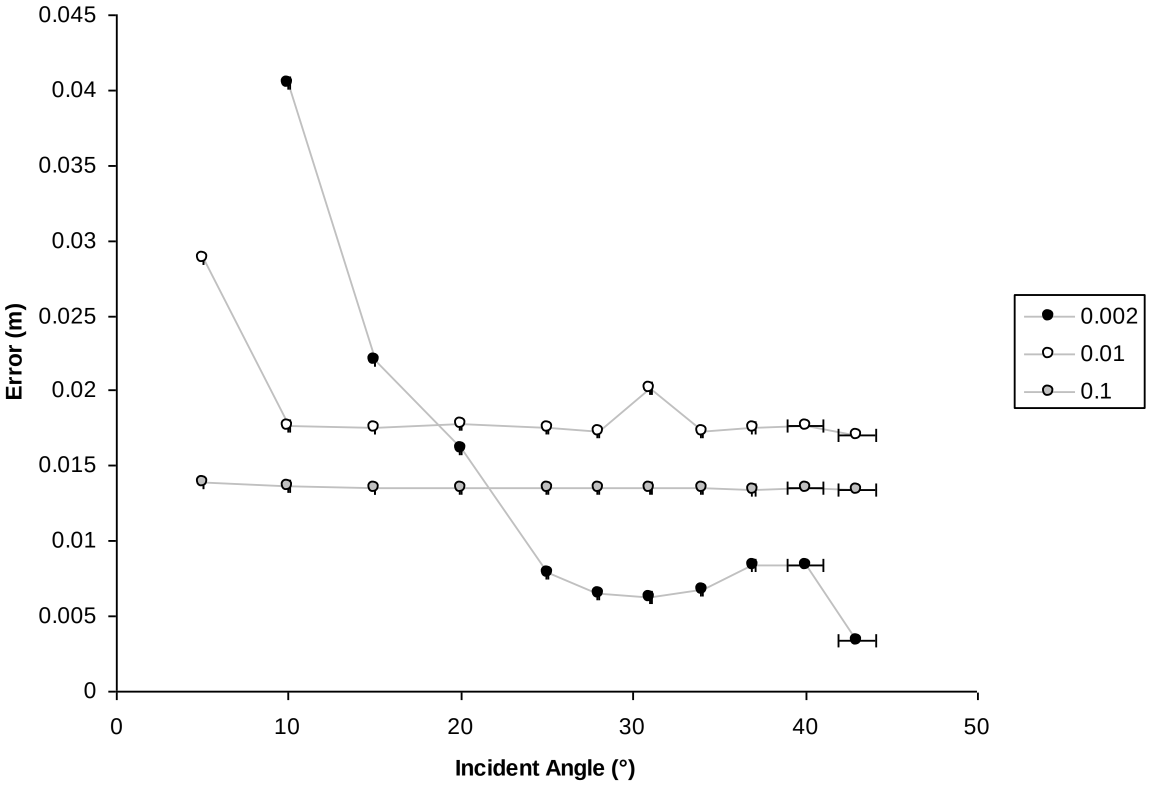

Figure 3.11: The mean error between the extracted dune amplitudes and the actual amplitude. . Legend shows the grid resolution. Error bars show the range of incident angle experienced over the bedform, and are included within the point for the majority of data points.

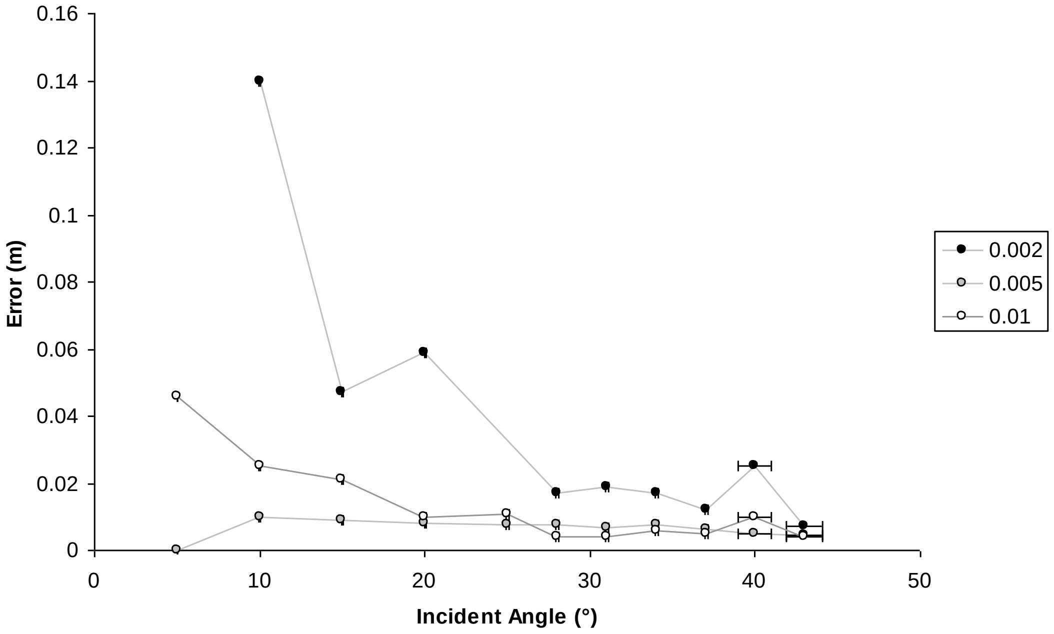

Figure 3.12: The mean error between the two extracted ripple wavelengths and the actual wavelength. . Legend shows the grid resolution. Error bars show the range of incident angle experienced over the bedform, and are included within the point for the majority of data points.

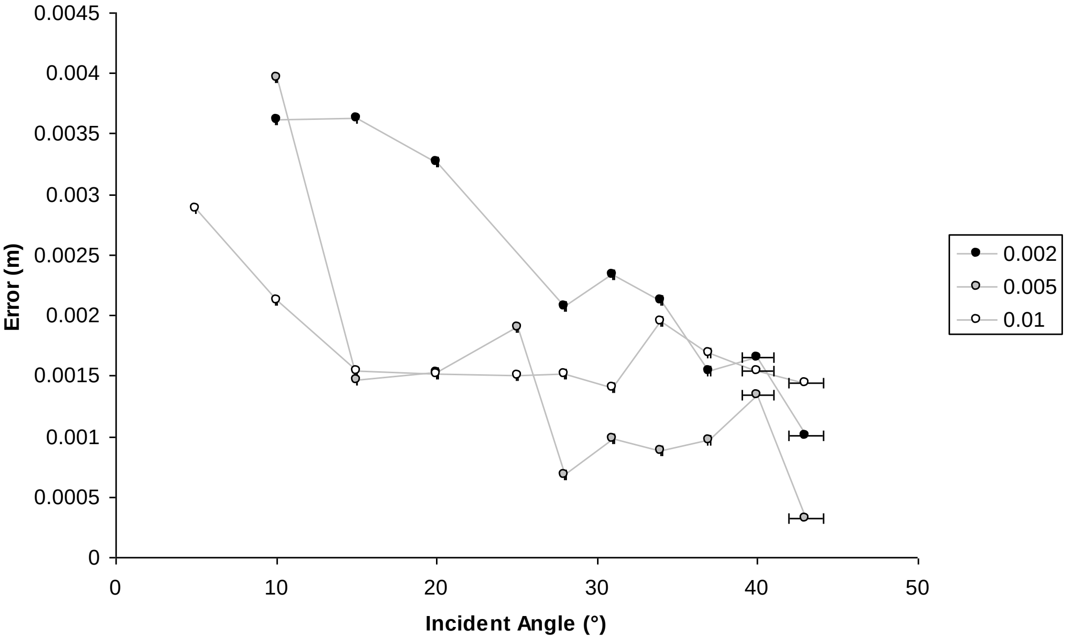

Figure 3.13: The average error between the three extracted ripple amplitudes and the actual amplitude. Legend shows the grid resolution. Error bars show the range of incident angle experienced over the bedform, and are included within the point for the majority of data points.

The results suggest incident angle influences the ability of the scanner to extract key landscape metrics. The extraction of dune wavelength (Figure 3.10) shows a decrease in error with increasing incident angles up to a point before converging for larger angles. The incident angle at which this convergence occurs changes with the cell resolution used to grid the data. At the finest resolution, 0.002m the error reduces from 0.15m at incident angles of 10°, to 0.01m at 25° before experiencing some levelling in the margin of error. The error at lower resolutions appears to decrease greatly from incident angles of 5-10° before stabilising at 10° with a typical error of 0.06m, this convergence occurs at lower incident angles than the higher resolution data.

A similar pattern is observed with the dune amplitude values (Figure 3.11). The greater resolution provides the lowest error in dune amplitude at incidence angles of 25° and above. Below this angle, the errors are somewhat larger, with the greatest error being 0.04m at 10°. Interestingly, the data gridded at a 0.01m resolution has a higher level of error, levelling out at around 0.019m, than the data at 0.1m resolution which has a stable error of around 0.015m. One potential explanation for this occurrence is that the concrete dunes used had amplitudes of 0.1m, the same size as the grid resolution.

The results are similar for the rippled bedforms. The ripple wavelength (Figure 3.12) shows at 0.002m resolution the same rapid decrease in error at incident angles of 5-25° from 0.14m to around 0.02m. However the wavelength appears to be best represented at resolutions of 0.005m, with resolutions of 0.01 also generally lower than at the 0.002m resolution. One possible explanation for this observation is that at resolutions of 0.002m, either no data points fall into a large number of cells, or very few data points are used when the cell average elevation is being calculated, thus increasing the influence an erroneous data point has on the overall cell elevation. At larger cell resolutions, the effects of these are lessened by the volume of more accurate data points. This is supported by the above point density data, which shows that despite setting a scanner point spacing of 1.4mm, in reality this is not achieved at low-medium incident angles. Behan (2000) supports this explanation by suggesting that the most accurate surfaces are created when using a grid spacing similar to the original data point spacing.

Errors in ripple amplitude display a similar behaviour to the wavelength data. Again using a resolution of 0.005m appears to offer the most accurate representation of the bedform, with sub millimetre errors at the highest incidence angle. At all resolutions, the data is more accurate at incidence angles of 25° and above. Whilst even the largest errors appear to be relatively small (around 0.0035m), it should be noted that in relation to the extent of the features being studied (average ripple amplitude of 0.005m), errors of this magnitude are significant.

3.8 Digital Elevation Model Accuracy

Typically within geomorphological studies, elevation point data is used to produce digital elevation models (DEMs) which are then used for a variety of different purposes, such as morphological change monitoring (Brasington *et al.*, 2003; Milan *et al.* 2007, Lim *et al.*, 2010), and landscape metric extraction

(Hodge *et al.*, 2009b). DEM errors will propagate through any subsequent analysis, therefore, it is important to minimise errors within DEMs. Attempts to quantify and minimise error in laser scanned data of complex surfaces has been attempted by Hodge (2010), however, this relies on the ability to scan a surface from multiple angles. As discussed above, this is not always possible. The survey strategy can play an important role in the accuracy of topographic points collected, as noted by Heritage *et al.*, (2009a), however, this study utilised TLS as a validation data set to quantify error when using theodolites and airborne LiDAR. As highlighted above, scanning geometry can influence point cloud data, however, the effects of incident angle on the quality of DEMs has yet to be explored within the literature. The following describes the methodology used to asses this problem in order to develop a protocol for TLS use in the field. DEMs of the scans measured from different incident angles were produced using the raw point clouds extracted earlier. These points were gridded onto an arbitrary grid within matlab, taking a mean of the points to give surface elevation. Cell resolution was set at 2mm. The validation data set was also produced using the same method. Each DEM was then subtracted from the validation data set in order to provide a cell by cell estimate of the error within the DEMs produced from a single scan. Mean absolute error was calculated in order to highlight the relationship between incident angle and DEM accuracy for the dune and ripple bedforms (Figure 3.14).

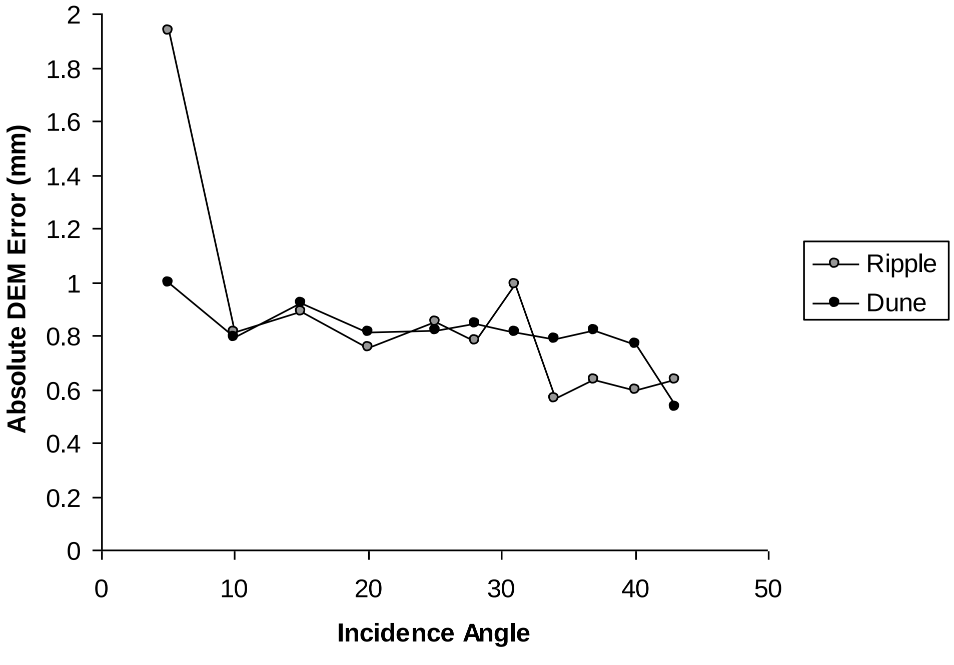

Figure 3.14: Graph Showing the relationship between incidence angle and absolute DEM error for the ripple (R^2 0.4933) and dune (R^2 0.5238) bedforms.

The above figure shows that incidence angle does have an effect on the DEM accuracy when analysing both ripples and dunes. Incidence angle has a larger effect on error on the rippled surface, with an error range of 1.9-0.5mm compared to1.0-0.05mm for the dune surface. The largest error (1.9mm) occurs when scanning the rippled bedform at the lowest incidence angle (5°). This result is unsurprising considering the complexity of the rippled surface and the low point density experienced at low angles. However, the difference between the dune and ripple errors at the lowest incident angle is interesting. One potential source of this disparity is the different surface textures and reflectivity. The dune was pale and smooth concrete, whilst the rippled surface was much rougher. The influence of surface roughness and colour has been previously documented, and scans of smooth, white surfaces are more accurate than those of other colours and textures (Clarke and Robson, 2004). The effect of surface roughness and colour require further investigation in the context of scanning aeolian features.

Whilst the absolute values provide a means to compare the effect of incidence angle on DEM accuracy, no information regarding systematic over or under prediction within the DEM is given. This is displayed in the histograms below for the dune (Figure 3.15) and ripple (Figure 3.16). Error is positive when a cell shows greater elevation than the validation data set and negative when the elevation is below the validation data set.

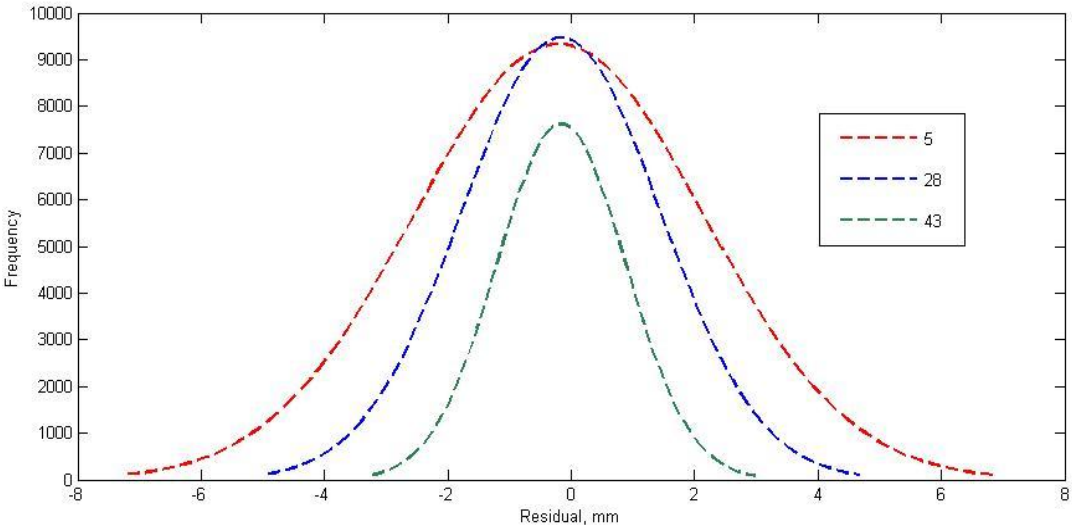

Figure 3.15: Distribution of residuals from the DEM differencing analysis at different incidence angles for the dune bedform.

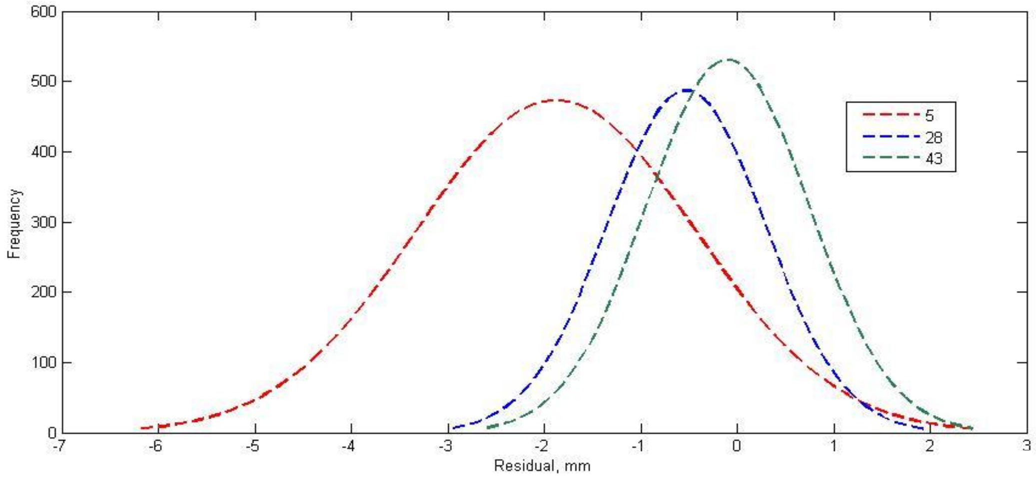

Figure 3.16: Distribution of residuals from the DEM differencing analysis at different incidence angles for the ripple bedform.

The residuals for the dune DEM (Figure 3.15) are Gaussian in distribution with a mean of 0mm. Errors have a wider range with increasing incident angle. For the rippled surface (Figure 3.16), incidence angle again appears to have a greater impact, with under prediction increasing at lower incidence angles. A clear shift is seen for the rippled bedform from mean under prediction of 0mm at 43° to 2.1mm at 5°. This error is significant when the extent of the rippled bedform is considered. This trend is not observed in the dune data, suggesting the morphology of the feature being scanned is responsible for the increase in surface underestimation. One possible explanation for the shift is the relative complexity of the surface being studied when compared to the dune. Three ripple features are present on the rippled bedform, providing greater potential for occlusion from the scanner line of sight. The rippled surface also covered a smaller area than the dune, therefore the lower point density experienced at low incident angles will have a greater influence.

3.9 Scan completion time

One important factor in scanning rapidly changing landforms is the time taken to acquire accurate topographic data. As the above results suggest, there will be a trade-off between scan time and the ability to capture accurate data. Figure 3.17

shows the time taken to complete each scan of both bedforms at increasing incident angles. For the dune bedform, scan time doubles from 3:41- 7:33 over incident angles of 5-15°. After this the time taken increases from 7:33 to just 9:47 over incident angles of 15-43°. Scan times for the rippled bedforms displays a similar trend, with a sharp increase in scan time at incidence angles ranging from 5-15°, before smaller increases in scan times are observed. This suggests that if rapid data acquisition is required, the error associated with scanning at low incident angles may have to be accepted in order to collect data as quickly as possible.

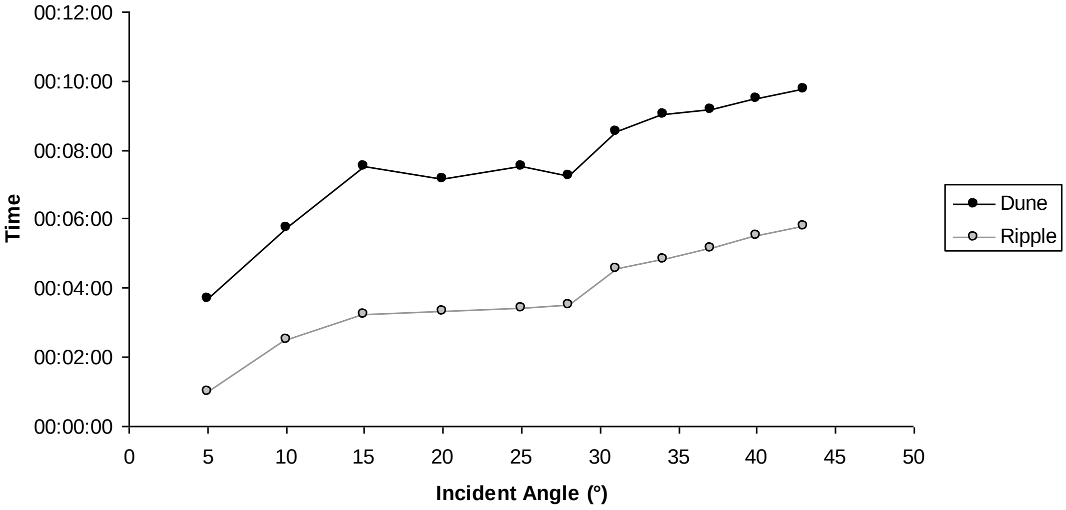

Figure 3.17: Time taken to complete the scanning of both bedforms at increasing incident angles.

3.10 Discussion

This study has focussed on the influence of scanning geometry, specifically the laser beam incidence angle, on the accuracy of the point cloud produced. This has been undertaken with a view to developing a protocol for utilising TLS in an aeolian environment. Point density is shown to be significantly influenced by the incident angle, with point densities varying by 20 points per cm^2 despite maintaining a fixed point spacing within the scanner set up. These results are comparable with Lindenbergh *et al*., (2005), however, this aspect appears to be largely ignored when considering scan set up in previous TLS studies (Keightly and Bawden, 2010). Whilst a high point density is desirable (Olsen and Stuedlein 2010), it says little about the accuracy of the points. The results have shown that the ability of the scanner to extract key landform metrics is also influenced by incidence angle. The dune scans experience the lowest errors when gridding the data at high resolutions and at incidence angles of 25° and above. The rippled data follows a similar pattern suggesting that a field set up with the highest incidence angle is desirable in order to produce the most accurate data. Data accuracy is likely to be a function not just of point density, but also fewer erroneous data points. As shown in Figure 3.1 the laser footprint is elongated at low incidence angles, increasing the likelihood of the footprint falling over multiple surfaces of different distances (such as a bedform crest) resulting in a mixed pixel being produced (Hodge *et al*., 2009a). Identification of these erroneous data points in single scan data remains an area for further study; however, it is highly difficult during active aeolian transport as saltating grains are likely to create mixed pixels (Nield and Wiggs, 2011).

Error propagation as a result of scan incidence angle has been observed in the DEM produced. The magnitude of the error is shown to reduce with increasing incidence angle, to the point where errors are sub-millimetre. This represents a promising justification in the use of single scanned data. One problem however remains the issue of occlusion due to the line of sight nature of the TLS. However, as discussed previously, setting up the scanner longitudinally to the direction of the bedform crest not only minimises the influence of the scanner on the local wind field, but is also likely to reduce occlusion compared to a transverse scan direction, particularly if a narrow scan swath is used. Increasing incidence angle is shown to decrease the range of errors within DEM (Figures 3.15 & 3.16). For the dune the mean error remains around 0 regardless of the incidence angle. However, the rippled surface appears to be more affected by the incidence angle, with surface under prediction occurring with decreasing incidence angle. This is a useful result, particularly if TLS is being used to capture micro-topography such as a rippled surface.

3.11 Conclusion

With the quantification of the errors associated with TLS in an aeolian environment, steps can be taken in order to undertake fieldwork with more confidence in the results of single scanned data. If ideal incident angles cannot be achieved, then an awareness of the magnitude of errors is important in order to assess the usefulness of the data acquired. The results have shown that scanning geometry has a significant influence on point cloud quality. It is therefore worthwhile considering when planning field campaigns using TLS in aeolian environments. The bedform of interest is important, as differences between ripples and dunes have been observed. For example, DEM accuracy of rippled surfaces is low at low incident angles, however, this effect does not appear to be as severe in dune environments, suggesting a lower influence angle (and therefore larger scan range) can be used if the primary target of the TLS study is small scale dunes. In the results displayed here, point cloud accuracy increases with incidence angle. Therefore field set ups should attempt to create the maximum incidence angles possible. This may be achievable through careful site selection, setting up the TLS on higher topography than the feature of interest or elevating the TLS position. Studying aeolian features on an inclined surface (such as ripples on the lee side of a dune) is also a possible method of increasing scan incidence angle. Incidence angles can quickly be calculated in the field, therefore fieldwork utilising TLS would benefit from preliminary scans to calculate the range of incidence angles encountered from the single scan position. Scanning geometry is an influencing factor that is useful not only in aeolian settings but any environment where TLS will be employed. Standardised protocols for laser scanning are important. The above methodologies could be applied in order to quantify errors associated with scan geometry in different environments.

Chapter 4: Application of Terrestrial Laser Scanning to In-situ Aeolian Bedforms

The previous chapter has highlighted the ability of TLS to accurately capture aeolian bedform features in a controlled experiment. The influence of scanning geometry has shown that consideration of the scan set up is important when planning a field study. More accurate methods to measure aeolian sediment transport are required (Li and Ni, 2003; Namikas, 2003; Ellis *et al*., 2009a; Barchyn and Hugenholtz, 2010), and TLS offers the ability to move away from point-based measuring methods and give an overall view of bed changes during active transport (Nield *et al.*,2011; Nield and Wiggs, 2011). The morphologic method has proved useful in fluvial geomorphological studies (Heritage and Hetherington, 2007; Milan *et al*., 2007), yet the application of this method has not been as readily applied in aeolian research. This chapter explores the applicability of TLS to capture in-situ aeolian ripples during active saltation. Firstly the ability of the TLS to accurately measure aeolian ripples will be analysed. Then, ripples migrating during active saltation will be measured in order to produce an overall sediment budget using the morphologic method. The accuracy and reliability of these findings will then be studied in order to evaluate the usefulness and potential future applications of TLS within aeolian environments.

4.1 Study Site

Field experiments were undertaken in the Great Sand Dunes National Park, Colorado (Figure 4.1). Two study sites were used within the park. Scans of ripple patches were collected on a parabolic dune on the Eastern boundary of the park (site location: 37.771° N 105.502° W), whilst scans of ripples migrating during active saltation were collected on a parabolic dune on the South-Eastern boundary of the park (site location: 37.695° N -105.581° W).

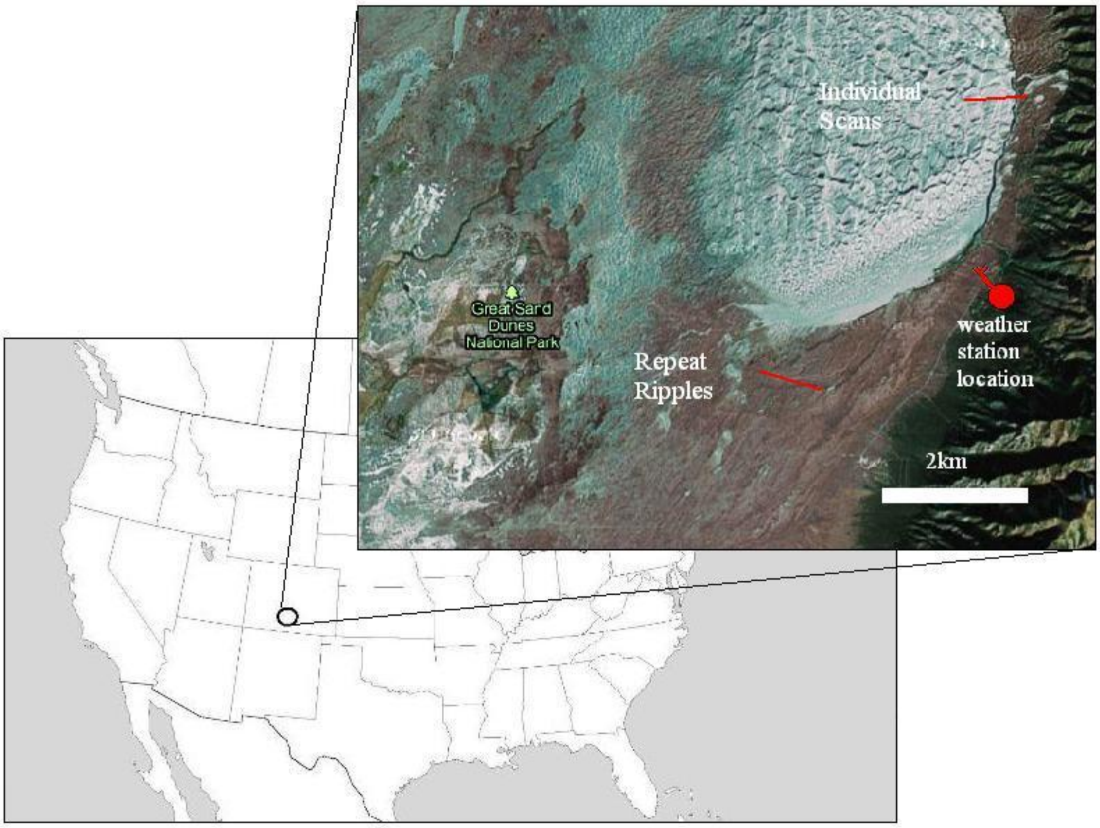

Figure 4.1 Map showing the location of the Great Sand Dunes National Park study site location and nearby weather station.

4.2 Static Ripples

In order to determine the influence of TLS incident angle when scanning in-situ ripples, rippled beds were measured on a parabolic dune. Five distinct rippled beds formed during a previous saltation event were measured at increasing incident angles (Figure 4.2). During the experiment, no active saltation was observed, so it can be assumed that the ripples remained static throughout the experiment.

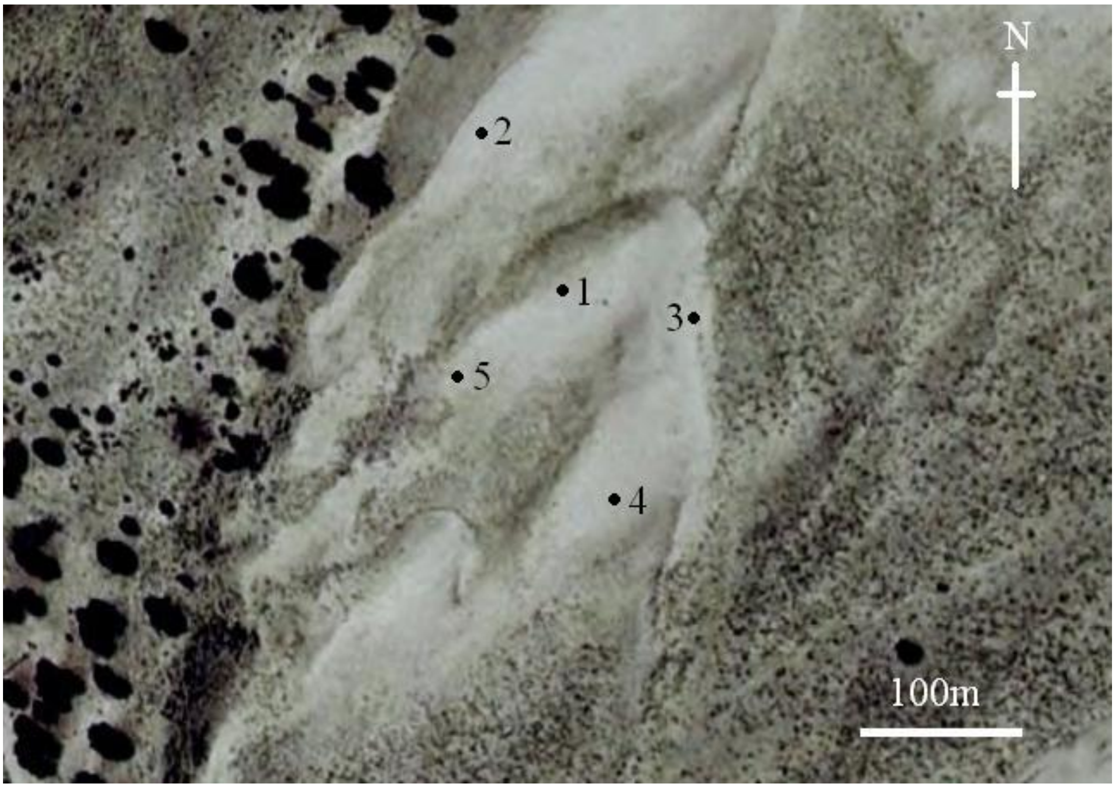

Figure 4.2. Map showing the locations of the five rippled patches measured during the experiment. Source: Google Earth, site location.

Measurements were collected using a Leica Scanstation TLS at a specified resolution of 1.4mm and a scanner height of 1.5m. Distances from the scanner to the bedform ranged from 5-13m. See Chapter 3 for detailed TLS specifications. The scanner location was moved for each individual scan, however point cloud registration was not necessary as the individual point clouds were analysed separately. Single scans were collected at each location. Collecting measurements on different areas of the parabolic dune enabled a range of incident angles to be investigated as the ripples were superimposed onto the parabolic dune (Wilson, 1972) changing the underlying gradient and therefore the incident angle of the incoming laser beam. Incident angles, calculated trigonomically based on the TLS height and distance from the centre of the bedform, ranged from 22-39°. The ripple patch sizes ranged from 28-52cm^2 to enable a larger number of ripples to be collected depending on the patch. Scan point density ranged from 2.85-28.32 points per cm^2 displaying a similar trend to those from the control experiment (Figure 3.7). A full summary of the five ripple patches measured is shown below (Table 4.1).

Table 4.1: Scan incident angle, patch size, number of ripples measured, point cloud density and the location of each ripple patch scanned.

Scan	Scan Incident Angle (°)	Patch Size (m)	Number of Ripples Measured	Point Density (points per cm^2)	Position on Dune
1	22.76 ± 0.06	0.74 x 0.71	2	2.85	crest
2	26.24 ± 0.01	0.58 x 0.57	7	8.34	arm
3	30.54 ± 0.01	0.56 x 0.46	6	14.05	crest
4	33.52 ± 0.02	0.69 x 0.58	7	10.09	stoss
5	39.79 ± 0.01	0.52 x 0.54	11	28.32	arm

4.3 Post Processing

Point cloud processing was undertaken using Leica Cyclone 5.8 (See previous chapter, Section 3.4, for a more detailed description). Registration of the point clouds was not necessary as the scans are not spatially relevant to each other. The point clouds were detrended so that the rippled bed sat on a horizontal plane and manually cleaned by deleting any points surrounding the bedform of interest. The patches were then rotated so the long axis of the ripple was parallel to the y axis. No points above the bed surface were removed. The individual scans were exported as .xyz files.

4.4 Static Ripple Scan Results

Ripple wavelengths and amplitudes were extracted using the same methodology as in the previous chapter (Section 3.7). The scan data from the static scans were gridded onto an arbitrary grid, giving a mean of the elevation within that cell. Cell resolution was set at 0.002mm as this proved to provide the most accurate ripple representation in the control experiment (Figures 3.12 and 3.13). Five cross sections per rippled patch were extracted from the gridded data, each cross section was the same length as the ripple patches and were rotated during post-processing. Each cross section was analysed within Matlab using an automated code to extract the highest and lowest points within the cross section profile. Metrics were calculated following the same methods as the control experiment (Section 3.7, page 61) and the results shown in Table 4.1. The calculated amplitude values were then multiplied by the cell resolution in order to produce a distance value. A mean was taken for each amplitude and wavelength over the five cross sections. This process was repeated for each of the five static ripple scans produced. The results from the wavelength and amplitude analysis are in Figure 4.3 and 4.4 respectively.

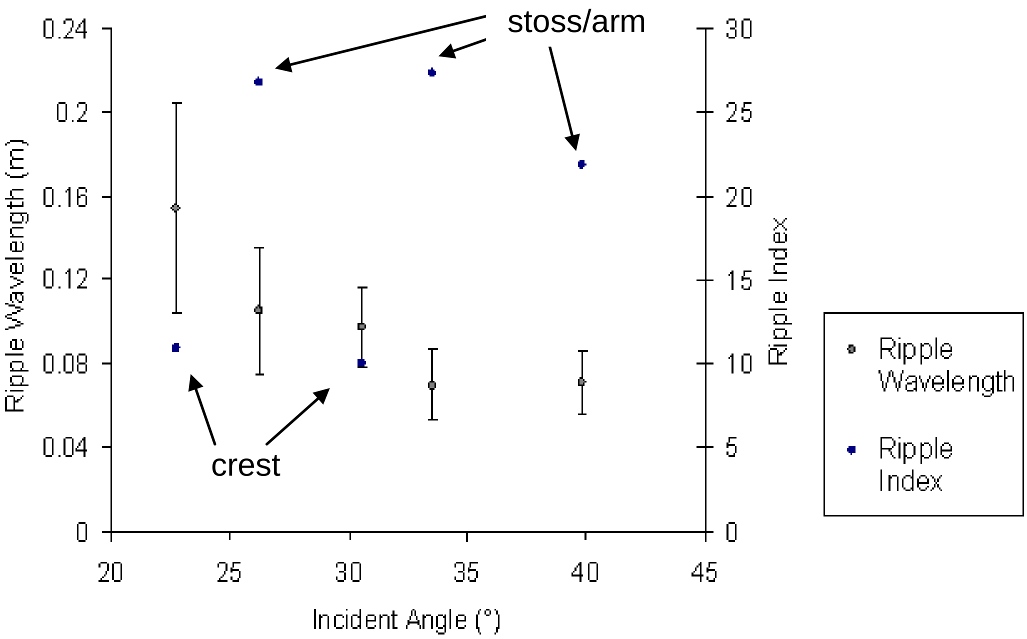

Figure 4.3 The average ripple wavelength and index at increasing incidence angles. Horizontal error bars (minimal) show variation in incident angle over the bedform and vertical error bars show the error as calculated at that incident angle in the previous chapter.

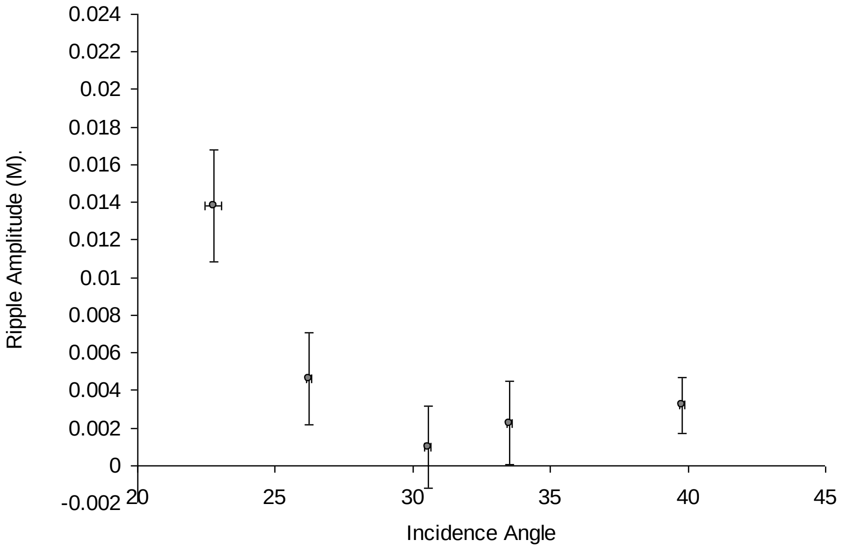

Figure 4.4 The average ripple amplitude at increasing incidence angles. Horizontal error bars show variation in incident angle over the bedform and vertical error bars show the error calculated at that

The results show the range of amplitudes and wavelengths experienced at different incidence angles. The error bars show the expected error at the calculated incident angle, based on the results from the previous chapter. The ripple amplitudes range from 13.8- 10mm (16.8-8mm including error) and wavelengths of 154-70.1 mm (204-56mm including error). These values all fall within ranges previously observed on rippled surfaces (Bagnold, 1941; Sharp, 1963; Lancaster, 1995). Amplitude measurements decrease at low incidence angles (22-30°) before showing a slight increase at greater incidence angles (30-39°). Wavelength measurements show a more uniform decrease with incidence angle. These trends are similar to errors observed when scanning fixed bedforms in the control experiment (Chapter 3, Figures 12 & 13). The ripple index (calculated as the ratio of wavelength to height) at the increasing incident angles range from 10-27 (Figure 4.3). These values fall into ranges previously observed (Bagnold, 1941; Sharp, 1963) who have observed values ranging from 10-70. The ripple index varies depending on the location of the ripples on the dune, with the ripples on the crest having a lower index value (10-12) than those on the stoss slope or dune arm (23-27). It has been documented that the most significant control on ripple index is the grain size, with coarse grains giving rise to larger ripple index values (Sharp, 1963). Grain size measurements were not collected during the fieldwork; however, previous studies on dune grain size sorting suggest coarse grains are concentrated at the base of the dune, with the finer grains accumulating at the crest (Lancaster, 1982; Watson, 1986). This is consistent with the ripples and their associated index values observed in this study.

During the field experiments it was not possible to obtain independent measurements to validate the TLS data. The decreases observed with increasing incidence angle could be explained by natural variation within the rippled bedforms. It is therefore difficult to differentiate between error associated with incident angle and location. As all of the ripple dimensions, index values and predicted errors fall within natural ranges of ripple dimensions, it can be concluded that the TLS is a viable tool to measure aeolian ripples from a single scan location during active sand transport.

4.5 Migrating Ripples

To explore the use of TLS during active transport, an experiment was devised to scan migrating ripples in order to capture pertinent metrics and explore the possibility of calculating net volumetric change through the ripple field. The field experiment was conducted on the 17th May 2010 on the crest of an active broad nose parabolic dune within the Great Sand Dunes National Park (Figures 4.1 and 4.5). Repeat scans were undertaken during an active saltation event in order to capture the topography underlying the saltation cloud and document ripple migration.

Figure 4.5. Map showing the location of the repeat ripple experiment. Source: Google Earth.

During the measurement period, wind data was recorded at a location 3km away from the study site (Location: 37.727° N -105.511° W) at a height of 6.09m. Wind direction was predominantly South-Southwesterly (approximately 205°) but swung round to West-Northwesterly for the final two scans. The wind strength initially dropped from around 4m/s^{-1} at the time of the first scan to around 3.1m/s^{-1} before picking up again to around 3.5m/s^{-1} at the same time as the change in wind direction (Figure 4.6).

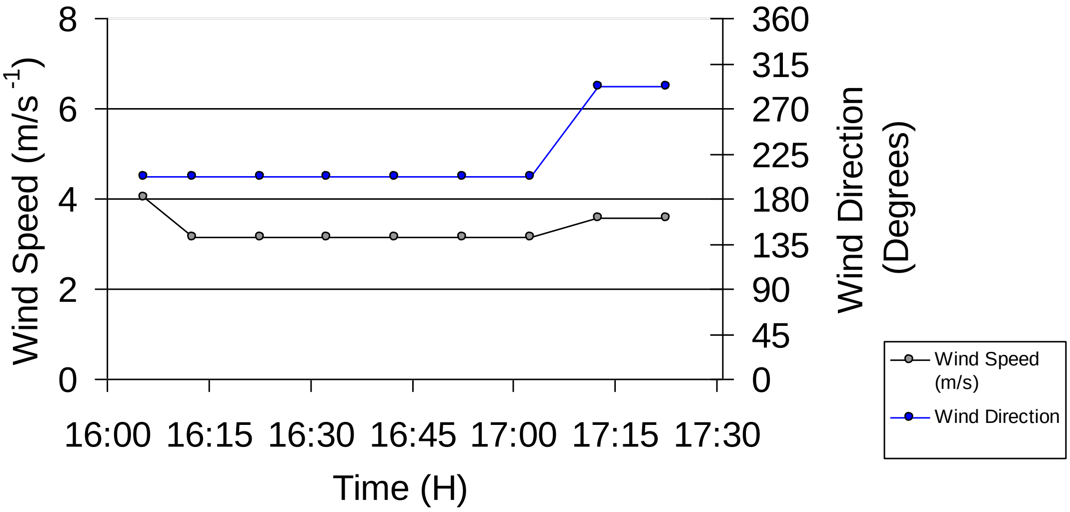

Figure 4.6 Wind conditions during the study period, as measured from the nearby weather station.

Numerous studies concerning aeolian ripples plot wind speed against ripple migration rate (Bagnold, 1941; Sharp, 1963; Lorenz, 2011) and these are often directly compared, despite differences in the height that the wind speed is measured (Lorenz and Valdez, 2011). As wind velocity varies with height above the bed, it is more useful to consider shear velocity when looking at relationships between wind and process. Shear velocity was calculated using the Prandtl-von Karman equation:

$$\frac{u}{u_*} = \frac{1}{k} \ln \frac{z}{z_o} \tag{4.1}$$

Where u is the velocity recorded at height z (m), z_o (m) is the aerodynamic roughness length of the surface (assumed to be 2mm due to a saltating surface), u_* (m/s) is the shear velocity and k is the von Karman constant (0.4).

Again, a Leica Scanstation was used to collect surface measurements. It was deployed at a height of 1.5m facing the nose of the parabolic dune providing more favourable laser incident angles than a horizontal bedform. This position was also downwind of the predominant wind direction to reduce the influence of the scanner on the local wind conditions. Incidence angles ranged from 21.8-17.35°. The rippled surface was measured eight times in total over a 74 minute period (Table 4.2), with intervals ranging from 2-27minutes depending on saltation activity. Each scan had a specified resolution of 1.4mm at a distance of 5m and measured an area 0.405 by 1.465m. Each scan took approximately 78 seconds to complete. Saltation rate was intermittent throughout the study, ranging from high visible saltation to no saltation (Table 4.2). Note that the saltation activity was observed at the start of each scan, and fluctuations in the extent of saltation intensity may have occurred during the scanning itself. During saltation events, ripples were observed to be migrating on the lee slope and along the crest of the parabolic dune. It is assumed that the majority of sediment transport and ripple migration occurred between scans, although it is acknowledged that some transport occurred during the scan period itself (Nield *et al.*, 2011).

Table 4.2. Field data and observations from the ripple study site.

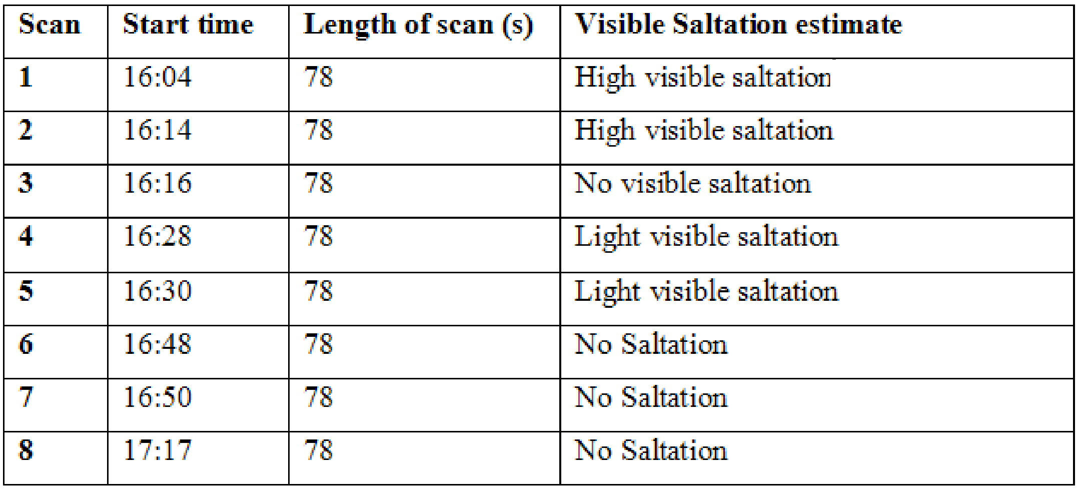

Scan	**Start time**	**Length of scan (s)**	**Visible Saltation estimate**
1	16:04	78	High visible saltation
2	16:14	78	High visible saltation
3	16:16	78	No visible saltation
4	16:28	78	Light visible saltation
5	16:30	78	Light visible saltation
6	16:48	78	No Saltation
7	16:50	78	No Saltation
8	17:17	78	No Saltation

with a small fraction of coarse grains, granules and pebbles (Lorenz and Valdez, 2011). The sand transport threshold for grains of this diameter according to Bagnold (1941) is 0.21 m/s^{-1}, above the shear velocities recorded in this study.

However, Nickling (1988) observed that transport is initiated over a range of shear velocities either side of the threshold, a finding supported by Baas and Sherman, (2006). As the surface of interest was on the lee side of the dune, the wind was likely to be turbulent, due to potential flow separation and back flow eddies (Lancaster, 1996) however this is difficult to ascertain, due to a lack of local wind measurements. The distance of the weather station from the study site means that local differences in wind speed, topographic influences and turbulent fluctuations are not accounted for.

4.6 Post Processing

A similar approach was taken to point cloud processing as in Section 4.3. Again, registration was not necessary as the scans were all conducted from the same position. As the scans were collected during active transport, laser return signals were collected from both the surface and from saltating particles. Despite saltating particles being much smaller than the laser footprint (4mm), a dense cloud of saltating particles will return a signal above the surface (Nield and Wiggs, 2011). As this study is focussed on the bedform dynamics beneath the saltating cloud, it was necessary to remove all points located above the rippled surface. This was achieved using a point filtering method developed by Nield and Wiggs (2011). The filter was applied to each point in the point cloud, analysing the relationship between point pairs in a $0.01m^2$ area (Figure 4.7) as utilised by Nield and Wiggs (2011). The filter then separated points based on the angle between point pairs. If the angle exceeded the angle of repose (set at 35°) it was removed from the dataset. This was repeated across the point cloud until a bare surface was left. This data was then gridded onto an arbitrary grid using linear interpolation with a resolution set at 2mm. This process was repeated for each dataset.

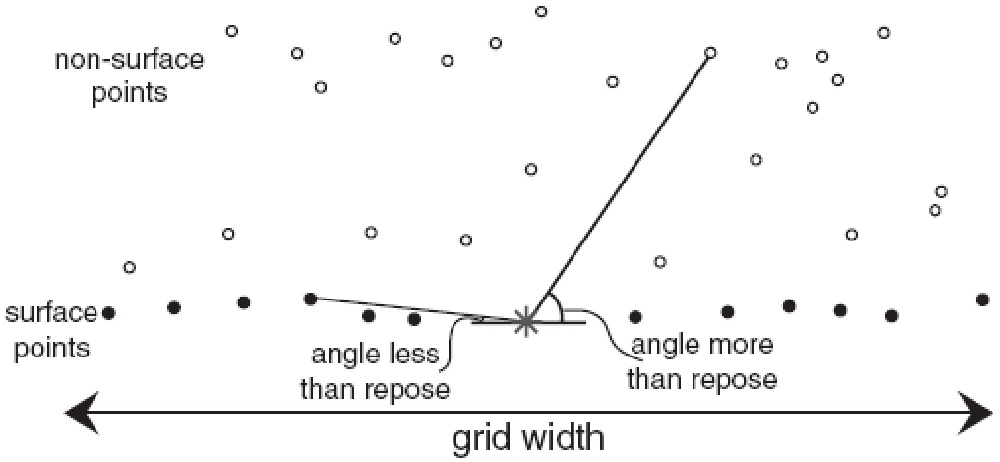

Figure 4.7. Two dimensional schematic showing the filtering method used to remove saltating grains from the laser scan point cloud. Black points represent surface points whilst white points represent points classified as saltating points. The star point represents the point where the filter is being applied. Image source: Nield and Wiggs (2011, p274)

In each dataset, a cross section was taken and ripple crests along that transect were extracted, using the same code as Section 4.3, giving the position of each ripple. The cross section was analysed visually to ensure no ripple interactions, such as y junctions were present. To calculate migration rate, starting with the second set of scan data, the location of the ripple crest was subtracted from the corresponding ripple in the previous scan. This gave the number of cells moved by the individual ripple which was then multiplied by the grid resolution to give a migration distance between subsequent scans. The migration rate was then calculated by dividing the distance moved by the time between each scans. This process was repeated for five profiles in each scan data set, and an average ripple migration rate was generated. The results of this analysis are shown in Figure 4.8.

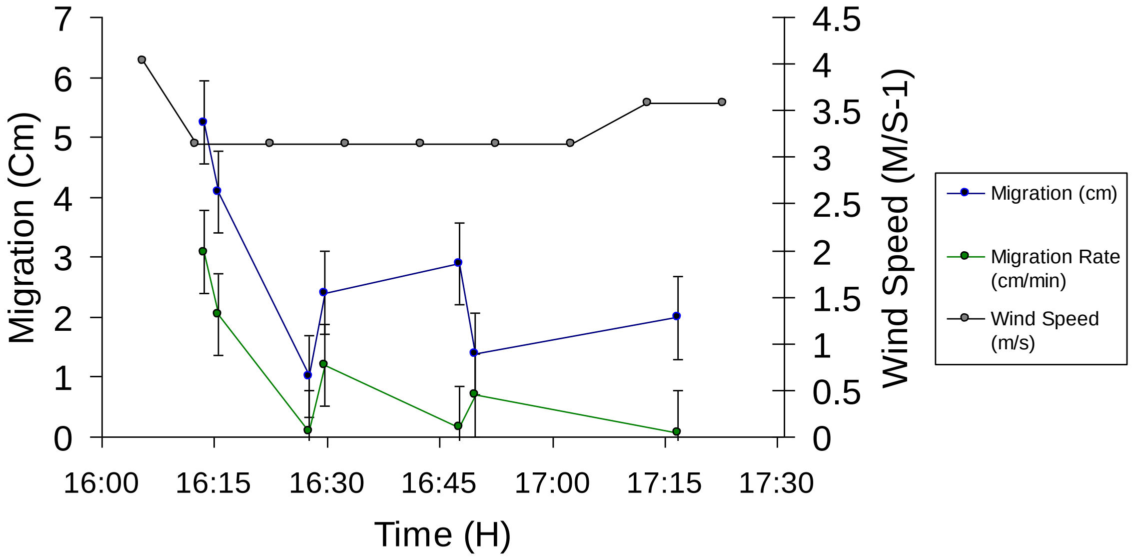

Figure 4.8 Ripple migration rate over the study period. Error bars represent the estimated error, calculated in the previous chapter.

The results show a decrease in ripple migration rate over the study period, from 3cm/minute to 0.08cm/minute. This coincides with a slight decrease and levelling of shear velocity throughout the study. The migration rates largely correspond with the field observations, with the fastest migration rates occurring during periods of highest visible saltation (Table 4.2), though it is recognised that further saltation, and therefore migration, could have occurred between scans. Scans were completed in 78 seconds, so up to 3cm additional migration could have occurred during the scanning process, based on the fastest migration rate. However, a visual check on the scan data revealed no crest line deviation along the ripple, suggesting this impact to be minimal. The majority of migration rates are within ranges previously noted by Sharp (1963) who observed ranges of 0.9-8.1cm/minute in the field. In the previous chapter, an estimated error for ripple wavelength was calculated. This has the potential to be used when calculating ripple migration rates to give confidence estimates with the data. The data was collected at an incident angle of 17-21° so therefore the error expected in ripple crest position is ±0.83cm (Figure 3.12). This is represented by the error bars on both the net ripple migration and migration rate (Figure 4.8). This error represents a significant proportion of the recorded migration rates, especially when migration rates are low. At the fastest migration rate (3.08cm/minute), 26% of that value can be viewed as erroneous. The slowest calculated migration rate (0.07cm/minute) is significantly lower than the estimated error, making it difficult to distinguish real geomorphic change from the noise associated with the data.

One interesting observation from the data is the apparent migration during periods where no saltation was observed to be occurring, and shear velocity is below the threshold required for transport. Migration rates of 0.07, 0.08, 0.16 and 0.69cm/minute were observed, below migration rates previously observed by Sharp (1963). This is either caused by saltation occurring between scans that was not observed, or errors within the laser scan data. Assuming that scan error caused these anomalous results, this can be used to provide a proxy for estimating scan error. As the ripple profile extraction method is automated, mixed pixels, that have not been removed by the filter, have the potential to produce inaccurate ripple crests and troughs within the ripple cross sections.

Mixed pixels above the surface but below the 35° threshold will remain in the data. This has the potential to influence the position of the crest if the mixed pixels falls either side of the true crest. Assuming that saltation and subsequent transport through impacts, are the only mechanism by which ripples migrate, and the measured migration rates during periods of no active saltation are caused by errors within the scan data, the observed migration rate during periods of no saltation have the potential to act as an additional method to estimate error within the data. The greatest migration distance calculated when no saltation was observed to be occurring was 0.69cm. This value is lower than the error calculated in the previous chapter, however still represents an error of 22% of the fastest migration rate.

Despite a constant mean wind speed throughout the experiment, migration rates show large fluctuations over the study period. It should also be noted that throughout the experiment, shear velocity was below the fluid threshold typically considered for ripple migration (Zimbleman *et al.*, 2009). However as the weather station was located over 3km from the study site, it is difficult to apply the collected wind data to the study site as it does not account for local wind speed variation, topographic influences, fluctuations due to turbulence and differences in surface roughness (Baas, 2008). The time between scans is also non-uniform which exaggerates the apparent fluctuations for the total migration distance. Ripples are also likely to have migrated during the scanning process. The scanning took 78 seconds to complete, and Sharp (1963) recorded migration of 2.5cm over the same time frame at comparable wind speeds. Maximum rates of 3cm/minute were recorded in this study.

A potential problem arising when using an automated cross sectional approach is that aliasing of ripples, whereby one cannot be sure that the same ripple is being measured each time (Lorenz and Valdez, 2011). This is especially prevalent when the time taken for a ripple to propagate one wavelength and the time between scans are similar. In this situation the scanned data would show little or no apparent migration, as one ripple would ‘aliase’ into the same position vacated by the next ripple. In reality relatively significant ripple propagation has occurred, introducing discrepancy between field observations of saltation activity and calculated migration rate.

The effect of aliasing can be analysed by comparing the estimated migration distance with the wavelength of the ripples studied. Average ripple wavelength for the study area was 12.2cm. Only one scan period experienced migration greater than the ripple wavelength (Table 4.3) and this was the scan that occurred during the period of greatest wind speed. Caution should be taken when using this method to asses the likelihood of ripple aliasing, as the migration rate is calculated using potential aliased ripples. Therefore if aliasing has occurred, the migration rate will be different. However in this case, the majority of distances migrated between scans are much shorter than the wavelength. Future studies should employ shorter scan sequences to reduce the likelihood of ripple aliasing occurring.

Table 4.3 Ratio of ripple migration/ripple wavelength

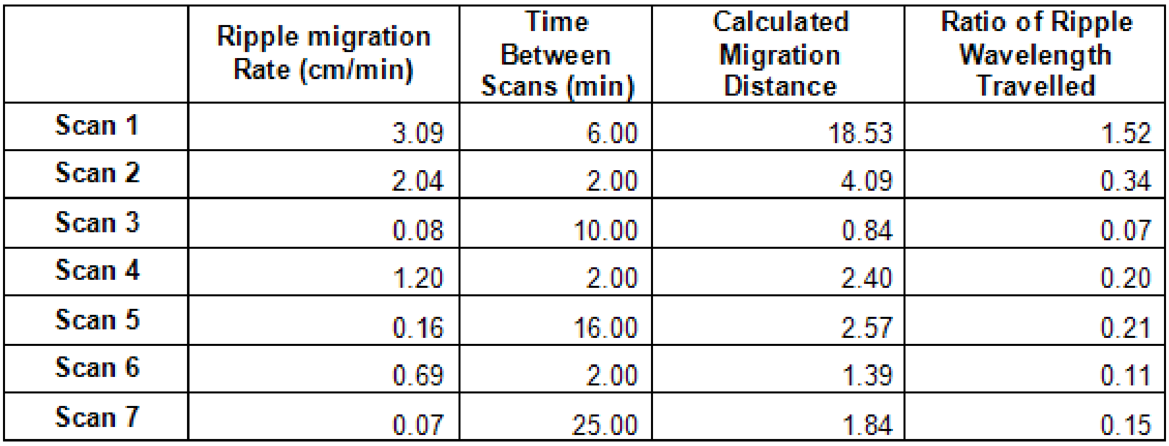

	Ripple migration Rate (cm/min)	Time Between Scans (min)	Calculated Migration Distance	Ratio of Ripple Wavelength Travelled
Scan 1	3.09	6.00	18.53	1.52
Scan 2	2.04	2.00	4.09	0.34
Scan 3	0.08	10.00	0.84	0.07
Scan 4	1.20	2.00	2.40	0.20
Scan 5	0.16	16.00	2.57	0.21
Scan 6	0.69	2.00	1.39	0.11
Scan 7	0.07	25.00	1.84	0.15

Whilst the automated approach tracks subsequent changes in the cross section, any bedform interactions such as bedform splitting or merging (Sharp, 1963; Kocurek *et al.*, 2009) are likely to influence the measured migration rate by shortening or lengthening the wavelength between ripples. Defect interactions such as creation or repulsion are likely to have an even greater influence using this method due to their proximity to other ripple crestlines and because they move at greater speeds than typical wind ripples (Anderson and McDonald, 1990; Kocurek *et al.*, 2009). However, as the results were averaged the potential for this happening is minimised. Obtaining ripple migration measurements using more traditional techniques such as using markers (Yizhaq, *et al.*, 2009; Zimbleman *et al.*, 2009) or time lapse photography (Andreotti *et* a*l.*,2006; Lorenz *et al.*, 2010) alongside the TLS was not possible during the field work. Independent measurements would provide the ability to validate the calculated migration rates and reduce uncertainty in the data as a result of aliasing. However, as no independent data is available, the results obtained must be treated with a degree of uncertainty, and obtaining independent measurements is necessary for future work in this field.

4.7 Morphological method

As previously discussed, the real benefit of terrestrial laser scanning is its ability to collect accurate, high-resolution topographic data in dense point clouds. Performing repeat scans enables the accurate monitoring of geomorphic change on the bed during active saltation. The above analysis has shown that capturing in-situ aeolian ripples is feasible using TLS, however the methods used to detect change between subsequent scans should be treated with a degree of uncertainty due to errors in the scan data. The morphologic method is applied to the scan data in this section to test the applicability of using this technique in aeolian environments.

The repeat scan data collected from the broad nose parabolic dune were used to analyse surface changes during active saltation. Digital elevation models from each scan were produced using the raw surface data, filtered to remove saltating particles or mixed pixels, and averaged over 0.002 m grid cells (See Nield *et al.*, 2011). DEMs of Difference (DODs) were produced by subtracting the elevations on a cell by cell basis from the subsequent scan. In total, seven DODs were produced, showing the bed surface change throughout the study period (Figure 4.9). The wind direction and therefore direction of ripple migration is from left to right. Areas of erosion are highlighted in blue and deposition as red.

The DODs displayed highlight the geomorphic change occurring over the study period. Rippled patterns are clearly visible on five of the DODs (Figure 4.9 a, c, d, e and g) as areas of erosion and deposition. This suggests that ripple migration is detected by the TLS. The ripples are seen to be propagating through the study area, with ripples entering from the left and exiting from the right.

Two of the DODs (Figure 4.9 b and f) have no distinct areas of erosion or deposition clearly visible suggesting that no ripple migration has occurred. For scan f, this corresponds with the previous observation that no significant migration has taken place. However, for DOD b, no ripple migration has occurred, despite a relatively high (2.04cm/minute) migration rate calculated using the cross sectional analysis. A possible explanation for this discrepancy is ripple aliasing in the same manner as discussed above, or that the cross sectional analysis was significantly influenced by the effect of mixed pixels.

The histograms displayed for each DOD correspond to the activity shown within the DOD. DOD’s with no distinct areas of erosion and deposition (e.g DODs b, d, and f) are relatively symmetrical with low variation about the modal value. DOD’s with distinct areas of erosion and deposition (e.g. DODs a,c,e and g) show a greater range of values, as well as being positively skewed. This suggests that whilst ripples are migrating, the bedform surface is net erosional.

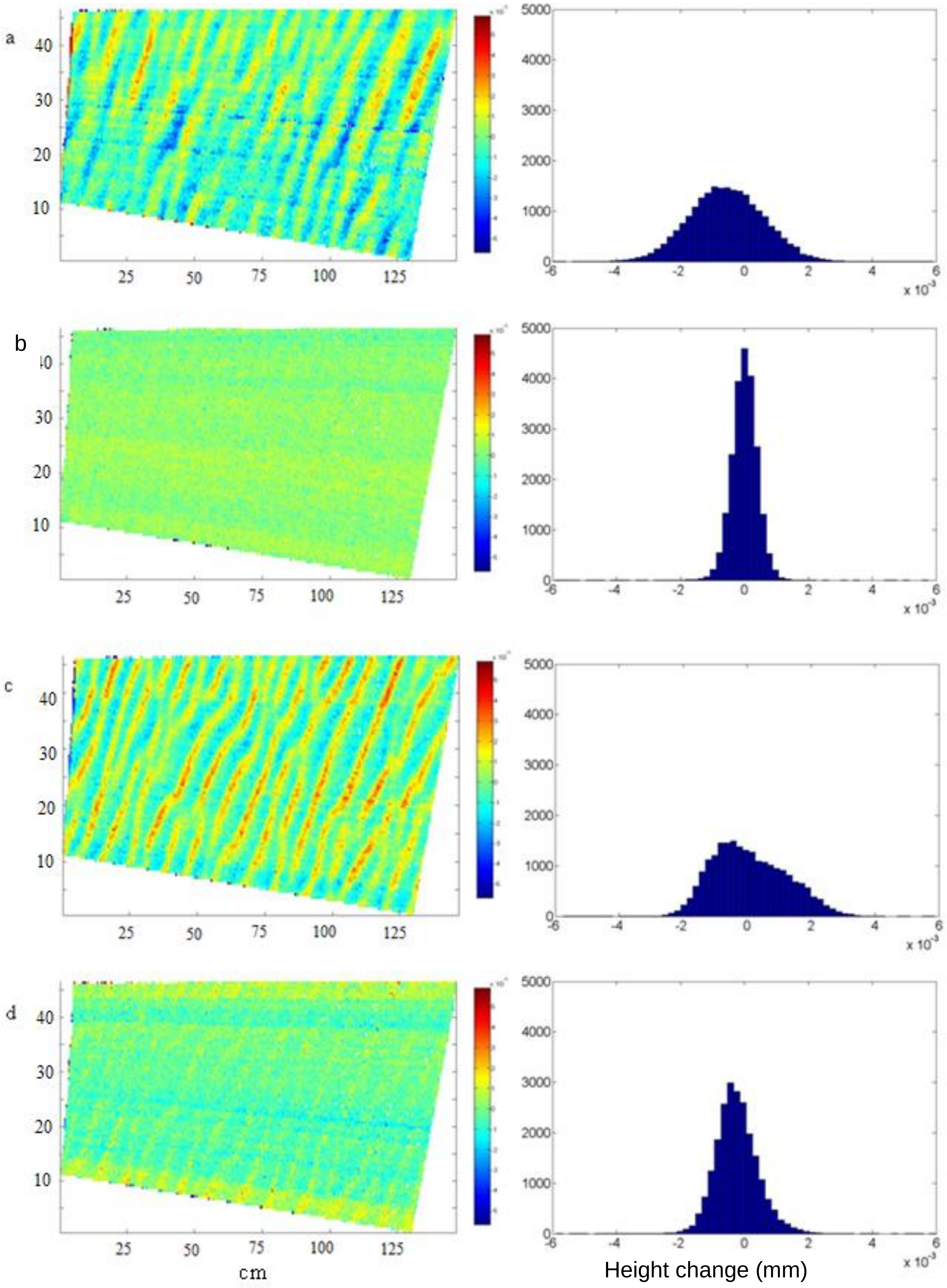
a
b
c
d
10
20
30
40
25
50
75
100
125
cm
0
1000
2000
3000
4000
5000
-6
-4
-2
0
2
4
6
x 10^-3
Height change (mm)

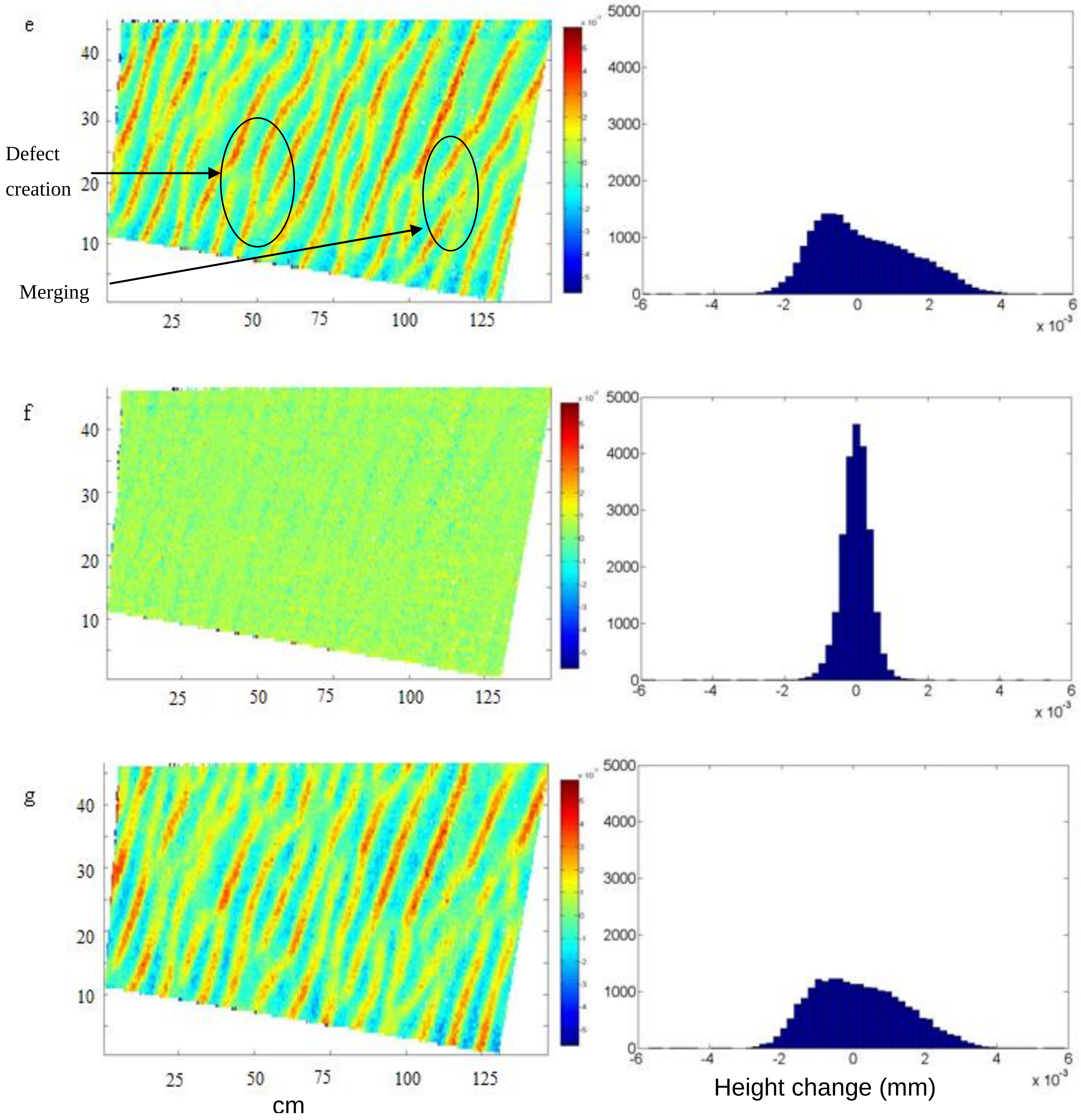

Figure 4.9. DEMs of Difference (left) produced for the 8 scans collected during the experiment. X and Y values represent number of cells, each cell is 0.002m^2. Histograms (right) show distribution of positive and negative values within the DOD. Bedform interactions are shown on DOD e.

Specific bedform interactions can be tracked through the sequential DODs (highlighted on DOD e). Assuming that aliasing is minimal between scans, ripples can be tracked as they propagate through the scans. Merging ripples are evident whereby smaller ripples overtake and merge with larger ripples. This is a constructive bedform interaction whereby the system progresses towards larger ripples, widely spaced and less frequent. The creation of defects can be observed in the DODs above (Figures a,c,e and g), as crestlines breaking up. Again, this process is common in initial state bedform fields experiencing uni-directional flow (Jerolmack and Mohrig, 2005). This process is regenerative, counteracting the constructive processes by increasing the number of bedforms in the system (Kocurek *et al.*, 2010). These defects can be observed migrating through the DODs at a faster rate than the larger ripples, as they merge with other bedforms. This is known as lateral linking, a constructive process which reduces the number of defects in the system. Again, this is a process common in the early stages of bedform construction and is responsible for the extensive length of the crests seen in ripple fields (Sharp, 1963; Landry and Werner, 1994).

Surface volumetric change was calculated by multiplying the DOD elevation change present in each cell by the surface area of each cell ($0.000004m^2$). Each volume was then summed into depositional and erosional totals, producing a volumetric budget for the study area (Table 4.4). Columns 4 and 8 show the percentages of the study area experiencing erosion and deposition without taking into account measurement inaccuracies or a threshold change values. Over 99% of the study site experienced surface change in each DOD. The ripple field fluctuates from being net erosional to net depositional throughout the study. The majority of DODs experience close ratios of erosion and deposition, with the exception of DOD1 and DOD4, of which 68 and 67% of the area experience erosion respectively. This is reflected in the net volumetric change, with the largest volumetric change ($-0.00066m^3$ and $-0.00025m^3$) experienced in these two DODs. These DODs coincide with the fastest migration rate observed above (Figure 4.8) and suggest that surfaces are net erosional when undergoing intense saltation (assumed due to higher migration rates). These findings support those of Andreotti *et al* (2006) who noted global erosion on rippled beds during saltation. Initial state beds were more susceptible to erosion before a developed ripple state was achieved and global erosion was reduced. The bed observed in this study was subject to a change in wind direction at the start of the observation period, and this may be responsible for the higher erosion observed as the bedforms adjusted to the new wind regime.

Figure 4.10 shows the net volumetric change plotted against time. The overall trend shows a change from net erosional to net depositional throughout the study. This transition from net erosional to net depositional corresponds with both the drop in wind speed and reduced bedform migration rate supporting the argument above suggesting that during intense active saltation rippled surfaces are net erosional. Displaying net volumetric change per minute (Figure 4.11) shows the same overall trend with a larger rate of erosion observed at DOD4 than DOD1. This is similar to the trend displayed above (Figure 4.8) and again is likely to be a function of the short amount of time between scans from which DOD4 was derived, rather than a large increase in active transport. The increase in net transport may have been caused by a local increase in wind speed, again, however, due to the distance from the meteorological station and the 10 minute averaging of velocity measurements, this was not detected.

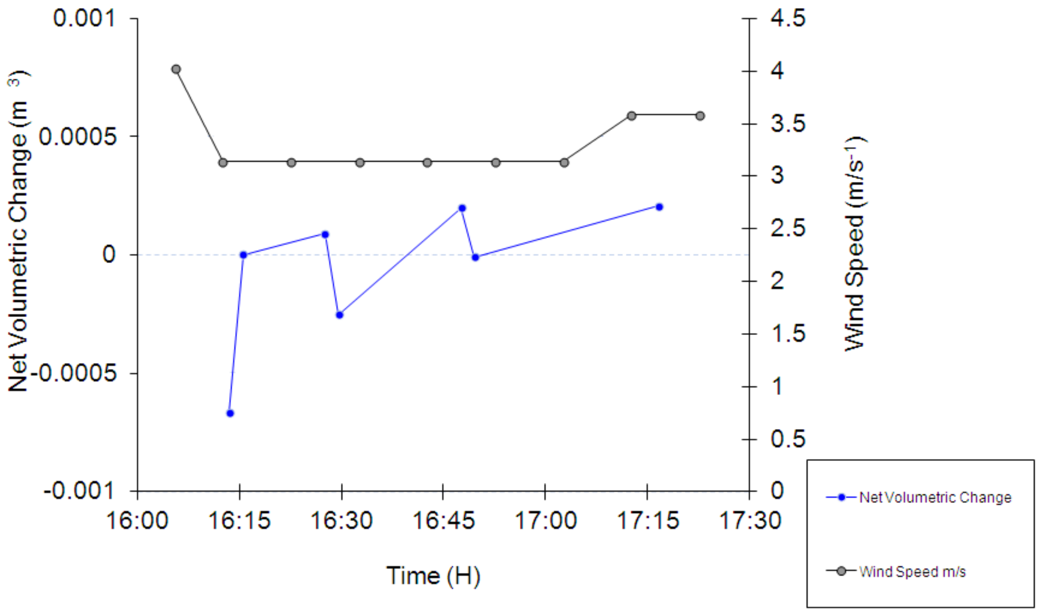

Figure 4.10 Net volumetric change calculated, and shear velocity plotted against time.

Table 4.4 Morphologic analysis data

DEM of Difference	**Erosion**				**Deposition**				**Net Volumetric Change (m^3)**
	Total elevation change (m)	**Number of cells**	**Percentage Coverage of Area**	**Net Erosion (m^3)**	**Total elevation change (m)**	**Number of cells**	**Percent Coverage of Area**	**Net Deposition (m^3)**	
DOD1	-17.445	15068	68.2	-0.000990895	5.418	7012	31.8	0.000325	-0.000666
DOD2	-3.401	10853	49.0	-0.000170067	3.450	11274	51.0	0.000172	0.000002
DOD3	-9.564	11357	51.4	-0.000478177	11.367	10739	48.6	0.000568	0.000090
DOD4	-8.632	14830	67.1	-0.000431598	3.617	7268	32.9	0.000181	-0.000251
DOD5	-10.170	11188	50.6	-0.000508476	14.145	10923	49.4	0.000707	0.000199
DOD6	-3.458	10915	49.4	-0.000172908	3.282	11184	50.6	0.000164	-0.000009
DOD7	-9.666	10578	47.8	-0.000483289	13.793	11552	52.2	0.000690	0.000206

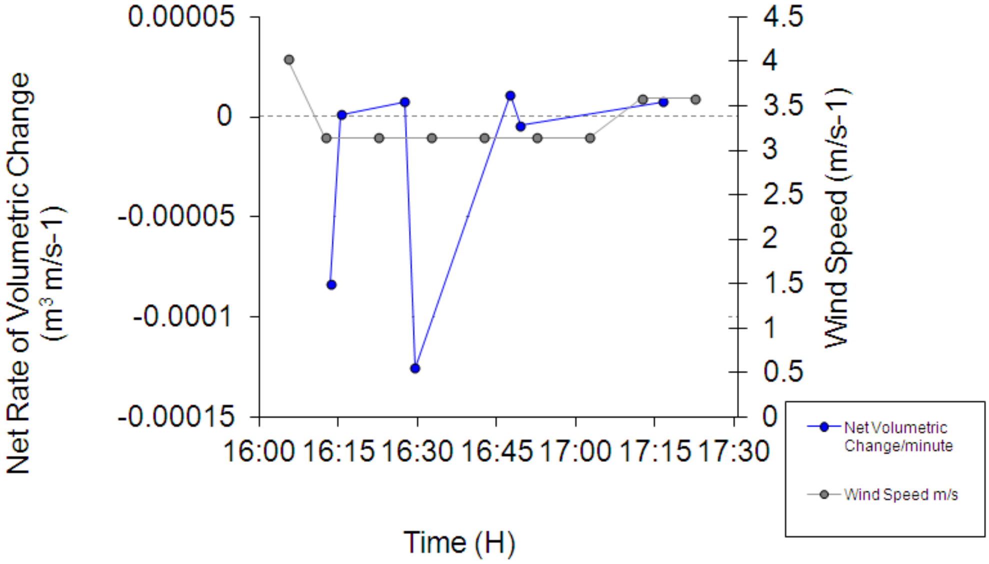

Figure 4.11. Net rate of volumetric change, calculated as change per time different between scans, and shear velocity, plotted against time.

The scanned area used in this study was determined by the best possible incident angle, rather than the number of features being measured. However, using the above morphologic analysis, the contribution of individual ripples within a sediment budget can be calculated. Dividing the net erosion, net deposition and net volumetric change recorded for each DOD by the number of whole ripples measured in each DOD gives an estimation of the contribution of each ripple to geomorphic change (Figure 4.12). Ripples measured 0.405m in length.

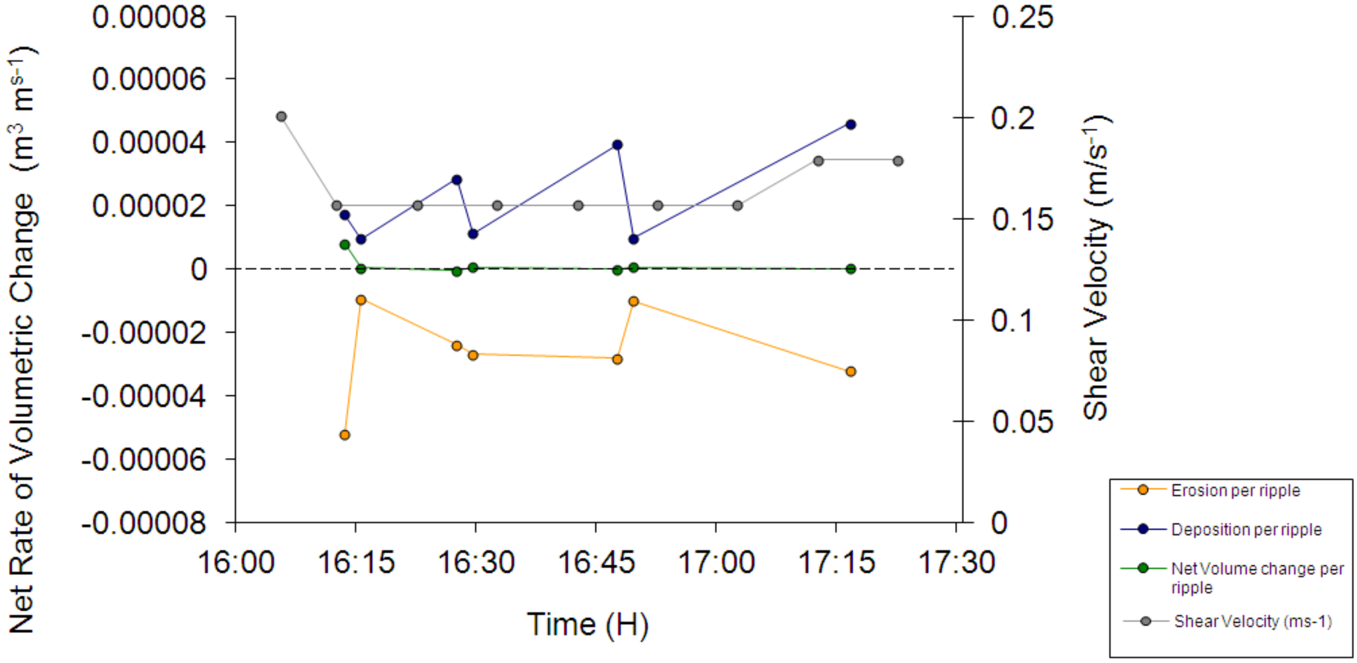

Figure 4.12. Morphologic budget estimated for each individual ripple measured within the DOD.

The individual ripple analysis shows similar trends to the overall morphologic budget. Overall the erosion decreased throughout the study period, and ripples switched from net erosional to net depositional. The ripple that experienced most change was recorded during the time of most active saltation, when an average of 0.00004m^3 of erosion occurred, 0.000016m^3 of deposition occurred with a net change of –0.000034m^3 occurring. This analysis provides an individual morphologic budget for each ripple, providing information regarding the reptating component of aeolian transport. Using this technique coupled with other aeolian transport measurement instruments could provide a more accurate estimation of the entire transport system.

4.8 Accounting for uncertainty within the DOD

Up to this point, the analysis has not considered errors within the DODs. Inherent errors within each DEM are propagated through the analysis and into the DOD (Wheaton *et al.*, 2010). It was shown in the last chapter that incidence angle has a significant impact on the overall quality of the DEM, and was quantified for increasing incidence angles. Therefore, in the absence of a validation data set, the error calculated in the previous chapter will be utilised in this study. Quantifying DOD error is essential in order to distinguish whether the geomorphic change observed is real, or inherent noise within the data. Quantifying DOD uncertainty has received attention within the literature (Lane *et al.*, 1994; Milne and Sear, 1997; Brasington *et al.*, 2000; Lane *et al.*, 2003; Wheaton *et al.*, 2010) and the typical approach to dealing with uncertainty is to apply a minimum level of detection ($_{\text{min}}$LoD), whereby change below a certain threshold is discarded (Brasington *et al.*, 2000; Wheaton *et al.*, 2010). This threshold is usually derived from a validation data set used as a measure of DEM quality (Milan *et al.*, 2007).

The application of a $_{\text{min}}$LoD is the approach used to quantify the level of DOD accuracy in this study. In the previous chapter the expected DOD error was estimated for increasing incident angles using a validation data set (Figure 3.15). The average DEM error associated with a scan incidence angle of 21° (the maximum incidence angle occurring in this study) was ±0.86mm. However the analysis of a DOD must account for the error within both DEMs and how this propagates into the final DOD. Following Brasington *et al*., (2003), Lane *et al*., (2003) and Milan *et al*., (2007) the standard deviation of the error was used to quantify uncertainty and can be calculated with the following equation:

$$_{\min}\mathrm{LoD} = t\sqrt{\sigma^2 + \sigma^2} \tag{4.2}$$

Where $_{\min}$LoD is the threshold level of detection, σ is the standard deviation of expected error in each DEM (calculated in the previous chapter) and *t* is the level of confidence selected for the $_{\min}$LoD. The value of *t* can be set at either 1σ which gives a confidence level of 68% (Lane *et al*., 2003) or 2σ which gives a 95% confidence limit (Brasington *et al*., 2000; Brasington *et al*., 2003). This study utilises a 95% confidence limit which results in a $_{\min}$LoD of ± 1.6mm. The $_{\min}$LoD was applied to each DOD and as such any geomorphic change observed beneath this threshold was removed on a cell by cell basis. A revised sediment budget was then calculated using the thresholded DOD to produce a net volumetric change. It should be noted at this point that the net volumetric change percentage is calculated from the absolute sum of both erosion and deposition, not the net difference, to avoid reaching a similar volumetric budget by chance. The results of the application of a $_{\min}$LoD are shown in Table 4.5.

Percentages of cells removed by the application of the $_{\min}$LoD ranged from 78-97% (Column 5) which represents a significant proportion of the total DOD surface area. This loss of information is manifested in the volumetric budget calculated from the thresholded DOD, with 90-97% value change from the erosion estimate and 89-96% of the deposition estimate when compared to the unthresholded estimation. As a result, the net volumetric change calculated from the thresholded DOD is significantly different to the unthresholded DODs. Net Volumetric change percentage difference ranged from 91-95% of information lost when a threshold is applied compared to the original DOD. The effect of applying the threshold to the net volumetric budget is displayed graphically below (Figure 4.13).

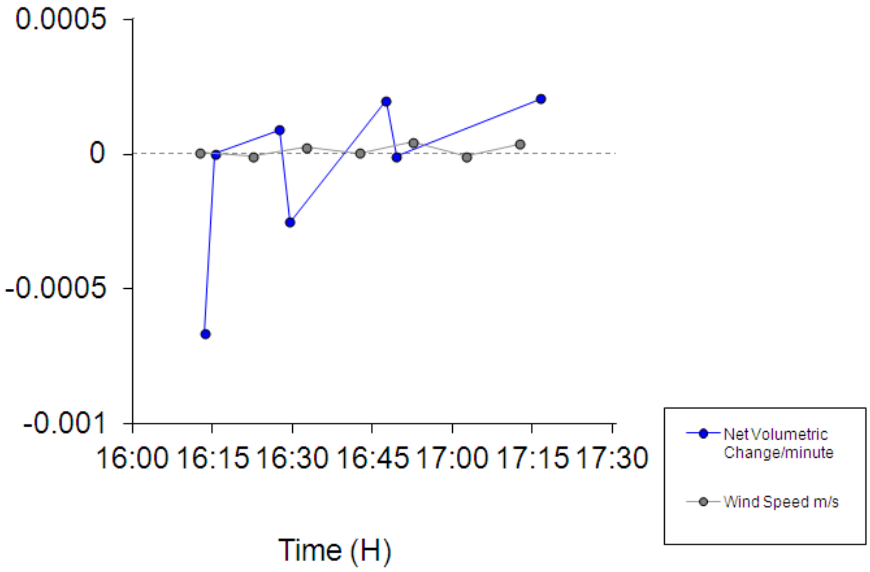

Figure 4.13. Calculated net volumetric change for both the unthresholded and thresholded DODs.

The application of the threshold has a marked effect on the overall volumetric budget calculated, with a significant reduction in estimated morphologic change occurring. Importantly, in the case of DOD2 there is a switch from being net depositional to net erosional after the application of the $_{min}$LOD. Similarly there is a switch from net erosional to net depositional in the case of DOD4. This is significant as it shows not only a decrease in estimated morphologic change, but also a reversal in what the DOD is representing. The performance of the DODs after applying the threshold reduces the significance of the original results. It is necessary to explore this result and offer some explanations and solutions.

4.9 Discussion

The large loss of data observed and variation between thresholded and unthresholded DODs is informative when trying to achieve an accurate estimate of morphological change. The threshold applied removes up to 97% of the observed changes as on a cell by cell basis, the majority of change falls within ± 1.6mm. However, the 1.6mm error threshold used offers an optimistic threshold level when compared to other studies utilising TLS to study morphologic change. Milan *et al* (2007) apply a $_{min}$LoD of 57mm when analysing daily geomorphic

Table 4.5 Volumetric change analysis before and after the $_{min}$LOD was applied and the percent of data lost when this threshold is applied. Net volumetric change percentage loss is calculated from the absolute volume change, not the net volumetric change.

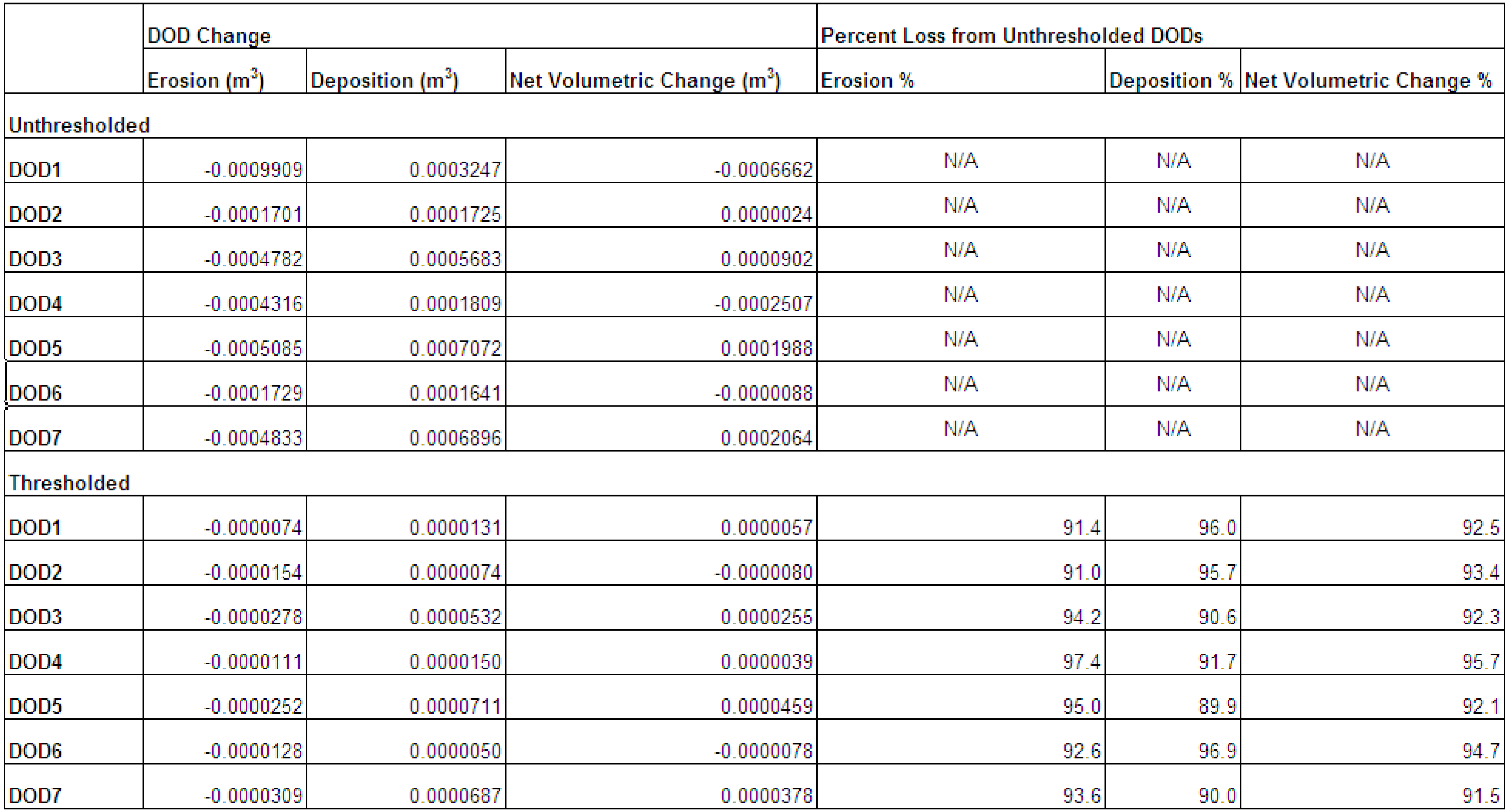

	DOD Change			Percent Loss from Unthresholded DODs		
	Erosion (m^3)	Deposition (m^3)	Net Volumetric Change (m^3)	Erosion %	Deposition %	Net Volumetric Change %
Unthresholded						
DOD1	-0.0009909	0.0003247	-0.0006662	N/A	N/A	N/A
DOD2	-0.0001701	0.0001725	0.0000024	N/A	N/A	N/A
DOD3	-0.0004782	0.0005683	0.0000902	N/A	N/A	N/A
DOD4	-0.0004316	0.0001809	-0.0002507	N/A	N/A	N/A
DOD5	-0.0005085	0.0007072	0.0001988	N/A	N/A	N/A
DOD6	-0.0001729	0.0001641	-0.0000088	N/A	N/A	N/A
DOD7	-0.0004833	0.0006896	0.0002064	N/A	N/A	N/A
Thresholded						
DOD1	-0.0000074	0.0000131	0.0000057	91.4	96.0	92.5
DOD2	-0.0000154	0.0000074	-0.0000080	91.0	95.7	93.4
DOD3	-0.0000278	0.0000532	0.0000255	94.2	90.6	92.3
DOD4	-0.0000111	0.0000150	0.0000039	97.4	91.7	95.7
DOD5	-0.0000252	0.0000711	0.0000459	95.0	89.9	92.1
DOD6	-0.0000128	0.0000050	-0.0000078	92.6	96.9	94.7
DOD7	-0.0000309	0.0000687	0.0000378	93.6	90.0	91.5

change on a pro-glacial floodplain, though this produced convergent scans from four different positions. The 1.6mm threshold is also an improvement on previous error estimations for single scans. The manufacturer guidance states the Leica scan station used has a precision as a standard deviation of 4mm (Leica Geosystems, 2007). Both Boeler and Marbs (2005), Hodge *et al.*, (2009a) and Hodge (2010) found an improved error estimation as a standard deviation of 2mm in laboratory experiments. However, these values are applicable to single scans, and are sure to propagate through the DOD analysis giving greater thresholds than those used here. Heritage and Hetherington (2007) found a mean error of 0.6mm when using TLS to measure smooth bedrock in fluvial environments which is more comparable to the level of errors found in this study. It should again be noted that in the absence of validation data, the uncertainty was calculated from a priori study and related to the uncertainty associated with incidence angle, not necessarily a typology of errors associated with using the TLS which is reflected in the relatively low $_{\text{min}}$LOD used.

The above suggests that the $_{\text{min}}$LOD used is less conservative than other studies utilising TLS. In spite of this, data loss is still high. This suggests that little surface change has occurred during the study. Without independent measurements of both ripple migration, saltation activity and local wind speed it is difficult to validate these results.

The method used to apply the $_{\text{min}}$LOD assumes the error is spatially uniform across the DOD. The result of this approach is to discard more useful data points than necessary where errors are low, and keep more data points than is necessary where errors are high (Wheaton *et al.*, 2010). Errors in DEMs have been shown to have a spatial bias, whereby uncertainty is higher in topographically complex areas (steep, high surface roughness, low survey point density), and lower in topographically simple areas (Wheaton, 2008). Lane *et al.*, (2003) apply a non-spatially variable $_{\text{min}}$LOD on the basis of wet and dry areas within a river catchment, however, this again is a relatively basic solution to the complex array of errors encountered within DEMs.

A possible improvement to the method utilised in this study is to apply a fuzzy inference system, developed by Wheaton *et al.*, (2010) which has been shown to reduce the level of data loss when performing DOD analysis as well as providing more meaningful results. The approach applies a set of three fuzzy set rules (data point quality, topographic complexity and survey point density) on a cell by cell basis to quantify the threshold level of detection. For example, an area with a high point density, high point quality and low slope angle, would have low uncertainty. This technique has the potential to be applied to TLS data in order to improve confidence that the data being removed is erroneous, and the data that remains represents significant geomorphic change. In the context of this experiment, ripple crests are likely to have lower uncertainty than ripple troughs due to fewer mixed pixels and higher point density and the fuzzy set rules would have to be modified for this. The use of TLS compared to GPS would also require a different method of quantifying individual point quality (Wheaton *et al.*, 2010 utilise point quality from the GPS). Ultimately, Wheaton *et al.*, (2010) found that the use of this method was more conservative than a standard $_{\text{min}}$LOD in that it discarded more data. Applying a more conservative threshold to the data would discard more data from the DOD analysis performed here and would leave very few true data points. The use of fuzzy inference techniques when quantifying uncertainty in DODs acquired with TLS is beyond the scope of this study and remains an area for further research.

Ultimately, in the context of aeolian ripples, the levels of change detected may simply be too low to produce accurate and reliable results when performing DEM differencing from TLS data, and requires instruments with higher resolution scanning ability. The level of morphologic change occurring in-between the 10 minute scans used in this study is low. Increasing the temporal intervals between scans, or scanning in a more active environment would allow a greater volume of geomorphic change to occur; this in turn would reduce the level of data loss. However the level of change detected must have an upper threshold for steady state migration as once a ripple propagates a full wavelength, the detected morphologic change would decrease due to ripple aliasing, despite an increase in real change. This is shown schematically in Figure 4.14.

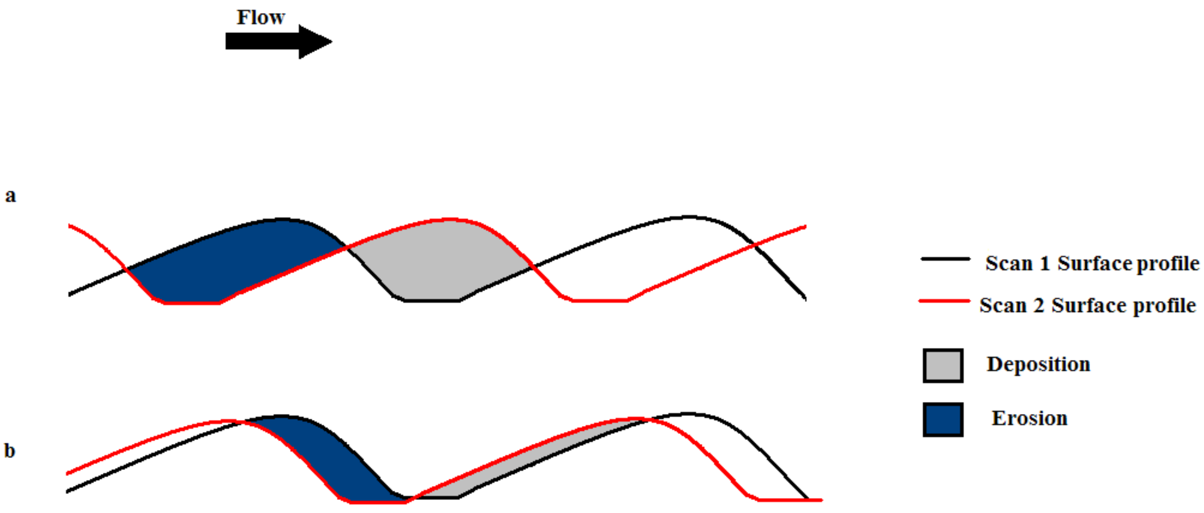

Figure 4.14. A schematic highlighting the profile changes occurring during ripple migration. Ripple translation is shown from the first scan (black line) to the second scan (red line). Areas of erosion (blue) and erosion (grey) are also highlighted for one propagated ripple. Ripple b migrates further than ripple a, however the surface profile change shows greater change to have occurred in profile a, known as aliasing (assuming wavelength remains constant).

The above conceptual profile shows that despite ripple b migrating further than ripple a, less change is observed volumetrically due to the ripple migrating almost an entire wavelength between scan times. This could potentially be solved by placing recognisable markers on each ripple before commencing each scan (See Sharp, 1963). However, this would be intrusive, negating one of the key benefits of using TLS in aeolian environments. Shortening the time between subsequent scans would reduce the likelihood of aliasing occurring (Table 4.3). A further problem in scanning such fast moving bedforms is that change is likely to occur whilst the TLS is conducting a scan. It was assumed that the majority of transport occurred between scans, however, it is likely that some transport occurred and the influence of this is difficult to ascertain.

The absence of independent measurement data makes it difficult to ascertain the accuracy of the results. However, the values obtained are plausible for both the surface area and for individual ripples. Previous studies estimate the reptating component of aeolian transport as 10-25% (Bagnold, 1941; Namikas, 2003) and this study has offered an alternative method to quantify this aspect. Further study is required to quantify the relationship between the saltating layer and the volumes of the ripples as they propagate. Deploying additional flux measurement devices such as sand traps and saltation probes alongside the TLS has the potential to provide a more accurate picture of the aeolian sediment transport system.

Whilst the morphologic change measurements recorded in this study are subject to data exclusion when accounting for error within the DEMs, the static ripple scans and migration rate calculations perform well. The scans of static ripples accurately capture the ripple morphology, and all ripple properties measured (amplitude and wavelength) fall within previously recorded ranges. The errors associated with performing scans of this type are shown to be low (Figures 3.12 and 3.13) and have a low impact on the results. Using TLS to capture ripples in this way is a useful tool to document quickly and accurately ripple profiles in the field. These can then be used as a validation data set to parameterise ripple formation models (Yizhaq *et al.*, 2004; Andreotti *et al.*, 2006; Manukyan and Prigozhin, 2009). Data sets of this type can also be utilised to document bedform interactions. Kocurek *et al*., (2010) state that very few time series data sets document interactions in natural bedform fields. The TLS provides the ability to capture bedform interactions at a high spatial resolution and in three dimensions and further work is required to understand these interactions at a 3D level. A further use of the scan data is to provide information regarding surface roughness, which can then be used within Computational Fluid Dynamic modelling (CFD) as a boundary condition (Hodge *et al*., 2009; Gartman *et al*., 2011).

Chapter 5: Thesis Conclusions

The purpose of this thesis was to develop a set of best practice principles to apply the use of terrestrial laser scanning in aeolian environments. These principles were then used to collect and analyse field data in order to provide a more accurate estimation of aeolian sand transport.

The TLS has been shown to be able to capture highly accurate, three dimensional topographic data. The use of this in aeolian environments is recognised as having great potential (Nagihara *et al.*, 2004; Bullard, 2006; Baas, 2008) and a set of best practice principles are important to develop, especially as the rapidly changing environments call for scans from single positions. Scanning geometry will therefore have a large influence on the overall accuracy of the results. Increasing the scan incidence angle to decrease laser footprint size has been shown to reduce the error value when scanning the same feature. The effect of incidence angle was shown to vary between bedforms. The incidence angle had a greater influence on the accuracy of ripple scans than for dune bedforms which should dictate field set ups in future studies.

As aeolian systems are subjected to rapid change, the ability to capture accurate data, with minimal error, quickly, is a useful tool. However the effect of incidence angle is not limited to studies utilising single, rapid scans but should also be considered when using TLS to scan surfaces from multiple angles. Nor are these findings limited to studies in aeolian environments, and it is hoped that consideration of the effect of scanning geometries on point cloud data will be given in any study utilising TLS. The influence of scanning geometry is receiving increasing amounts of attention (Soudarissanane *et al.*, 2011*)*. Kaasalainen *et al.*, (2011) suggest that the influence of incidence angle on scan quality is affected by surface parameters such as roughness or grain size. These parameters are environment specific and this study has studied the effect of incident angles in aeolian environments.

Ideal scan set ups would seek the greatest scan incident angle; however, it is acknowledged this is not always possible when conducting field studies. Therefore, the error to be expected from scanning at less than ideal incidence angles has been quantified. This can then be used to provide confidence levels or error thresholds within the data sets produced, acknowledging the influence of scanning geometry. The fact that different bedforms within the same environments are influenced differently by scanning geometries should be considered by any study utilising TLS. Information regarding the best protocols to follow to capture the object of interest should be explored before a field study is conducted. Using this approach will provide more accurate data and result in greater reliability.

The knowledge gained from studying scan geometries has also been applied to an active aeolian ripple field. Scans when no active saltation was occurring were highly accurate and produced useful topographic data. From this, ripple metrics regarding wavelength and amplitude were extracted and an automated method was developed to do this. It was found that all ripples scanned fell within previously observed morphologic ranges, suggesting that the TLS is a useful tool to capture ripples quickly and accurately. However, this conclusion is hindered by a lack of validation data. Therefore, further work is required to collect independent measurements regarding the features being scanned in order to validate the results obtained in this study.

Undertaking scanning during active saltation was then used to capture the topography of a rippled bed. Ripple migration rates were shown to fall within previously observed rates of migration. Correlation between wind speed and migration rate was low, however this is likely to be a function of the distance between the study site and the meteorological station. Future studies would greatly benefit with the deployment of an in-situ weather station to provide more frequent and accurate local weather data. Short and uniform pauses between subsequent scans would reduce the possibility of ripple aliasing. Deployment of saltation flux instruments would also provide the ability to correlate saltation and ripple migration rates and should be considered for future studies of this type. It is suggested that following the protocol outlined below will produce optimal results.

1. Reduce scan incident angle where possible to increase point density and reduce error;
2. Utilise bed geometry to enhance maximum possible incident angle;
3. Where maximum incidence angle is not possible in the field, consider the bedform of interest before selecting a threshold;
4. Also consider the bedform when selecting scan resolution to reduce the volume of redundant data;
5. Place the TLS either downwind, or perpendicular to the wind direction to reduce interference;
6. Utilise additional instruments to provide data to validate collected results. An in-situ anemometer would allow stronger inferences to be made between shear velocity and aeolian transport. Saltation impact sensors and sand traps would improve the reliability of any volumetric estimation made using the TLS. Utilising stereo-photogrammetry could also improve bedform migration estimates;
7. Consider bedform migration rates, surface area and point density to reduce the time taken to complete each scan. This information should be used to select a suitable time interval between scans to reduce the effect of aliasing;

One of the key aims of this study was to provide a new method for estimating aeolian sand transport, and the morphologic method utilising TLS point data was identified as a possible improvement on the traditional point based sediment traps typically used in aeolian transport studies. The TLS captures the spatial heterogeneity displayed in surface changes that may not be detected by point based methods. Ripples can clearly be seen propagating through scans and morphologic changes were quantified using DEM differencing and a net sediment transport budget was developed. The ripple sediment budget through the study switches from net erosional during periods of intense saltation, to net depositional as saltation activity decreases, supporting the findings of previous studies (Andreotti *et al*., 2006). The sediment budget for individual ripples follows a similar pattern. The use of TLS in this way provides a method to estimate the reptating component of aeolian sediment transport, which is typically ignored or under estimated by traditional sand traps (Wang and Kraus, 1999; Namikas 2003; Ellis *et al.*, 2009a). Application of the TLS alongside other methods for quantifying sand flux should provide a more accurate estimate of overall transport. The TLS also provides a topographic map of the bed under deformation, shows bedform interactions between ripples, has potential to provide data regarding the saltating layer (Nield and Wiggs, 2011) and could be used to provide surface roughness measurements (Kaasalainen *et al*., 2011).

Uncertainty analysis performed on the DODs, removed the majority of the data. Up to 95% of data was excluded when a threshold level of detection was applied, and the difference between the thresholded and un-thresholded volume estimates was large. The absence of validation data limits the reliability of both the thresholded and unthresholded results and further investigation is required in order to validate the results obtained. It may be the case that due to aliasing, the TLS is more suited to capturing larger scale bed changes and roughness metrics rather than ripples on an individual basis. Larger bedforms migrate at slower rates, which would allow the TLS to complete a full scan at a high resolution without the bedform undergoing significant change. The control experiment showed that the TLS is suited to capturing small scale bedforms accurately and this is an aspect worthy of further research. This study has shown that the TLS could prove useful in aeolian environments, especially when a carefully considered scan set up is implemented.

Reference List

Allen, J. R. L. 1969. On the geometry of current ripples in relation to stability of fluid flow, *Geografiska Annaler*, 51, 61-95.

Anderson, R. S. 1987. A theoretical model of aeolian impact ripples, *Sedimentology*, 34, 943-956.

Anderson, R. S. 1990. Eolian ripples as examples of self-organisation in geomorphological systems, *Earth-Science Reviews*, 29, 77-96.

Anderson, R. S. and Bunas, K. L. 1993. Grain size segregation and stratigraphy in aeolian ripples modelled with a cellular automaton, *Nature,* 365, 740-743.

Anderson, R.S. and McDonald, R.R. 1990. Bifurcations and terminations in eolian ripples. *Eos 71*, 1344.

Andreotti, B., Claudin, P. and Douady, S. 2002. Selection of dune shapes and velocities Part 2: A two-dimensional modelling, *The European Physical Journal B*, 28, 3, 341-352.

Andreotti, B., Claudin, P. and Pouliquen, O. 2006. Aeolian Sand Ripples: Experimental Study of Fully Developed States, *Physical Review Letters*, 96, 028001-1-028001-4.

Antonarakis, A.S., Richards, K.S., Brasington, J. and Bithell, M. 2009. Leafless roughness of complex tree morphology using terrestrial lidar, *Water Resources Research*, 45, W10401.

Arens, S.M. 1996. Rates of aeolian transport on a beach in a temperate humid climate, *Geomorphology*, 17, 3-18.

Arens, S.M. 1997. Transport rates and volume changes in a coastal foredune on a Dutch Wadden island, *Journal of Coastal Conservation*, 3, 49-56.

Arens, S. M. and Lee, G. van der. 1995. Saltation sand transport for the measurement of aeolian transport into the foredunes, *Soil Technology*, 8, 61-74.

Baas, A.C.W. 2004. Evaluation of saltation flux impact responders (Safires) for measuring instantaneous aeolian sand transport intensity, *Geomorphology*, 59, 99-118.

Baas, A. C. W. and Sherman, D. J. 2005. Formation and behaviour aeolian streamers, *Journal of Geophysical Research*, 110, F03011.

Baas, A.C.W. and Sherman, D.J. 2006. Spatiotemporal Variability of Aeolian Sand Transport in a Coastal Dune Environment, *Journal of Coastal Research*, 22, 5, 1198-1205.

Baas, A. C. W. 2007. Complex systems in aeolian geomorphology, *Geomorphology*, 91, 311-331.

Baas, A. C. W. 2008. Challenges in aeolian geomorphology: Investigating aeolian streamers, *Geomorphology*, 93, 3-16.

Bagnold, R.A. 1941. The Physics of Blown Sand and Desert Dunes. Chapman and Hall, London.

Bagnold, R.A. 1973. The nature of saltation and 'bed-load' transport in water, *Proceedings of the Royal Society London*, Series A, 332, 473-504.

Barchyn, T.E. and Hugenholtz, C.H. 2010. Field comparison of four piezoelectric sensors for detecting aeolian sediment transport, *Geomorphology*, 120, 368-371.

Bauer, B. O. and Davidson-Arnott, R. G. D. 2002. A general framework for modelling sediment supply to coastal dunes including wind angle, beach geometry, and fetch effects, *Geomorphology*, 49, 89-108.

Bauer, B.O. and Namikas, S.L. 1998. Design and field test of a continuously weighing, tipping-bucket assembly for aeolian sand traps, *Earth Surface Processes and Landforms*, 23, 1171-1183.

Bauer, B. O., Sherman, D.J., Nordstrom, K.F. and Gares, P. A. 1990. Aeolian transport and measurement across a beach and dune at Castroville, California. In Carter, R. W. G., Nordstrom, K. F. and Psuty, N.P. (eds) *Coastal Dunes: Form and Process*, John Wiley and Sons, London, 39-55.

Behan, A. 2000. On the Matching Accuracy of Rasterised Scanning Laser Altimeter Data, *International Archives of Photgrammetry and Remote Sensing*, 33, B2, 75-82.

Boehler, W. and Marbs, A. 2005. Investigating Laser Scanner Accuracy, http://www.scanning.fh-mainz.de/scannertest/results300305.pdf (accessed 27.08.2010)

Borah, D.K. and Voelz D.G. 2007. Estimation of Laser beam pointing prarmeters in the presence of atmospheric turbulence, *Applied Optics*, 46, 23, 6010-6018.

Bouchard, J. P., Cates, M. E., Ravi Prakesh, J. and Edwards, S. F. 1994. A model for the dynamics of sandpile surfaces, *Journal de Physique I*, 4, 10, 1383-1410.

Brasington, J., Rumsby, B.T. and McVey, R.A. 2000. Monitoring and modelling morphological change in a braided gravel-bed river using high resolution GPS-based survey, *Earth Surface Processes and Landforms*, 25, 973-990.

Brasington, J., Langham, J. and Rumsby, B. 2003. Methodological sensitivity of morphometric estimates of coarse fluvial sediment transport, *Geomorphology*, 53, 3, 229-316.

Brasington, J. and Smart, R.M.A. 2003. Close range digital photogrammetric analysis of experimental drainage basin evolution, *Earth Surface Processes and Landforms*, 28, 231-247.

Brasington, J., Wheaton, J.M. and Hodge, R. 2007. Modelling braided river morphodynamics with terrestrial laser scanning, *EOS Transactions* AGU, 88, Fall Meet. Suppl., Abstract H51L-02.

Bullard, J.E. 2006. Arid Geomorphology, *Progress in Physical Geography*, 30, 542-552.

Butterfield, G. R. 1991. Grain transport rates in steady and unsteady turbulent airflows, *Acta Mechanica Supplement*, 1, 97-122.

Butterfield, G.R. 1998. Transitional behaviour of saltation: wind tunnel observations of unsteady winds, *Journal of Arid Environments*, 39, 377-394.

Carbonneau, P.E., Lane, S.N. and Bergeron, N.E. 2003. Cost-effective non-metric close-range digital photogrammetry and its application to a study of coarse gravel river beds, *International Journal of Remote Sensing*, 24, 14, 2837-2854.

Chapman, D.M. 1990. Aeolian sand transport – an optimized model, *Earth Surface Processes and Landforms*, 15, 751-760.

Charlton, M.E., Large, A.R.G. and Fuller, I.C. 2003. Application of airborne LiDAR in river environments: the River Coquet, Northumberland, UK, *Earth Surface Processes and Landforms*, 28, 299-306.

Clark, J. and Robson, S. 2004. Accuracy of measurments made with a Cyraz 2500 laser scanner against surfaces of known colour, *Survey Review*, 37, 294, 626-638.

Clawges, R., Vierling, L.A. and Calhoon, M. 2007. Use of ground-based scanning LiDAR for estimation of biophyscil properties of western larch (*Larix occidentalis*), *International Journal of Remote Sensing*, 28, 19, 4331-4344.

Coco, G and Murray, A. B. 2007. Patterns in the sand: from forcing templates to self-organisation, *Geomorphology*, 91, 271-290.

Cornish, V. 1933. *Ocean waves and kindred geophysical phenomena*, Cambridge Uniersity Press, Cambridge.

Csahòk, Z., Misbah, C., Rioual, F. and Valance, A. 2000. Dynamics of aeolian ripples, *The European Physical Journal E*, 3, 71-86.

Davidson-Arnott, Yang, Y., Ollerhead, J., Hesp, P.A. and Walker, I. J. 2008. The effect of surface moisture on aeolian sediment transport threshold and mass flux on a beach, *Earth Surface Processes and Landforms*, 33, 55-74.

Eitel, J.U.H., Vierling, L.A. and Long, D.S. 2010. Simultaneous measurements of plant structure and chlorophyll content in broadleaf saplings with a terrestrial laser scanner, *Remote Sensing of Environment*, 114, 2229-2237.

Eitel, J.U.H., Willians, C.J., Vierling, L.A., Al-Hamdean, O.Z. and Pierson, F.B. 2011. Suitability of terrestrial laser scanning for studying surface roughness effects on concentrated flow erosion processes in rangelands, *Catena*, 87, 3, 398-407.

Ellis, J.T., Li, B., Farrell, E.J. and Sherman, D. J. 2009a. Protocols for characterizing aeolian mass-flux profiles, *Aeolian Research*, 1, 1-2, 19-26.

Ellis, J.T., Morrison, R.F. and Priest, B.H. 2009b. Detecting impacts of sand grains with a microphone system in field conditions, *Geomorphology*, 105, 87-94.

Ellwood, J. M., Evans, P. D. and Wilson, I. G. 1975. Small scale aeolian bedforms, *Jourrnal of Sedimentary Petrology*, 45, 554-561.

Ewing, R.C., Kocurek, G. and Lake, L.W. 2006. Pattern analysis of dune-field parameters, *Earth Surface Processes and Landforms*, 31, 1176-1191.

Ewing, R.C. and Kocurek, G. 2010. Aeolian dune-field pattern boundary conditions, *Geomorphology*, 114, 175-187.

French, J.R. 2003. Airborne LiDAR in support of geomorphic and hydraulic modelling, *Earth Surface Processes and Landforms*, 28, 321-335.

Fryberger, S. G., Hesp, P. and Hastings, K. 1992. Aeolian granule ripple deposits, Namibia, *Sedimentology*, 39, 319-331.

Fuller, I.C., Large, A.R.G., Charlton, M.E., Heritage, G.L. and Milan, D.J. 2003. Reach-scale sediment transfers: An evaluation of two morphological budgeting approaches, *Earth Surface Processes and Landforms*, 28, 8, 889-903.

Gares, P.A., Davidson-Arnott, R.G.D., Bauer, B.O., Sherman, D.J., Carter, R.W.G., Jackson, D.W.T. and Nordstrom, K.F. 1996. Alongshore variations in aeolian sediment transport: Carrick Finn Strand, Ireland, *Journal of Coastal Research*, 12, 673-682.

Gartman, A., Fister, W., Schwanghart, W. and Müller, M.D. 2011. CFD modelling and validation of measured wind field data in a portable wind tunnel, *Aeolian Research*, 3, 315-325.

Geist, H.J. and Lambin, E.F. 2004. Dynamic Causal Patterns of Desertification, *BioScience,* 54, 9, 817-829.

Gillette, D. A. 1999. Physics of Aeolian Movement Emphasising Changing of the Aerodynamic Roughness Height by Saltating Grains (the Owen Effect), in Goudie, A. S., Livingstone, I. and Stokes, S. (eds), *Aeolian Environments, Sediments and Landforms,* Wiley, Chichester.

Gillette, D.A., Fryrear, D.W., Xiao, J.B., Stockton, P.H., Ono, D., Helm, P.J., Gill, T.E. and Ley, T. 1997. Large-scale variability of wind erosion mass flux rates at Owens Lake: 1. Vertical profiles of horizontal mass fluxes of wind-eroded particles with diameter greater than 50 μm, *Journal of Geophysical Research*, 102, 25977– 25987.

Greeley, R. and Iverson, J. D. 1985. *Wind as a Geological Process*, Cambridge University Press, Cambridge.

Greeley, R., Blumberg, D.G. and Williams, S. H. 1996. Field measurements of the flux and speed of wind-blown sand, *Sedimentology*, 43, 41-52.

Gruen, A. and Akca, D. 2005. Least squares 3D surface and curve matching, *ISPRS Journal of Photogrammetry and Remote Sensing*, 59, 3, 151-174.

Goosens, D. 2004. Effect of soil crusting on the emission and transport of wind-eroded sediment: field measurements on loamy sandy soil, *Geomorphology,* 58, 145-160.

Haff, P.K. 1996. Limitations on predictive modelling in geomorphology. In Rhoads, B.L. and Thorn, C.E. (eds), The Scientific Nature of

Geomorphology: Proceedings of the 27th Binghamton Symposium in Geomorphology, Wiley, Chichester, 337-358.

Hallet, B. 1990. Spatial self-organisation in geomorphology: from periodic bedforms and patterned ground to scale-invariant topography, *Earth-Science Reviews*, 29, 57-75.

Hancock, G.R. and Wilgoose, G.R. 2001. The interaction between hydrology and geomorphology in a landscape simulatpr experiment, *Hydrological Processes*, 15, 115-133.

Hardisty, J. and Whitehouse, K. J. S. 1988. Evidence for a new sand transport process from experiments on Saharan dunes, *Nature*, 332, 532-534.

Heritage, G. and Hetherington, D. 2007. Towards a protocol for laser scanning in fluvial geomorphology, *Earth Surface Processes and Landforms*, 32, 1, 66-74.

Heritage, G. and Large, A.R.G (eds). 2009. *Laser Scanning for the Environmental Sciences*. Wiley, Chichester.

Heritage, G.L., Milan, D.J., Large, A.R.G. and Fuller, I.C. 2009. Influence of survey strategy and interpolation model on DEM quality, *Geomorphology*, 112, 334-344.

Hodge, R., Brasington, J. and Richards, K. 2009a. *In situ* characterization of grain-scale fluvial morphology using Terrestril Laser Scanning, *Earth Surface Processes and Landforms*, 34, 954-968.

Hodge, R., Brasington, J. and Richards, K. 2009b. Analysing laser-scanned digital terrain models of gravel bed surfaces: linking morphology to sediment transport processes and hydraulics, *Sedimentology*, 56, 2024-2043.

Hodge, R. 2010. Using simulated Terrestrial Laser Scanning to analyse errors in high-resolution scan data of irregular surface, *ISPRS Journal of Photogrammetry and Remote Sensing*, 65, 2, 227-240.

Horikawa, K., Hotta, S., Kubota, S. and Katori, S. 1984. Field measurement of blown sand transport rate by trench trap, *Coastal Engineering Journal. Japan*, 26, 101-120.

Houser, C. 2009. Synchronisation of transport and supply in beach-dune interaction, *Progress in Physical Geography*, 33, 6, 733-746.

Hoyle, R. B. and Mehta, A. 1999. Two-Species Continuum Model for Aeolian Sand Ripples, *Physical Review Letters*, 83, 5170-5173.

Hoyle, R. B. and Woods, A. W. 1997. Analytical model of propagating sand ripples, *Physical Review E*, 56, 6, 6861-6868.

Hsu, S.A. 1973. Computing eolian sand transport from shear velocity measurements, *Journal of Geology*, 81, 739-743.

Illenberger, W.K. and Rust, I.C. 1986. Venturi-compensated eolian sand trap for field use, *Journal of Sedimentary Research*, 56, 4, 541-543.

Iverson, J.D. and Rasmussen, K.R. 1994. The effect of surface slope on saltation threshold, *Sedimentology*, 41, 721-728.

Jackson, D. W. T. 1996a. Potential inertial effects in aeolian sand transport: preliminary results, *Sedimentary Geology*, 106, 193-201.

Jackson, D. W. T. 1996b. A new, instantaneous sand trap design for field use, *Sedimentology*, 43, 791-796.

Jackson, N.L., Sherman, D.J., Hesp, P.A., Klein, A.H.F., Ballasteros, F. and Nordstrom, K.F. 2006. Small-Scale Spatial Variations in Aeolian

Sediment Transport on a Fine-Sand Beach, *Journal of Coastal Research*, SI39, 379-383.

Jerolmack, D. J. and Mohrig D. 2005. Interactions between bed forms: Topography, turbulence, and transport, *Journal of Geophysical Research*, 110, F02014.

Jones, J.R. and Willets, B.B. 1979. Errors in measuring uniform aeolian sand flow by means of an adjustable trap, *Sedimentology*, 26, 463-468.

Kaasalainen, S., Ahokas, E., Hyypp, J. and Suomalainen, J. 2005. Study of surface brightness from backscattered laser intensity calibration of laser data, IEEE Geoscience and Remote Sensing Letters, 2, 3, 255-259.

Kaasalainen, S., Jaakkola, A., Kaasalainen, M., Krroks, A. and Kukko, A. 2011. Analysis of Incidence Angle and Distance Effects on Terrerstrial Laser Scanner Intensity: Search for Correction Methods, *Remote Sensing*, 3, 2207-2221.

Kadib, A.A. 1965. A function for sand movement by wind, *University of California Hydraulics Engineering Laboratory Report HEL*, 2-8, Berkeley.

Kawamura, R. 1951. Study of sand movement by wind, *Institute of Science and Technology*, *Tokyo*, Report 5, 3-4, 95-112.

Keightly, K. E. and Bawden, G. W. 2010. 3D volumetric modelling of grapevine biomass using Tripod LiDAR, *Computers and Electronics in Agriculture*, 74, 305-312.

Khalaf, F.I. and Al-Ajmi, D. 1993. Aeolian Processes and sand Encroachment Problems in Kuwait, *Journal of Geomorphology*, 6, 111-134.

Kocurek, G., Ewing, R. C. and Mohrig, D. 2010. How do bedform patterns arise? New views on the role of bedform interactions within a set of boundary conditions, *Earth Surface Processes and Landforms*, 35, 1, 51-63.

Kocurek, G., Townsley, M., Yeh, E., Havholm, K. and Sweet, M.L. 1992. Dune and dune-field development on Padre Island, Texas, with implications for interdune deposition and water-table-controlled accumulation, *Journal of Sedimentary Petrology*, 62, 4, 622-635.

Kukko, A., Kaasalainen, S. and Litkey, P. 2008. Effect of incidence angle on laser scanner intensity and surface data, *Appl. Opt.*, 47, 986 2008.

Lancaster, N. 1982. Dunes on the Skeleton Coast, SWA/Namibia: geomorphology and grain size relationships, *Earth Surface Processes and Landforms*, 7, 57-587.

Lancaster, N. 1995. *Geomorphology of Desert Dunes*. Routledge, London.

Lancaster, N. 1996. Field studies of sand patch initiation on the northern margin of the Namib sand sea, *Earth Surface Processes and Landforms*, 21, 947-954.

Landry, W. and Werner, B. T. 1994. Computer-simulations of self-organised wind ripple patterns, *Physica D*, 77, 238-260.

Lane, S.N., Chandler, J.H. and Richards, K.S. 1994. Developments in monitoring and modelling small-scale river bed topography. *Earth Surface Processes and Landforms*, 19, 4, 349-368.

Lane, S.N. and Chandler, J.H. 2003. Editorial: The generation of high quality topographic data for hydrology and geomorphology: New data sources, new applications and new problems, *Earth Surface Processes and Landforms*, 28, 229-230.

Lane, S.N. Richards, K.S. and Chandler, J.H. 1995. Morphological estimation of the time-integrated bed load transport rate, *Water Resources Research*, 31, 3, 761-772.

Lane, S.N., Westaway, R.M. and Hicks, M. 2003. Estimation of erosion and deposition volumes in large, gravel-bed, braided river using synoptic remote sensing, *Earth Surface Processes and Landforms*, 28, 249-271.

Large, A.R.G. and Heritage, G.L. 2009. Laser Scanning- Evolution of the Discipline. In Heritage, G.L. and Large, A.R.G. (eds) *Laser Scanning for the Environmental Sciences*, Wiley-Blackwell, Chichester.

Leatherman, S.P. 1978. A new aeolian sand trap design, *Sedimentology*, 25, 303-306.

Lee, J.A. 1987. A field experiment on the role of small scale wind gustiness in aeolian sand transport, *Earth Surface Processes and Landforms*, 12, 331-335.

Leica Geosystems. 2007. http://hds.leica-geosystems.com/hds/en/Leica_HDS3000.pdf (accessed 27.08.10)

Lettau, K. and Lettau, H. 1977. Experimental and micrometerological field studies of dune migration. In Lettau, K. and Lettau, H (eds), *Exploring the Worlds Driest Climate*, 110-147, University of Wisconsin, Madison, Institute for Environmental Studies.

Li, Z.S. and Ni, J.R. 2003. Sampling efficiency of vertical array aeolian sand traps, *Geomorphology*, 52, 3, 243-252.

Lichti, D.D. 2005. Spectral Filtering and Classification of Terrestrial Laser Scanner Point Clouds, *The Photogrammetric Record*, 20, 111, 218-240.

Lichti, D.D., Gordon, S.J. and Tipdecho, T. 2005. Error models and propagation in directly georeferenced terrestrial laser scanner networks, *Journal of Surveying Engineering*, 131, 4, 135-142.

Lichti, D.D. and Jamtsho, S. 2006. Angular resolution of terrestrial laser scanners, *The Photogrammetric Record*, 21, 114, 141-160.

Lichti, D.D. 2007. Error modelling, calibration and analysis of an AM-CW terrestrial laser scanner system, *Journal of Photogrammetry & Remote Sensing*, 61, 307-324.

Lim, M., Petley, D.N., Rosser, N.J., Allison, R.J., Long, A.J. and Pybus, D. 2006. Combined digital photogrammetry and time-of-flight laser scanning for monitoring cliff evolution, *Photogrammetric record*, 20, 1, 109-129.

Lim, M., Mills, J. and Rosser, N. 2009. Laser Scanning Surveying of Linear Features: Considerations and Applications. In Heritage, G.L. and Large, A.R.G. (eds) *Laser Scanning for the Environmental Sciences*, Wiley-Blackwell, Chichester.

Lim, M., Rosser, N.J., Allison, R.J. and Petley, D.N. 2010. Erosional processes in the hard rock coastal cliffs at Staithes, North Yorkshire, *Geomorphology*, 114, 12-21.

Lindenbergh, R., Pfeifer, N. and Rabbani, T. 2005. Accuracy analysis of the Leica HDS3000 and feasibility of tunnel deformation monitoring, Proceedings of the ISPRS Workship Laser Scanning, Volume XXXXVI, Netherlands, 24-29.

Liu, X., Dong, Z., Wang, X. 2006. Wind tunnel modelling and measurements of the flux of wind-blown sand, *Journal of Arid Environments*, 66, 657-672.

Lorenz, R.D. 2011. Observations of wind ripple migration on an Egyptian seif dune using an inexpensive digital timelapse camera, *Aeolian Research*, 3,2, 229-234.

Lorenz, R.D. and Valdez, A. 2011. Variable wind ripple migration at Great Sand Dunes National Park and Preserve, observed by timelapse imaging, *Geomorphology*, 133, 1-10.

Lorenz, R.D, Jackson, B. and Barnes, J. 2010. Inexpensive timelapse digital cameras for studying transient meterorological phenomena: dust devils and playa flooding, *Journal of Atmospheric and Oceanic Technology*, 27, 246-256.

Manukyan, E. and Prigozhin, L. 2009. Formation of aeolian ripples and sand sorting, *Physical Review E*, 79, 031303.

Marcus, W.A. and Fonstad, M.A. 2008. Optical remote mapping of rivers at sub-meter resolutions and watershed extents, *Earth Surface Processes and Landforms*, 33, 4-24.

Martin, Y. 2003. Evaluation of bed load transport formulae using field evidence from the Vedder River, British Columbia, *Geomorphology*, 53, 75-95.

Martin, Y. and Church, M. 1995. Bed-material transport estimated from channel surveys: Vedder River, British Columbia, *Earth Surface Processes and Landforms*, 20, 336-347.

McEwan, I.K. and Willets, B.B. 1991. Numerical model of the saltation cloud, *Acta Mechanica Supplement*, 1, 53-66.

McEwan,I. K. and Willets, B.B. 1993. Sand transport by wind: a review of the current conceptual model, in Pye, K. (ed) *The Dynamics and Environmental Context of Aeolian Sedimentary Systems*, Geological Society, London.

McEwan,I. K. and Willets, B.B. 1994. On the prediction of bed-load sand transport rate in air, *Sedimentology*, 41, 1241-1251.

McKenna-Neuman, C. 1993. A review of aeolian transport processes in cold environments, *Progress in Physical Geography*, 17, 2, 137-155.

McKenna-Neuman, C. and Nickling, W.G. 1989. A theoretical and wind tunnel investigation of the effect of sediment by wind, *Canadian Journal of Soil Science*, 69, 79-96.

McMenamin, R., Cassidy, R. and McCloskey, J. 2002. Self-Organised Criticality at the onset of Aeolian Sediment Transport, *Journal of Coastal Research*, SI36, 498-505.

Mechelke, K., Kersten, T.P. and Lindstaedt, M. 2007. Comparative investigations into the accuracy behaviour of the new generation terrestrial laser scanning systems, *Optical 3-D Measurement Techniques VIII, 1, 319-327.*

Miao, T.D., Mu, Q.S. and Wu, S.Z. 2001. Computer simulation of aeolian sand ripples and dunes, *Physics Letters A*, 288, 16-22.

Milan, D.J., Heritage, G.L. and Hetherington, D. 2007. Application of a 3D laser scanner in the assessment of erosion and deposition volumes and channel change in a proglacial river, *Earth Surface Processes and Landforms,* 32, 1657-1674.

Milne, D.J. and Sear, D. 1997. Modelling river channel topography using GIS. *International Journal of Geographical Information Science*. 11, 5, 499-519.

Misbah, C. and Valance, A. 2003. Sand ripple dynamics in the case of out-of-equilibrium aeolian regimes, *The European Physical Journal E*, 12, 4, 523-529.

Mitha, S., Tran, M. Q., Werner, B. T. and Haff, P. K. 1986. The grain-bed impact process in aeolian saltation, *Acta Mechanica*, 63, 267-278.

Momiji, H., Nishimori, H., and Bishop, S.R. 2002. On the shape and migration speed of a proto-dune, *Earth Surface Processes and Landforms*, 27, 1335-1338.

Nagihara, S., Mulligan, K.R. and Xiong, W. 2004. Use of a three-dimensional laser scanner to digitally capture the topography of sand dunes in high spatial resolution, *Earth Surface Processes and Landforms*, 29, 391-398.

Namikas, S. L. 2003. Field measurement and numerical modelling of aeolian mass flux distribution on a sandy beach, *Sedimentology*, 50, 303-326.

Namikas, S.L., Edwards, B.L., Bitton, M.C.A., Booth, J.L. and Zhu, Y. 2010. Temporal and spatial variabilities in the surface moisture content of a fine grained beach, *Geomorphology*, 114, 303-310.

Namikas, S.L. and Sherman, D.J. 1995. A review of the effects of surface moisture content on aeolian sand transport. In Tchakerian, V.P. (ed), Desert Aeolian Processes, Chapman and Hall, New York.

Nickling, W. G. 1988. The initiation of partical movement by wind. *Sedimentology*, 35, 499-511.

Nickling, W.G. and Mckenna Neuman, C. 1997. Wind tunnel evaluation of a wedge-shaped aeolian sediment trap, *Geomorphology*, 18, 333-345.

Niedzielski, T., Kowalcyzyk, K. and Czystolowski, M. 2006. Statistical procedure to analyse sparse data on the morphometric parameters of aeolian sand ripples obtained by the shadow cast technique, *Estuarine, Coastal Shelf Science*, 70, 180-186.

Nield, J. M. and Baas, A. C. W. 2008. Investigating parabolic and nebkha dune formation using a cellular automaton modelling approach, *Earth Surface Processes and Landforms*, 33, 724-740.

Nield, J.M., Wiggs, G.F.S. and Squirrell, R.S. 2011. Aeolian sand strip mobility and protodune development on a drying beach: examining surface moisture and surface roughness patterns measured by terrestrial laser scanning. *Earth Surface Processes and Landforms*, 36, 4, 513-522.

Nield, J. M. and Wiggs, G.F.S. 2011. The application of terrestrial laser scanning to aeolian saltation cloud measurement and its response to changing surface moisture. *Earth Surface Process and Landforms*, 36, 273-278.

Nittrouer, J.A., Allison, M.A. and Campanella, R. 2008. Bedform transport rates for the lowermost Mississippi River, *Journal of Geophysical Research*, 113, F03004.

Nordstrom, K.F. and Jackson, N.L. 1992. Effect of source width and tidal elevation changes on eolian transport on an estuarine beach, *Sedimentology*, 39, 769-778.

Norris, R. M. and Norris, K. S. 1961. Algodones Dunes of southeastern California, *Geological Society of America Bulletin*, 72, 605-620.

Ochoa, R.D. 2005. *Repeated high-precision topographic surveys of a barchan dune at White Sands, New Mexico using ground-based lidar*, MA Thesis, Texas Tech University.

Olsen, M.J. and Stuedlein, A.W. 2010. Discussion of 'Use of terrestrial laser scanning for the characterisation of retrogressive landslides in sensitive clay and rotational landslides in river banks', *Candadian Geotechnical Journal,* 46, 12, 1379-1390.

Owen, P. R. 1964. Saltation of uniform grains in air, *Journal of Fluid Mechanics,* 20, 225-242.

Pelletier, J.D. 2009. Controls on the height and spacing of eolian ripples and transverse dunes: A numerical modelling investigation, *Geomorphology*, 105, 322-333.

Pesci, A., Fabris, M., Conforti, D., Loddo, F., Baldi, P. and Anzidei, M. 2007. Integration of ground-based laser scanner and aerial digital photogrammetry for topographic modelling of Vesuvio volcano, *Journal of Volcanology and Geothermal Research*, 162, 3-4, 123-138.

Pesci, A. and Teza, G. 2008. Effects of surface irregularities on intensity data from laser scanning: an experimental approach, *Annals of Geophysics*, 51, 839-848.

Pfeifer, N., Dorninger, P., Haring, P. and Fan, H. 2007. Investigating Terrestrial Laser Scanning Intensity Data: Quality and Functional Relations, In 8th conf. on O3D, Zurich, Switzerland

Pieraccini, M., Noferini, L., Mecatti, D., Atzeni, C., Teza G., Galgaro, A. and Zaltron, N. *2006*. Integration of radar interferometry and laser scanning for remote monitoring of an urban site built on a sliding slope, *IEEE Transactions on Geoscience and Remote Sensing*, 44, 9, 2335-2342.

Pietro, L.S., O'Neal, M.A. and Puleo, J.A. Developing Terrestrial-LIDAR-Based Digital Elevation Models for Monitoring Beach Nourishment Performance, *Journal of Coastal Research*, 24, 6, 1555-1564.

Prigozhin, L. 1999. Nonlinear dynamics of Aeolian sand ripples, *Physical Review E*, 60, 729-733.

Puccia, C. J. and Levins, R. 1985. *Qualitative Modeling of Complex Systems (an introduction to loop analysis and time averaging*), Harvard University Press, Cambridge, Massachusetts.

Pye, K. 1987. *Aeolian dust and dust deposits,* Academic Press, London.

Rasmussen, K. R. and Mikkelsen, H. E. 1991. Wind tunnel observation of aeolian transport rates, *Acta Mechanica Supplement*, 1, 135-144.

Rosser, N.J., Petley, D.N., Lim, M., Dunning, S.A. and Allison, R.J. 2005. Terrestrial laser scanning for monitoring the process of hard rock coastal cliff erosion, *Quarterly Journal of Engineering Geology and Hydrogeology*, 38, 4, 363-375.

Pye, K. and Tsoar, H. 1990. *Aeolian Sand and Sand Dunes*, Unwin Hyman, London.

Rasmussen, K. R. and Sorensen, M. 2008. Vertical variation of particle speed and flux density in aeolian saltation: Measurement and modelling, *Journal of Geophysical Research*, 113, F02S12.

Reshetyuk, Y. 2010. A unified approach to self-calibration of terrestrial laser scanners, *Journal of Photogrammetry and Remote Sensing*, 65, 445-456.

Rumpel, D. A. 1985. Successive aeolian saltation: studies of idealized collisions, *Sedimentology,* 32, 267-275.

Ruz, M-H. and Meur-Ferec, C. 2004. Influence of high water levels on aeolian sand transport: upper beach/dune evolution on a macrotidal coast, Wissant Bay, northern France, *Geomorphology*, 60, 73-87.

Sankey, J.B., Eitel, J.U.H., Glenn, N.F., Germino, M.J. and Vierling, L.A. 2011. Quantifying relationships of burning, roughness, and potential dust emission with laser altimetry of soil surfaces at submeter scales, *Geomorphology*, 135, 181-190.

Sauerman, G., Kroy, K. and Herrmann, H. J. 2001. Continuum saltation model for sand dunes, Physical Review E, 64, 31305.

Saye, S.E., Wal, D.v.d. and Pye, K. 2005. Beach-dune morphological relationships and erosion/accretion: An investigation at five sites in England and Wales using LIDAR data, *Geomorphology*, 72, 128-155.

Schürch, P., Densmore, A.L., Rosser, N.J., Lim, M. and McArdell, W.B. 2011. Detection of surface change in complex topography using terrestrial laser scanning: application to the Illgraben debris-flow channel, *Earth Surface Processes and Landforms*, 36, 1847-1859.

Sepalla, M. and Linde, K. 1978. Wind tunnel studies of ripple formation, *Geografiska Annaler*, 60, 29-42

Shao, Y. and Lu, H. 2000. A simple expression for wind erosion threshold friction velocity, *Journal of Geophysical Research*, 105, 22437-22443.

Sharp, R. P. 1963. Wind Ripples, *Journal of Geology*, 71, 617-636.

Sherman, D.J. 1995. Problems of scale in the modelling and interpretation of coastal dunes, *Marine Geology*, 124, 339-349.

Shermann, D. J. and Hotta, S. 1990. Aeolian sediment transport: theory and measurement. In Carter, R. W. G., Nordstrom, K. F. and Psuty, N.P. (eds) *Coastal Dunes: Form and Process*, John Wiley and Sons, London, 17-37.

Sherman, D. J., Jackson, D.W.T., Namikas, S.L. and Wang, J. 1998. Wind-blown sand on beaches: an evaluation of models, *Geomorphology*, 22, 113-133.

Sherman, D. J. and Farrell, E. J. 2008. Aerodynamic roughness lengths over movable beds: Comparison of wind tunnel and field data, *Journal of Geophysical Research*, 113, F02S08.

Soudarissanane, S., Van Ree, J., Bucksch, A. and Lindenbergh, R. 2007. Error budget of Terrestrial Laser Scanning: Influence of the incidence angle on the scan quality, In Proceedings of 3D-NordOst, Berlin, Germany, December 5- December 8, 2007.

Soudarissanane, S., Lindenbergh, R., Menenti, M. and Teunissen, P. 2009. Incidence Angle Influence on the Quality of Terrestrial Laser Scanning Points, ISPRS Workshop Laserscanning 2009, Paris.

Soudarissanane, S., Lindenbergh, R., Menenti, M. and Teunissen, P. 2011. Scanning geometry: Influencing factor on the quality of terrestrial laser scanning points, *ISPRS Journal of Photogrammetry and Remote Sensing*.

Spaan, W.P. and Van den Abele, G.D. 1991. Wind borne particle measurements with acoustic sensors, *Soil Technology*, 4, 51-63.

Spies, P. J., McEwan, I. K. and Butterfield, G. R. 2000. One-Dimensional transitional behaviour in saltation, *Earth Surface Processes and Landforms*, 25, 505-518.

Sterk, G., Jacobs, A.F.G. and Van Boxel, J.H. 1998. The effect of turbulent flow structures on saltation sand transport in the atmospheric boundary layer, *Earth surface Processes and Landforms*, 23, 10, 877-887.

Sterk, G., Lopez, M.V. and Arrue, J.L. 1999. Saltation transport on a silt loam soil in northeast Spain, *Land Degradation & Development*, 10, 545-554.

Stockton, P.H. and Gillete, G.A. 1990. Field measurement of the sheltering effect of vegetation on erodible land surface, *Land Degradation & Rehabilitation*, 2, 77-85.

Stojic, M., Chandler, J., Ashmore, P. and Luce, J. 1998. The assessment of sediment transport rates by automated digital photogrammetry, *Photogrammetric Engineering & Remote Sensing*, 64, 5, 387-395.

Stull, R. B. 1988. *An Introduction to Boundary Layer Meterology*, Dordrecht, Kluwer.

Szornik, K.W., Gehrels, R. and Murray, A.S. 2008. Aeolian sand movement and relative sea-level rise in Ho Bugt, western Denmark, during the ‘Little Ice Age’, *The Holocene*, 18, 6, 951-965.

Terzidis, O., Claudin, P. and Bouchard, J. P. 1998. A model for ripple instabilities in granular media, *The European Physical Journal B*, 5, 2, 245-249.

Thomas, S.G. 2005. Dryland Processes and Environments, in Holden, J. 2005, *Physical Geography and the Environment*, Pearson Prentice Hall, London, 382-404.

UNEP. 1997. *World Atlas of Desertification.* Edward Arnold: London.

Ungar, J.E. and Haff, P.K. 1988. Steady state saltation in air, *Sedimentology*, 34, 289-299.

Valance, A. and Rioual, F. 1999. A nonlinear model for aeolian sand ripples, *European Physical Journal B*, 10, 30, 543-548.

Vandewalle, N. and Galam, S. 2000. A 1DIsing model for ripple formation, *Journal of Physics A*, 33, 4955-4962.

Van Dijk, P. M., Arens, S. M. and Van Boxel, J. H. 1999. Aeolian processes across transverse dunes. II: Modelling the sediment transport and profile development, *Earth Surface Processes and Landforms*, 24, 319-333.

Van Pelt, R.S., Peters, P. and Visser, S. 2009. Laboratory wind tunnel testing of three commonly used saltation impact sensors, *Aeolian Research*, 1, 55-62.

Voison, S., Foufou, S., Truchetet, F., Page, D. and Abidi, M. 2007. Study of ambient light influence for three-dimensional scanners based on structured light, *Optical Engineering*, 46, 3, 030502.

Walker, I.J., Hesp, P.A., Davidson-Arnott, R.G.D. and Ollerhead, J. 2006. Topographic steering of alongshore airflow over a vegetated foredune: Greenwich Dunes, Prince Edward Island, Canada, *Journal of Coastal Research*, 22, 5, 1278-1291.

Wang, C.K., Wu, F.C. Huang, G.H. and Lee, C.Y. 2011. Mesoscale terrestrial laser scanning of fluvial gravel surfaces, *Geosciences and Remote Sensing Letters*,

Wang, P. and Kraus, N.C. 1999. Horizontal water trap for measurement of aeolian sand transport, *Earth Surface Processes and Landforms*, 24, 65-70.

Wang, Y., Wang, D., Wang, L. and Zhang, Y. 2009. Measurement of sand creep on a flat sand bed using a high-speed digital camera, *Sedimentology*, 56, 1705-1712.

Watson, A. 1986. Grain-size variations on a longitudinal dune and a barchans dune, *Sedimentary Geology*, 46, 49-66.

Wechsler, S.P. and Kroll, C.N. 2006. Quantifying DEM uncertainty and its effect on topographic parameters, *Photogrammetric Engineering and Remote Sensing*, 72, 9, 1081-1090.

Werner, B. T. 1995. Eolian dunes: computer simulation and attractor interpretation, *Geology*, 23, 1107-1110.

Werner, B. T. and Gillespie D. T. 1993. Fundamentally discrete stochastic model for wind ripple dynamics, *Physical Review Letters*, 71, 19, 3230-3234.

Werner, B. T. and Haff, P. K.1988. The impact process in aeolian saltation: two-dimensional simulations, *Sedimentology*, 35, 189-196

Werner, B. T., Haff, P. K., Livi, R. P. and Anderson, R. S. 1986. Measurement of eolian sand ripple cross-sectional shapes, *Geology*, 14, 743-745.

Wheaton, J.M. 2008. Uncertainty in morphological sediment budgeting of rivers. Unpublished PhD Thesis, University of Southampton, 412pp. http://www.joewheaton.org/Home/research/projects-1/morphological-sediment-budgeting/phdthesis (accessed 27/11/09)

Wheaton, J.M., Brasington, J., Darby, S.E. and Sear, D.A. 2010. Accounting for uncertainty in DEMs from repeat topographic surveys: improved sediment budgets, *Earth Surface Processes and Landforms*, 35, 2, 135-156.

White, B. R. 1979. Soil transport by winds on Mars, *Journal of Geophysical Research*, 84, 4643-4651.

Willets, B. B. and Rice, M. A. 1986. Collision in aeolian transport: the saltation/creep link. In Nickling, W.G. (Ed), Aeolian Geomorphology, Allen & Unwin, London.

Wilson, I. G. 1972. Aeolian bedforms – their development and origins, *Sedimentology*, 19, 173-210.

Woolard, J.W. and Colby, J.D. 2002. Spatial characterization, resolution, and volumetric change of coastal dunes using airborne LIDAR: Cape Hatteras, North Carolina, *Geomorphology*, 48, 269-287.

Wyngaard, J.C. 1992. Atmospheric turbulence, *Annual Review of Fluvial Mechanics*, 24, 205-234.

Yao, Z.Y., Wang, T., Han, Z.W., Zhang, W.M. and Zhao, A.G. 2007. Migration of sand dunes on the northern Alxa Plateau, Inner Mongolia, China, *Journal of Arid Environments*, 70, 80-93.

Yizhaq, H.Balmforth, N.J. and Provenzale, A. 2004. Blown by wind: nonlinear dynamics of aeolian sand ripples, *Physica D*, 195, 207-228.

Zhang, Q.H. and Miao, T.D. 2003. Aeolian sand ripples aroud plants, *Physical Review E*, 67, 051304-1-4

Zhuang, H. and Roth, Z.S. 1995. Modeling gimbal axis misalignments and mirror centre offset in a single-beam laser tracking measurement system, *The international Journal of Robotics Research*, 14, 3, 211-224.

Zimbleman, J.R., Irwin, R.P., Williams, S.H., Bunch, F., Valdez, A. and Stevens, S. 2009. The rate of granule ripple movement on Earth and Mars, *Icarus,* 203, 71-76.

Zing, A.W. 1953. Wind tunnel studies of the movement of sedimentary material, *Procedings of the 5th Hydraulics Conference Bulletin*, 34, Institute of Hydrolics, Iowa City, 111-135.